SUBCYCLE DYNAMICS OF LASER-INDUCED IONIZATION AND TAILORED LASER FILAMENTS

A Dissertation

by

PETR ZHOKHOV

Submitted to the Office of Graduate and Professional Studies of
Texas A&M University
in partial fulfillment of the requirements for the degree of

DOCTOR OF PHILOSOPHY

Chair of Committee,	Aleksei Zheltikov
Committee Members,	Olga Kocharovskaya
	Alexei Sokolov
	Robert Nevels
Head of Department,	George Welch

December 2015

Major Subject: Physics

ABSTRACT

Powerful laser pulses with duration of few optical cycles and less open up new venues of nonlinear optics and yield novel applications for quantum optics, electronics and solid-state physics. In the present Ph.D. research we study, by means of supercomputer simulations, new approaches to powerful ultrashort pulse self-transformation in laser-induced filaments and filament-like regimes.

We have found new regimes in which unprecedentedly short powerful light pulses in optical domain can be generated in helium via shock wave formation at the optimum pulse compression point. We have found general scaling laws that extend nonlinear pulse self-transformation regimes to arbitrarily high powers.

We also study photoionization dynamics in solids at ultrashort timescales and develop a simple closed-form quantum-mechanical model of ultrafast photoionization and optical properties of photoionized solids, applicable for pulses of arbitrary shape and duration, in a wide range of field intensities, and in a wide range frequencies of field and of nonlinear response. Our model provides single self-consistent framework for nonlinear optics of absorbing semiconductors and transparent dielectrics in high-intensity fields. Using our ultrafast photoionization framework we refine criteria of ultrafast light-induced damage in the transparent material. Our simulations of ultrashort pulse propagation through photoionized solid using finite-difference time-domain code predict complex charge-field dynamics in the bulk of the solid, not described by semiclassical model of optical properties of solid-state plasma. We found non-monotonous dependence of solid-state plasma density in the wake of the pulse on depth inside the solid due to high-harmonic generation, phase matching and absorption.

Physical effects captured by our model show potential of ultrafast photoionization for future solid-state optoelectronics and information processing as it allows precise control of charge dynamics inside solids at time scales 6 orders of magnitude faster than currently available semiconductor electronics.

ACKNOWLEDGMENTS

I would like to acknowledge continuous support by my advisor, Dr. Aleksei Zheltikov. Dr. Zheltikov has enabled me with unique selection of problems to work on, discussions of highest quality and scientific nudging and babysitting in the best sense of the word without which the present thesis would hardly be written. Additionally, I should acknowledge the rare freedom of location that Dr. Zheltikov provided me, due to which I was able to spend quite some time in Russia with my family. My research was funded partially from start-up funds of Dr. Zheltikov, partially from Welch Foundation, grant A-1801, and partially from Russian Quantum Center. Several trips to the conferences have been payed by Dr. Zheltikov's funds, Dr. Marlan Scully's funds and by student travel grant from Department of Physics and Astronomy of Texas A&M University; I am very grateful for their generous support. My research has benefited enormously from discussions with my colleagues, Ilya Fedotov, Alexander Voronin, Evgeniy Serebryannikov, Sean Blakley and Hector Perez.

TABLE OF CONTENTS

Page

Page

LIST OF FIGURES

FIGURE Page

1. INTRODUCTION

Since their invention in 1953, lasers have rapidly evolved from exotic quantum-mechanical experiments into workhorses of many industrial and scientific applications. Among plethora of wonderful properties of lasers, making them useful in science and technology, lasers can produce the shortest artificial events ever made - on the order of femtoseconds (1 femtosecond, fs = 10^{-15} seconds), while recent systems push this limit even further, into the attosecond realm (1 attosecond, as = 10^{-18} s). Commercial availability of femtosecond bursts of light made it possible to directly observe and control very rapid processes, such as, for example, vibrations and rotations of molecules, creation and destruction of chemical bonds [5, 6]. Attosecond technologies provide probes for even faster processes, such as motion and rearrangement of electrons in atoms and molecules [7, 8, 9, 10]. On the other hand, these ultrashort bursts of light allow us to experimentally study dynamics of processes previously thought of as instantaneous, such as, for example, quantum-mechanical tunneling through the barrier.

Another very active and fruitful area of laser evolution is the increase of the peak pulse power that allowed study light-matter interaction at the extreme conditions where, for example, electric field of light pulse can be much stronger than natural electric field binding electrons to atomic nuclei. Modern high-power laser systems achieve petawatt (1 PW = 10^{12} watt) levels of instantaneous power that make possible efficient laser particle acceleration, X-ray generation. Next generation of ultrahigh power lasers (such as Extreme Light Infrastructure, ELI) is planned to reach so-called Schwinger limit [11] of light intensities, at which electron-hole pairs can be created in vacuum, thus paving the studies of nonlinear quantum electrody-

namics of vacuum [12]. Simultaneosly, some effects of nonlinear QED can be probed at much smaller intensities level in semiconductors; for example, photoionization [13, 14], or creation of electron-hole pair by intense radiation, is a direct analog of electron-positron pair creation in nonlinear QED.

The technique of choice in generation of ultrashort high-power laser pulses is chirped-pulse amplification (CPA), pioneered by Donna Strickland and Gerard Mourou in 1985 [15], whereby ultrashort pulses are stretched with a dispersive line (stretcher), amplified to high energy and then compressed down to original duration with another dispersive line (pulse compressor). The point of stretching is to reduce peak intensity of the amplified pulse below the threshold of onset of nonlinear effects and light-induced damage in the amplifier – the idea borrowed from high-power radar technology. It has been discovered that resulting compressed pulses are powerful enough to cause nonlinear-optical effects virtually in any media, including atmospheric air; and one of the first effects to set in is self-focusing [16, 17]. This, as a matter of fact, accidental discovery (it was found that initially collimated beam after some distance of propagation leaves burn marks on the mirrors) has opened up a whole field of nonlinear optics of filaments [18, 19]. Femtosecond filamentation is a very robust nonlinear-optical phenomenon, ocurring in gases, liquids and solids and conveying high-intensity radiation over distances much larger than diffraction length of linearly propagating light. These properties make femtosecond filaments unique tools for nonlinear optics and high-power laser physics and enable such applications as remote (up to tens of kilometers) atmosphere sensing [20, 21, 22], remote laser-induced breakdown spectroscopy, remote sub-diffraction imaging [23], laser pulse self-compression (down to sub-fs duration) [24, 25, 26, 27, 2], high harmonics generation and others (see excellent reviews [18, 19]).

While femtosecond filaments themselves have become a well-established technol-

ogy, some fundamental aspects of physics behind filaments are still unexplored. For example, at high levels of input power filaments tend to experience so-called modulational instability [28] and break down onto multiple individual filaments, interacting with each other [29, 30, 31, 32, 33, 18, 19]. Various regimes of interaction of individual filaments are of interest from the point of chaotic dynamics [34]. When filaments are used for pulse self-compression, minimum pulse duration and maximum field intensity, attainable during pulse self-compression in the filament, or, more broadly speaking, the physical mechanisms responsible for limiting pulse duration and maximum intensity, are of significant interest.

On the other hand, the nonlinearity of bound and free electrons that creates the filament is not very well studied at the sub-femtosecond timescales, relevant for description of transient waveforms during pulse self-compression in the filament. Often the existing models of non-resonant Kerr nonlinearity [17] and photoionization [13, 35, 36, 37] are taken, strictly speaking, beyond their domain of validity in theoretical description of femtosecond filaments. This makes filaments a great probe for such sub-femtosecond dynamics and at the same time calls for theoretical description of underlying nonlinearities at the relevant timescales [38, 39, 40].

The structure of the present thesis reflects evolution of the research focus of our group in Texas A&M University under supervision of Prof. Aleksei Zheltikov. First part (sections 2–6) is devoted to supercomputer numerical simulations of various regimes of filamentation in solids and gases, and analytical studies of filament properties. Second part (sections 8–12) is devoted to theoretical studies of photoionization in solids at sub-cycle time scales. We develop FCRPI - field-cycle-resolved photoionization theory (sections 8–10) and apply it to problems of optical breakdown of dielectrics by ultrashort pulses and nonlinear reflection of ultrashort pulses by interface with ionizing dielectric at sub-cycle timescales (sections 11–12).

2. NUMERICAL MODEL

To simulate interaction of multiple filaments in liquids or solids, we use the following three-dimensional time-dependent equation [41, 18, 19, 42] for complex scalar field amplitude $A = A(t, x, y, z)$ evolution:

$$\frac{\partial A_F}{\partial z} = i\left(\sqrt{k(\omega)^2 - k_x^2 - k_y^2} - \frac{\omega}{V_{gr}}\right) A_F + \mathcal{F}_{x\to k_x, y\to k_y}\left\{R_{nl}[A] + R_i[A]\right\} \tag{2.1}$$

where $A_F \equiv \mathcal{F}_{x\to k_x, y\to k_y, t\to\omega}\{A\}$ is the Fourier transform of the field amplitude, x and y are the transverse coordinates, k_x and k_y are the x and y components of the wave vector, z is the propagation coordinate, ω is the radiation frequency, $t = t_{lab} - \frac{z}{V_{gr}}$ is the retarded time, t_{lab} is the time in the laboratory frame, V_{gr} is the group velocity, $k(\omega) = \frac{\omega}{c} n(\omega)$, c is the speed of light in vacuum, $n(\omega)$ is the frequency-dependent linear refractive index. Equation (2.1) is derived from Maxwell equations in the approximation of unidirectional field evolution, that is, that most of the energy of the field propagates approximately in the same direction, or, alternatively, that the back-scattered wave is weak [43, 44]. The term $R_{nl}[A]$ includes instantaneous (Kerr) and inertial (Raman) parts of the nonlinear-optical response:

$$R_{nl}[A] = i\frac{\omega}{c}\mathcal{F}_{t\to\omega}\left\{n_2\int_0^\infty K(\tau)|A(t-\tau,x,y,z)|^2 + \chi_{TH}A^3 + n_4|A|^4 A d\tau A\right\}, \tag{2.2}$$

where n_2 and n_4 is are second- and fourth order nonlinear refractive indices,

$$\begin{aligned} n_2 &= \frac{\omega}{ck(\omega)}\sqrt{\frac{\mu_0}{\epsilon_0}}\chi^{(3)}(\omega;\omega,-\omega,\omega), \\ n_4 &= \frac{\omega}{ck(\omega)}\frac{\mu_0}{\epsilon_0}\chi^{(5)}(\omega;\omega,\omega,\omega,-\omega,-\omega), \\ \chi_{TH} &= \frac{\omega}{ck(3\omega)}\sqrt{\frac{\mu_0}{\epsilon_0}}\chi^{(3)}(3\omega;\omega,\omega,\omega), \end{aligned} \tag{2.3}$$

$\chi^{(3)}$ and $\chi_{(5)}$ are third- and fifth order nonlinear susceptibility tensors [45, 46, 47] $K(\tau)$ is the Raman response function,

$$K(\tau) = (1-f_R)\delta(\tau) + f_R\frac{1+\Omega_R^2\tau_R^2}{\Omega_R^2\tau_R}e^{-\tau/\tau_R}\sin\Omega_R\tau \tag{2.4}$$

Here f_R is the fraction of the delayed response in the total nonlinear response, Ω_R is the Raman frequency, τ_R is the decay time, and $\delta(\tau)$ is the Dirac delta function. The first term in Eq. (2.4) mimics the instantaneous Kerr response, and the second term models the inertial Raman nonlinearity [48].

Ionization effects are included through the $R_i[A]$ function [18, 19]:

$$R_i[A] = \frac{\sigma(\omega)}{2}\left(1+i\omega\tau_c\right)\mathcal{F}_{t\to\omega}\left\{\rho A\right\} - \mathcal{F}_{t\to\omega}\frac{W\left(|A|^2\right)}{|A|^2}\left(U_i+U_p\right), \tag{2.5}$$

where $\sigma(\omega) = \frac{\mu_0 e^2}{mk(\omega)(1+\omega^2\tau_c^2)}$ is the inverse bremsstrahlung cross section, τ_c is the electron momentum transfer time, μ_0 is vacuum permeability, m is the electron mass. The first term on the right-hand side of Eq. (2.5) describes free-electron refraction and absorption, while the second term accounts for photoionization losses, where $W(|A|^2)$ is the photoionization rate, U_i is the ionization potential or band gap, $U_p = \frac{e^2|A|^2}{m\omega_0^2}\sqrt{\frac{\mu_0}{\epsilon_0}}\frac{1}{n_0}$ is the ponderomotive energy of an electron oscillating in the electromagnetic wave, ϵ_0 is the vacuum permittivity, $n_0 \equiv n\left(\omega_0\right)$ is the linear refrac-

tive index at the central pulse frequency ω_0. The electron density $\rho \equiv \rho(t, x, y, z)$ is found by solving the equation:

$$\frac{\partial \rho}{\partial t} = W\left(|A|^2\right)\rho_{at} + \frac{\sigma(\omega_0)}{U_i + U_p}\rho|A|^2 - \frac{\rho}{\tau_r}, \tag{2.6}$$

First term in (2.6) describes photoionization, where $W(|A|^2)$ is photoionization rate per atom, molecule or unit crystal cell, ρ_{at} is density of atoms, molecules or inverse volume of a unit crystal cell. Second term in (2.6) describes avalanche photoionization, and the last term – finite lifetime of free carriers τ_r.

When considering a single filament, we can make use of cylindrical symmetry of the beam and instead of transverse coordinates x and y introduce transverse radial coordinate. The Fourier transform over transverse coordinates then becomes Hankel transform (or Fourier-Bessel transform or zeroth order)

$$\mathcal{F}_{r\to k_r}\{f(r)\} \equiv \int_0^\infty 2\pi J_0(k_r r) f(r) dr \tag{2.7}$$

Additionally, we use $k_x^2 + k_y^2 = k_r^2$, and also use the fact that for single filament $k_r \ll k(\omega)$ and rewrite (2.1) as

$$\frac{\partial A_F}{\partial z} = i\left(D(\omega) - \frac{k_r^2}{2k(\omega)}\right)A_F + R_{nl}[A] + R_i[A] \tag{2.8}$$

where $D(\omega) = k(\omega) - \omega/V_{gr}$ is the dispersion operator.

The nonlinear-optical responses of noble gases in high-intensity fields, on one hand, do not have delayed nonlinearity (the delayed nonlinearity comes from rotations or vibrations of molecules. Stricly speaking, response of bound electrons is also somewhat inertial [49], however, at the timescales relevant to most regimes of femtosecond filamentation such inertia can be neglected). On the other hand, there

are additional terms related to higher-order electronic nonlinearities and multiple ionization of atoms

$$R_{nl}[A] = i\frac{\omega}{c}\mathcal{F}_{t\to\omega}\left[n_2\left(|A|^2A + \frac{1}{3}A^3\right) + n_4\left(|A|^4A + \frac{1}{2}|A|^2A^3\right)\right], \tag{2.9}$$

where n_2 and n_4 are the Kerr nonlinear refractive indices. The $|A|^2A$ and $|A|^4A$ terms describe intensity dependent refraction, while the $\frac{1}{3}A^3$ and $\frac{1}{2}|A|^2A^3$ terms account for third-harmonic generation through the third- and fifth-order nonlinear susceptibilities.

R_i term on the right-hand side of Eqs. (2.1) and (2.8) that accounts for ionization response is modified as follows

$$R_i[A] = -\frac{\sigma(\omega)}{2}(1 + i\omega\tau_c)\mathcal{F}_{t\to\omega}\left[\rho(t)A\right] - \mathcal{F}_{t\to\omega}\left[\sum_{Z=0}^{N}\frac{U_Z + U_p}{|A|^2}W_Z\rho_Z A\right], \tag{2.10}$$

where U_Z and W_Z are the ionization potential and photoionization rate for an ion with a charge Z, U_p is the electron ponderomotive energy. The time-dependent free electron density $\rho(t)$ is found by integrating the following set of equations [50]:

$$\frac{\partial\rho_0}{\partial t} = -W_0\rho_0, \tag{2.11}$$

$$\frac{\partial\rho_Z}{\partial t} = W_{Z-1}\rho_{Z-1} - W_Z\rho_Z \quad \text{for } Z = 1, \ldots, N, \tag{2.12}$$

$$\rho = \sum_{Z=1}^{N} Z\rho_Z, \tag{2.13}$$

where ρ_Z is the density of ions with a charge Z, subject to the initial conditions

$$\rho_Z\left(t=0\right)=0 \quad \text{for } Z=1,\ldots,N, \tag{2.14}$$

$$\rho_0\left(t=0\right)=\rho_{at}, \tag{2.15}$$

ρ_{at} is the density of neutral atoms.

For the purposes of analysis of various physical mechanisms responsible for certain aspects of filaments it can be useful to introduce central frequency ω_0 and rewrite (2.8) in t, r, z coordinates as [18, 19, 42]

$$\frac{\partial A}{\partial z}=i\left(\hat{D}+T^{-1}\frac{\nabla_r^2}{2k_0}\right)A+\hat{R}_{nl}[A]+\hat{R}_i[A] \tag{2.16}$$

where

$$T=1+\frac{i}{\omega_0}\frac{\partial}{\partial t} \tag{2.17}$$

is self-steepening operator , $k(\omega)\approx k(\omega_0)\left(1+\frac{\omega-\omega_0}{\omega_0}\right)$ in the denominator of the diffraction term $T^{-1}\frac{\nabla_r^2}{2k_0}$ in (2.16); $\hat{D}A=\mathcal{F}_{\omega\to t}DA_F$ and $\hat{R}_i[A]=\mathcal{F}_{\omega\to t}R_i[A]$ are Fourier-transforms of dispersion operator and ionization response into time domain, respectively. Nonlinear response operator can be written fully in time-domain using operator T as

$$\hat{R}_{nl}[A]=i\frac{\omega_0}{c}n_2T\left\{\int_0^\infty K(\tau)|A(t-\tau,r,z)|^2d\tau A+n_4|A|^4A\right\}, \tag{2.18}$$

In expression (2.18) we have included higher-order nonlinearity through $n_4|A|^4A$ term, which will be useful in the analysis of optical shock-wave formation (section 5). In the same way, third harmonic generation terms from (2.9) can be included.

3. SUPERCOMPUTER SIMULATIONS

Equations (2.1)–(2.11) were solved using split-step method [51, 52, 48]. Specifically, in the equation (2.1) linear term

$$i\left(\sqrt{k(\omega)^2-k_x^2-k_y^2}-\frac{\omega}{V_{gr}}\right)A_F \tag{3.1}$$

is local in the k_x, k_y space (the space of transverse wavenumbers), that is, change of amplitude A_F given by the term (3.1) at point $k_{x,0}, k_{y,0}$ depends only on values of A_F at $k_{x,0}, k_{y,0}$ (and various values of frequency ω). Such locality means that change in A_F due to linear term (3.1) can be calculated in various grid points in k_x, k_y in parallel. In the cylindrically symmetric case (Eq. (2.8)) linear term

$$i\left(D(\omega)-\frac{k_r^2}{2k(\omega)}\right)A_F \tag{3.2}$$

is local in variable k_r. At the same time, nonlinear term

$$\mathcal{F}_{x\to k_x, y\to k_y}\left\{R_{nl}[A]+R_i[A]\right\} \tag{3.3}$$

is local in space of transverse coordinates x, y. Locality allows parallel calculation of linear term in all points in k_x, k_y-space (or k_r-space) simulataneously, and parallel calculation of nonlinear term in all points x, y-space simultaneously. The computation step is then as follows:

1. Calculate $A_F^{(l)}(z)=e^{R^{(l)}\Delta z}A_F(z)$, where $R_l=i\left(\sqrt{k(\omega)^2-k_x^2-k_y^2}-\frac{\omega}{V_{gr}}\right)$
2. Calculate Fourier transform $A^{(l)}(t,x,y,z)=\mathcal{F}_{\omega\to t,k_x\to x,k_y\to y}A_F^{(l)}(\omega,k_x,k_y,z)$

3. Calculate $\Delta A(t,x,y,z)$ - change of $A(t,x,y,z)$ during the step Δz due to nonlinear term (3.3) using Runge-Kutta method of the fourth order and $A^{(l)}(t,x,y,z)$ as input

4. Calculate $\max|\Delta A(t,x,y,z)|$. If $(\max|\Delta A(t,x,y,z)| > Tol \max|A(t,x,y,z)|$, where Tol is numerical tolerance parameter (that physically has the meaning of maximum nonlinear phase shift during one step and usually selected between 0.01 and 0.05), set $\Delta z \leftarrow \Delta z/2$, discard $\Delta A(t,x,y,z)$ and repeat step 3.

5. Set $A_F \leftarrow A_F^{(l)} + \mathcal{F}_{t\to\omega,x\to k_x,y\to k_y}\Delta A(t,x,y,z)$

6. Set $\Delta z \leftarrow 0.5 Tol \max|A(t,x,y,z)|/\max|\Delta A(t,x,y,z)|$

Discretization steps in time t and transverse coordinates x and y (or radial coordinate r) were chosen fixed in such a way as to provide a reliable convergence of the numerical procedure.

Simulations were performed in parallel codes using Message Passing Interface (MPI) technology at the Lomonosov supercomputer of Moscow State University in Russia, and using Graphics Proccessing Units (GPU) through Compute Unified Device Architecture (CUDA) technology on the workstations in Texas A&M University and in Moscow State University.

4. RELATIVISTIC-INTENSITY FILAMENTS*

In this section, we show that filamentation-assisted compression of subpetawatt laser pulses is possible in low-pressure gases, where the gas pressure is chosen in such a way as to avoid multiple filamentation and where the depletion of outer-shell ionization is used to steer the balance between Kerr-nonlinearity-induced self-focusing and plasma defocusing toward the optimum for self-compression of subpetawatt laser pulses [1].

Simulations were performed for low-pressure argon. Dispersion was included in the model through the appropriate Sellmeier equation for argon [53]. The nonlinear refractive indices are calculated as $n_{2,4} = \overline{n}_{2,4}\frac{p}{p_0}$, where p is the gas pressure and p_0 is the atmospheric pressure. The values of the nonlinear refractive index $\overline{n}_2$ for argon available from the literature vary within at least the range from $0.8\text{x}10^{-19}$ to $1.5\text{x}10^{-19}$ cm^2W^{-1} [54, 55, 56, 57]. For our simulations, we take $\overline{n}_2 = 10^{-19}$ cm^2 W^{-1}. Since all the Kerr-type processes in our system are controlled by the product of $\overline{n}_2$ and the gas pressure p, the uncertainty in $\overline{n}_2$ simply implies an additional adjustment of the gas pressure p. The critical power for self-focusing at $p = 1$ bar for radiation with the wavelength $\lambda_0 = 800$nm is then equal to $P_{cr} = \frac{3.77\lambda_0^2}{8\pi n_2 n_0} \approx 9.6$ GW. The electron momentum transfer time was calculated as $\tau_c = \overline{\tau}_c\frac{p_0}{p}$ with $\overline{\tau}_c = 190$ fs for argon [18, 19]. In electron density calculations, it was sufficient to limit the sum in Eqs. (2.10) and (2.11) with $N = 11$, as the number of Ar^{11+} ions was negligibly small. Throughout this paper, we discuss simulations performed for a Gaussian pulse with an FWHM pulse width $\tau_0 = 30$ fs and the central wavelength $\lambda_0 = 800$ nm.

*Section reprinted with permission from "Filamentation-assisted self-compression of subpetawatt laser pulses to relativistic-intensity subcycle field waveforms" by P. A. Zhokhov, V. Ya. Panchenko, and A. M. Zheltikov [1]

Light pulses with such parameters and energies in the range of a few joules can be routinely generated by the available 100–200-TW laser systems [58, 59]. Simulations done with other input pulse shapes, including flat-top, super-Gaussian pulses, show that, because of the highly nonlinear, strongly coupled temporal and spatial field waveform dynamics, which involves pulse and beam sectioning, it is nontrivial to identify simple pulse-shaping strategies that would efficiently optimize filamentation-assisted pulse compression or enhance its energy throughput in the considered range of field intensities. The input beam diameter and the focusing length were varied in our (3+1)-dimensional simulations in order to achieve the highest efficiency of pulse compression simultaneously avoiding the multiple filamentation of a beam, as discussed below in this paper. In what follows, we present the results of simulations performed for a Gaussian laser beam with an initial FWHM diameter of 2 cm and a linear focal length of 5 m. This beam focusing geometry was found to provide the most promising regime of pulse compression.

To avoid multiple filamentation of the high-power laser beam, the gas pressure in our analysis is chosen in such a way as to keep the critical power for self-focusing P_{cr} approximately at the level of the the peak power P of the laser pulse. In particular, for a 30-fs pulse with $E_0 = 6$ J, the peak power becomes equal to P_{cr} at an argon pressure of $5.11\text{x}10^{-5}$ bar.

As a first step of our analysis, we verify that the high-power laser pulse with a given initial energy forms a single filament as it propagates through the low-pressure gas, with its beam profile remaining stable with respect to the buildup of a small-scale multifilamentary beam structure. Figure 4.1(a) presents the results of (3+1)-dimensional simulations for a 30-fs laser pulse with an energy of 6 J, propagating in argon at $p = 5.11\text{x}10^{-5}$ bar, with $P = P_{cr}$. The beam at the linear focus point $z = 0$ displays perfect cylindrical symmetry with no signatures of multiple filamentation.

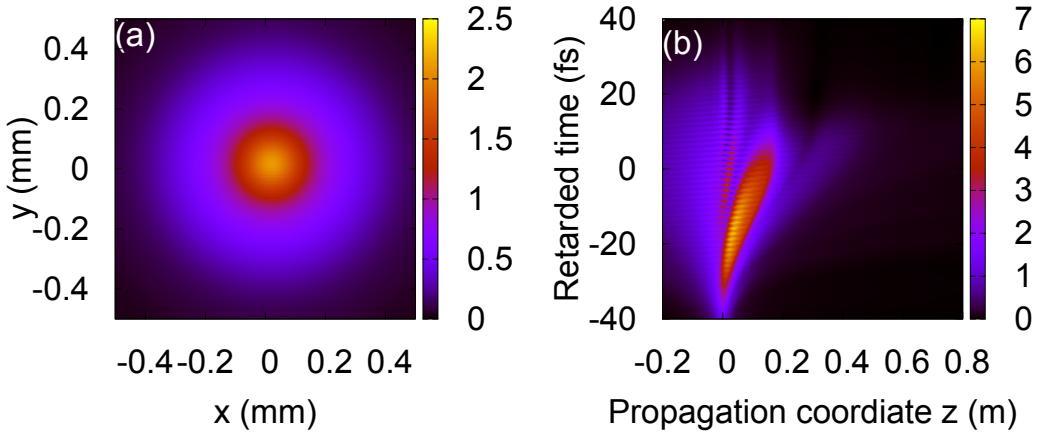

Figure 4.1 (a) The fluence $F = \int |A|^2 dt$ (kJ/cm^2) as a function of transverse coordinates x and y of a high-power beam with $E_0 = 6$ J, $\tau_0 = 30$ fs, and $\lambda_0 = 800$ nm at $z = 0.4$ m in argon at $p = 5.11\text{x}10^{-5}$ bar simulated by solving the (3+1)-dimensional GNSE. (b) The on-axis field intensity (PW/cm^2) as a function of the propagation distance and retarded time for $E_0 = 1$ J, $\tau_0 = 30$ fs, and $P = P_{cr}$. From P. A. Zhokhov *et al*, 2012 [1]

However, avoiding multiple filamentation by keeping $P_{cr} \approx P$ at lower gas pressures is necessary, but not sufficient to effectively scale filamentation-assisted pulse compression to extreme light powers. Since the ionization rate is typically a much steeper function of the laser intensity than the Kerr nonlinearity, efficient pulse compression of extreme-power laser pulses at low gas pressures is prevented [Figs. 4.1(b), 4.2(a)] by a fast increase in the electron density along the filament [dashed curve in Fig. 4.2(a)], which tends to defocus the laser beam following the initial stage of beam self-focusing [Fig. 4.1(b)]. To steer the balance between ionization-induced defocusing and Kerr-nonlinearity-related self-focusing toward more efficient pulse compression in longer filaments, we use specific properties of argon, which features a large gap ($\Delta U \approx 280$ eV) between the ionization potentials of M- and L-shell

electrons. When the laser field intensity is high enough to deplete the M-shell, the large gap ΔU tends to stabilize the electron density along the filament. This effect is illustrated by Fig. 4.2(a), showing that 1- and 6-J laser pulses generate filaments where the maximum field intensities differ by two orders of magnitude, while the average ionization degrees $\langle Z \rangle = \rho/\rho_{at}$ differ only by factor of two. This result is in striking contrast with filamentation at the atmospheric pressure, when the electron density rapidly grows with the laser intensity [18, 19]. For $E_0 = 6$ J, the average ionization degree $\langle Z \rangle$ is effectively clamped at $\langle Z \rangle = 8$ (which corresponds to a complete depletion of the M-shell) and remains unchanged over more than 1 m.

Due to this electron density clamping effect, the Kerr-nonlinearity-related phenomena can be decoupled within a limited time interval and limited propagation path from ionization-induced defocusing, as the laser intensity can increase [Fig. 4.2(a)] without a noticeable growth in the electron density [solid curve, the range of intensities from 0.2 to 0.8 EW/cm^2 in Fig. 4.2(a)]. The spatial self-action of a high-power laser beam under these conditions is dominated by the Kerr nonlinearity, enabling efficient pulse compression through pulse self-steepening and space-time focusing [18, 19].

This regime of pulse self-compression is illustrated in Figs. 4.3(a) and 4.3(b), which present the spatiotemporal dynamics and dynamics of spectral broadening of a laser pulse with $\tau_0 = 30$ fs and energy 6 J in argon at $p = 5.11\text{x}10^{-5}$ bar with $\overline{n}_4 = 0$. Behind the linear focus [$z = 0$, shown by white contour lines in Fig. 4.2(b)], the beam continues to focus due to the Kerr nonlinearity [Fig. 4.2(b)], which dominates within this section of propataion path over ionization-induced defocusing, suppressed due to the depletion of ionization from the outer shell of argon. This beam self-focusing dynamics is accompanied by pulse reshaping and compression in the time domain, as well as by efficient supercontinuum generation in the spectral domain. At $z =$

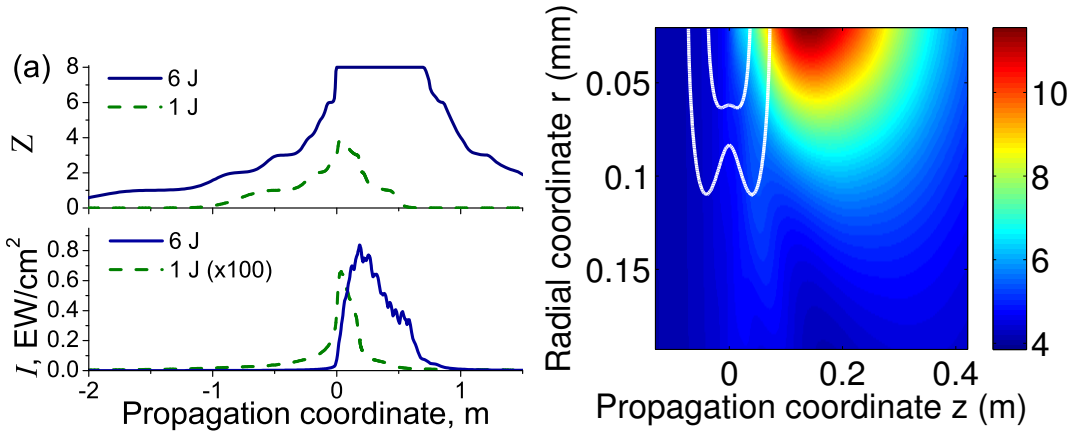

Figure 4.2 (a) The ionization degree (top) and the maximum on-axis field intensity (bottom) versus the propagation coordinate z for $\tau_0 = 30$ fs, $P = P_{cr}$ and $E_0 = 6$ J (dashed lines) and 1 J (solid lines). (b) The fluence (kJ/cm^2) as a function of the propagation distance z and radial coordinate r for $E_0 = 6$ J, $\tau_0 = 30$ fs, $P = P_{cr}$. The levels of 0.1 and 0.3 of the maximum field intensity for a linearly focused beam are shown by white contour lines. From P. A. Zhokhov *et al*, 2012 [1]

0.5 m, the spectrum of this supercontinuum stretches into the UV region, where it starts to interfere with the third harmonic (the spectral component centered at 1.2 PHz).

Maximum pulse compression is achieved at a certain distance inside a filament ($z = 0.6$ m for the chosen set of parameters, see Figs. 4.4 and 4.5). This distance of maximum compression depends on the gas pressure. As the pressure of argon is increased from 5.11x10^{-5} bar (the pressure that provides compression to the shortest pulse width) to 6x10^{-5} bar, maximum compression to a pulse width of about 3 fs is achieved at $z = 0.5$ m.

In Fig. 4.4(a), we show the FWHM pulse width, the rms pulse width

$$\tau_{rms} = \sqrt{\frac{\int_0^{r_0} rdr \int dt|A|^2t^2}{\int_0^{r_0} rdr \int dt|A|^2} - \left(\frac{\int_0^{r_0} rdr \int dt|A|^2t}{\int_0^{r_0} rdr \int dt|A|^2}\right)^2}, \tag{4.1}$$

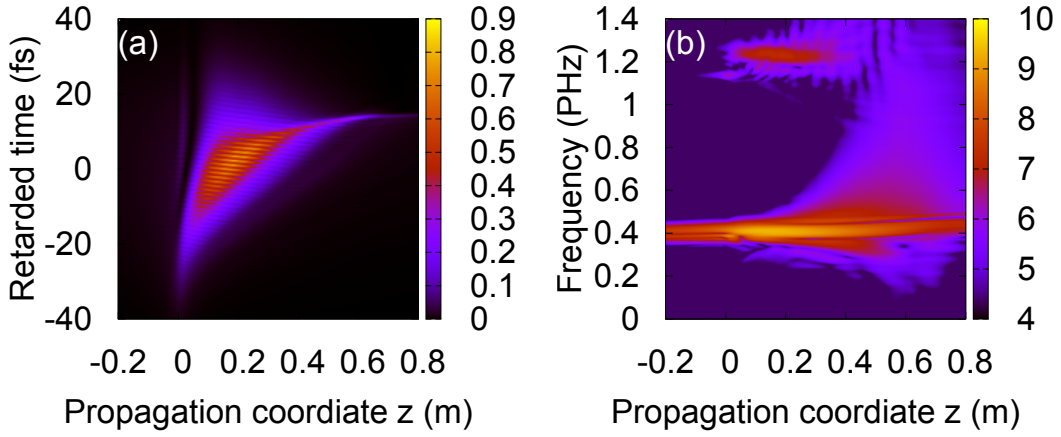

Figure 4.3 (a) The on-axis field intensity (EW/cm^2) as a function of the propagation distance and retarded time and (b) the on-axis spectral intensity in arbitrary units on the log scale as a function of the propagation distance and frequency for $E_0 = 6$ J, $\tau_0 = 30$ fs, and $P = P_{cr}$. From P. A. Zhokhov *et al*, 2012 [1]

where r_0 is the aperture of, e.g., a pinhole used to select the central part of the beam at $z = 0.6$ m. With $r_0 = 0.14$ mm, pulses with an FWHM pulse width of 1.3 fs and a total energy of about 0.3 J can be generated [Fig. 4.4(b)]. The contrast of this pulse is 20 with respect to a prepulse at $t = -\tau_0/2 = -15$ fs and 200 with respect to a postpulse at $t = +\tau_0/2 = 15$ fs. The steep trailing edge of this pulse is indicative of the key role of self-steepening and space-time focusing effects in this regime of pulse compression. The FWHM width of the temporal envelope of $|A|^2$ on the beam axis at $z = 0.6$ m is 0.86 fs, which corresponds to 0.3 field cycles [Fig. 4.5(a)]. Generation of such an extremely short pulse is facilitated by the interference of the spectrally broadened fundamental field and its third harmonic, which gives rise to fringes, visible in Fig. 4.3(a). This process enhances the central peak of the field that undergoes the most efficient self-focusing [Fig. 4.3(a)], giving rise to

a solitary peak in the radial profile of the field intensity, which is manifested as a plateau in the dependence of the pulse width on the pinhole diameter in Fig. 4.4(a). The light intensity achieved in transient field waveforms on the beam axis as a part of this pulse self-compression dynamics is as high as 0.8 EW/cm^2 [$z = 0.2$ m in Figs. 4.2(a), 4.3(a)], falling in the range of relativistic field intensities.

Generation of relativistic-intensity subcycle field waveforms is quite sensitive to variations in the parameters of the input laser pulse, as well as variations in the gas pressure. Stretching of the input pulse by 3% of its width or a decrease in the input pulse energy by 200 mJ would increase the pulse width at the point of maximum compression inside the filament up to approximately 3.5 fs. As the gas pressure is increased by 20%, the shortest pulse width achieved in the filament is increased to 3 fs.

Even higher field intensities can be generated as a result of filamentation-assisted pulse self-compression dynamics for laser beams with higher input energies. In particular, a laser pulse with $E_0 = 7$ J and $\tau_0 = 30$ fs inducing a filament in argon at $p =$ 3.1x10^{-5} bar generates subcycle field transients with the field intensity as high as 2 EW/cm^2. The filament length tends to increase with the growth in the input energy in this regime in agreement with the tendency illustrated in Fig. 4.2(a). Technically, the computer code remains perfectly stable and fully functional in this range of extreme light intensities, while the small-scale features in the spatiotemporal structure of the field can be analyzed using finer adaptive computation steps in space and time. However, since the relativistic physics of light – matter interaction at these cites of extremely high light intensity in filaments is not included in our model and falls beyond the scope of this study, we restrict our analysis here to the regimes where the regions of relativistic light intensity are localized within very small areas, exerting no influence on the overall spatiotemporal dynamics of the laser beam.

We emphasize here that relativistic-intensity subcycle field transients are generated as a part of the considered pulse-compression scenario at a certain propagation distance inside the filament. Filtering this extreme-intensity subcycle field waveform for experiments in the far field is a challenging issue, which may limit the utility of the proposed pulse compression strategy. One possible solution to this problem is to perform relativistic laser–particle interaction experiments (e.g., experiments on particle acceleration) right inside the filament. Our simulations show that, by increasing the energy of the input laser pulse up to 7 J, it is possible to generate relativistic-intensity subcycle field transients on a centimeter spatial scale. An alternative solution would be to filter such extreme-intensity subcycle pulses using appropriate pinholes for far-field experiments in the single-shot mode, which is not uncommon for extreme-intensity laser science.

The residual chirp of the pulse at the point of maximum compression [see the contour lines in Figs. 4.4(c), as well as the profiles of the temporal and spectral phases in Figs. 4.5(a) and 4.5(b)]. This suggests that a further compression of this pulse would be possible with an appropriate dispersion of a medium behind the filter or a properly designed dispersion-compensating component. The transform-limited pulse width supported by the full spectrum of the pulse at the point of maximum compression is 0.53 fs, which corresponds to 0.2 field cycles.

While argon has been shown to be ideally suited for filamentation-assisted pulse compression to subcycle pulse widths and relativistic field intensities, a similar spatiotemporal dynamics of high-power ultrashort light pulses can be implemented using other gas media. Specifically, neon and krypton, the nearest neighbors of argon in the periodic table in the family of rare gases, would be other promising candidates, enabling the expansion of the parameter space for the considered regime of pulse compression. In particular, neon, due to its higher ionization potential, would be

suitable for the compression of ultrashort pulses with even higher initial energies (up to 30 J according to our simulations), while krypton would be promising for compression of laser pulses with lower energies (in the range of 0.5 – 2 J). Obviously, the initial beam diameter and focusing geometry need to be appropriately adjusted for efficient pulse compression in other gas media.

Higher order nonlinearities, included in our model through the n_4 terms in Eqs. (2.1),(2.2) and (2.9), may play a significant role in pulse self-compression in the regime of extreme light intensities. While positive n_4 values tend to assist filamentation and pulse compression, negative n_4 may stop self-focusing before the optimal conditions for pulse self-compression are achieved [Fig. 4.4(d)]. Under these conditions, the optimal gas pressure and initial beam focusing should be redefined with the inclusion of the n_4 effects for the maximum efficiency of pulse self-compression.

In summary, we have shown that filamentation-assisted spatiotemporal dynamics of ultrashort laser pulses in the regime of extreme light powers can enable self-compression of subpetawatt laser pulses to subcycle pulse widths and relativistic field intensities. Supercomputer simulations presented here demonstrate compression of 6-J, 30-fs laser pulses to 1.3-fs sub-100-TW broadband field waveforms and reveal the generation of relativistic-intensity subfemtosecond field transients as a result of such a pulse evolution scenario, with multiple filamentation avoided due to low gas pressures and the balance between Kerr and ionization nonlinearities steered toward optimal pulse compression due to the depletion of ionization from the outer shell of atoms by a high-power laser field.

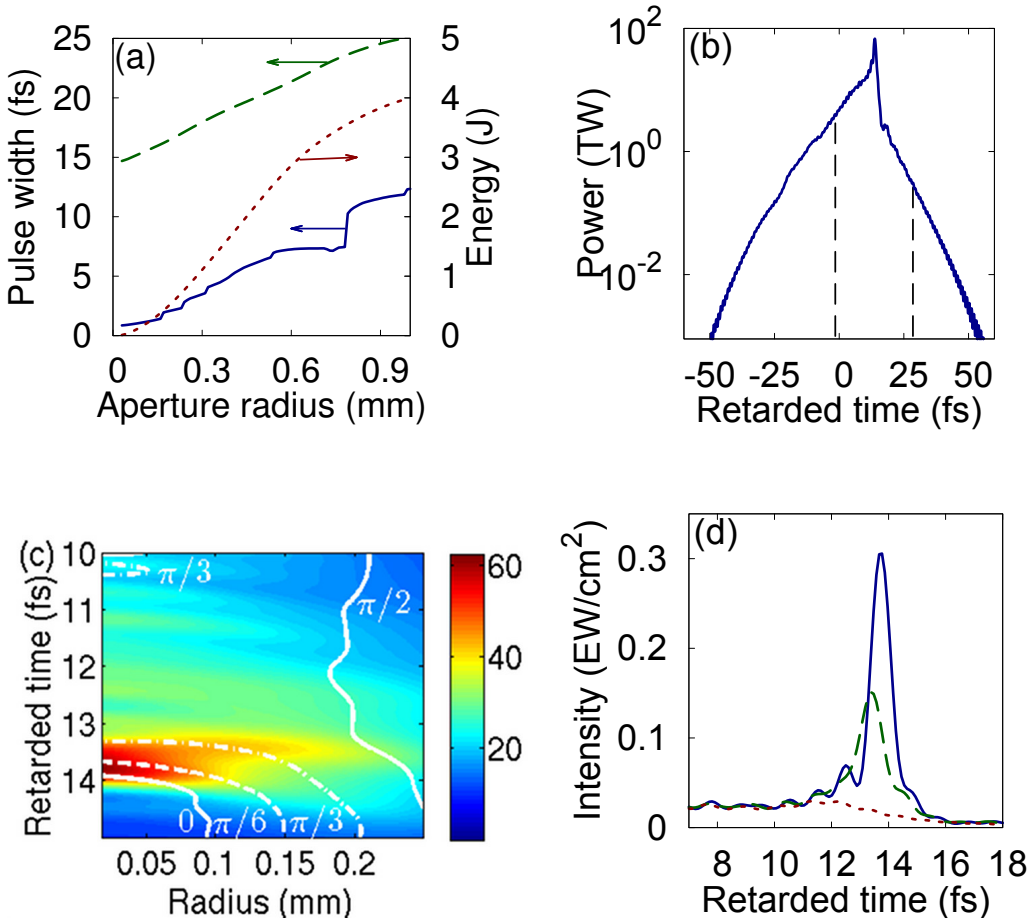

Figure 4.4 (a) The FWHM pulse width (solid blue line), the rms pulse width (dashed green line), and the total energy (red dotted line) for the compressed pulse transmitted through an aperture with a radius r_0 at z=0.6 m, (b) the power in the pulse (log scale) transmitted through an aperture with a radius of 0.14 mm at $z = 0.6$ m. The vertical dashed lines show the initial pulse width. (c) The maps of the field intensity (PW/cm^2) versus retarded time and radius at $z = 0.65$ m. White contour lines are the isolines of the temporal phase. (d) The on-axis field intensity versus the retarded time at $z = 0.6$ m for $\overline{n}_4 = 0$ (blue solid line), -1x10^{-39} TW^2/cm^4 (green dashed line), -1x10^{-38} TW^2/cm^4 (red dotted line) . In all cases $E_0 = 6$ J, $\tau_0 = 30$ fs, and $P = P_{cr}$. From P. A. Zhokhov *et al*, 2012 [1]

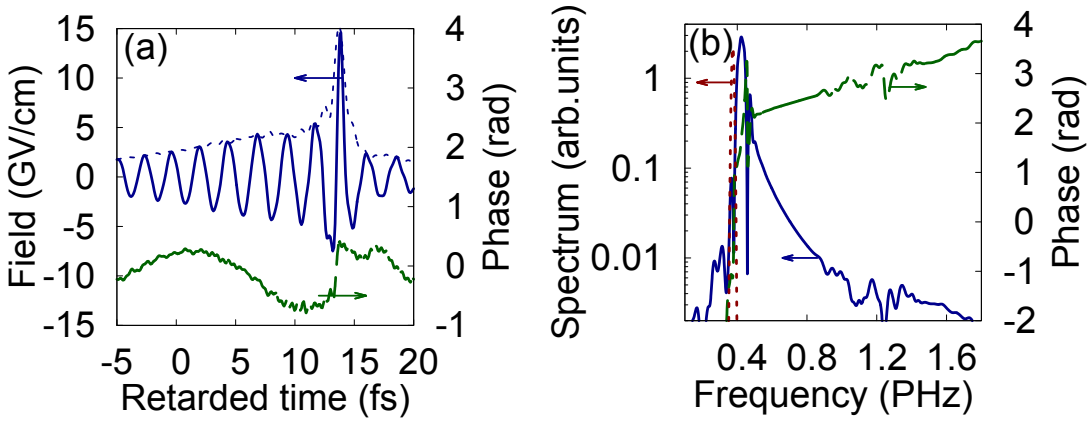

Figure 4.5 (a) The on-axis electric field (solid blue line) and its envelope (blue dotted line) versus the retarded time and (b) the spectrum of this field waveform at $z = 0.6$ m for $E_0 = 6$ J, $\tau_0 = 30$ fs, and $P = P_{cr}$. The green dashed line shows (a) the temporal and (b) the spectral phase of the field. The spectrum of the input pulse is shown in (b) by the dotted red line. From P. A. Zhokhov *et al*, 2012 [1]

5. ATTOSECOND SHOCK WAVES*

A shock wave is a generic term for an abrupt, often discontinuous, transient disturbance of physical parameters that exhibits a clearly pronounced wavelike behavior as it propagates through a medium [60, 61, 62]. Examples of shock waves are found in fluid dynamics, nonlinear acoustics, astrophysics, seismology, and detonation physics and include such diversified natural phenomena as thunder, volcanic and stellar explosions, earthquakes, and tsunamis [63]. An important class of shock waves, observed in ocean physics, acoustics, and nonlinear electrodynamics, is produced through a nonlinear wave steepening. In optics, this type of nonlinearity translates into the intensity dependence of the group velocity, leading to a self-steepening of one of the pulse edges. Following the early theoretical predictions in the 1960s [64], optical shock waves have been experimentally demonstrated [65, 66] and insightfully explained [67] in terms of the nonlinear wave-evolution equation as a part of the classical work on spectral broadening of ultrashort laser pulses in nonlinear media. In more recent studies, shock-wave effects have been shown to play an important role in supercontinuum generation in highly nonlinear fibers [68, 69], as well as in ultrafast optical waveform dynamics in laser-induced filaments [18, 19, 70, 71].

One-dimensional shock-wave effects, observed in optical fibers [48], are known to steepen the trailing edge of the pulse, but do not lead to pulse shortening. Similar to hydrodynamic shocks, which obey a set of well-defined conservation and propagation laws [72], 1D shock waves in nonlinear optics have been shown to satisfy energy and photon-number conservation [73, 74, 75] and to evolve in accordance with fundamental equations of electrodynamics [48], allowing in some approximations compact

*Section reprinted with permission from "Attosecond shock waves" by P. A. Zhokhov and A. M. Zheltikov [2]

analytical self-similar solutions.

In this section, we demonstrate that a three-dimensional dynamics of ultrashort light pulses, which involves strongly coupled spatial and temporal nonlinear effects, can give rise to isolated optical shock transients with remarkably short, subfemtosecond pulse widths, suggesting an ionization-free pulse self-compression scenario whereby multigigawatt attosecond optical waveforms can be synthesized [2].

The input peak power in our simulations was chosen slightly below the critical power of self-focusing $P_{cr} = \frac{\lambda_0^2}{2\pi n_0 n_2}$, where $\lambda_0 = \frac{2\pi c}{\omega_0}$ is the central wavelength, n_0 is the linear field-free refractive index. The initial beam sizes and the focusing geometry were varied in a broad range to achieve a specific scenario of space–time self-focusing where the self-steepening of the trailing edge of the pulse is accompanied by the diffraction of the leading edge of the pulse, allowing a shock wave to evolve toward an extremely short pulse width.

Helium was chosen as a nonlinear medium in our simulations because of its high ionization potential ($U_i \approx 24.59$ eV), providing a broad transparency range, needed to support the spectrum of subfemtosecond shock-wave transients. The nonlinear refractive indices for helium are $n_2 \approx 3\text{x}10^{-8}\frac{p}{p_0}$ cm^2/TW and $n_4 \approx -1\text{x}10^{-11}\frac{p}{p_0}$ cm^4/TW^2 [76, 77, 78, 56], where p is the gas pressure and p_0 is the atmospheric pressure. The entire dispersion profile of the gas is included in the model through the $n(\omega)$ data for helium from Ref. [79].

Laser pulses with a peak power well above P_{cr} tend to form filaments in accordance with the standard filamentation scenario as beam self-focusing due to the Kerr nonlinearity of the gas is balanced by ionization-induced defocusing. As shown by the extensive earlier work (see, e.g., Refs. [18, 19] for review), this regime of beam dynamics, accurately reproduced in our simulations, enables pulse compression to few-cycle pulse widths. A drastically different scenario of field evolution is observed

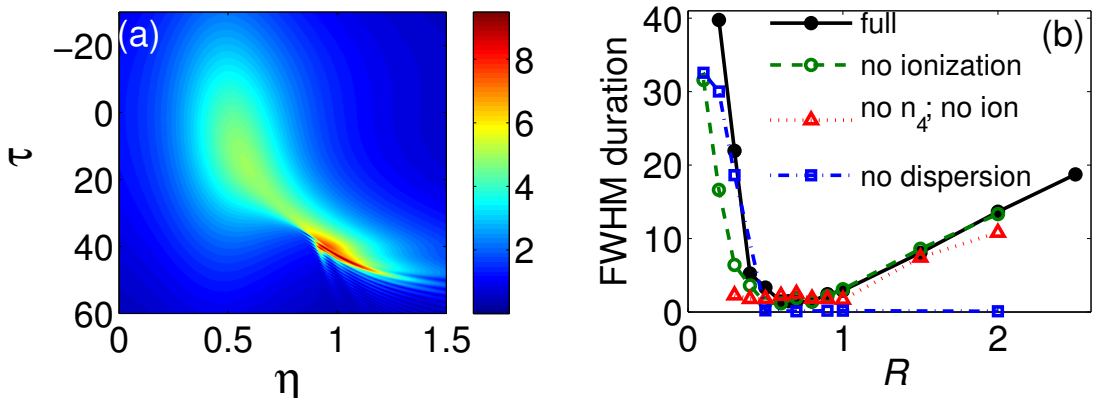

Figure 5.1 (a) Spatiotemporal map of the on-axis field amplitude $\mathcal{A}$ for $f = 0.65L_d$ and (b) the minimum dimensionless FWHM pulse width on the beam axis as a function of $R = f/L_d$ calculated with the full model (solid line, filled circles), with ionization switched off (dashed line, open circles), with ionization and high-order nonlinearity switched off (dotted line, triangles) and with dispersion switched off (dash-dotted line, rectangles) for $P = 0.8P_{cr}$, $\tau_0 = 70$. From P. A. Zhokhov and A. M. Zheltikov, 2013 [2].

for loosely focused laser beams with peak powers slightly below P_{cr}. This regime of nonlinear spatiotemporal field dynamics is illustrated in Fig. 5.1(a) for an input field with a peak power $P = 0.8P_{cr}$ taken in the form of Gaussian pulse with dimensionless pulse width $\tau_0 = 70$ and Gaussian spatial profile, focused in helium with a focal length $f = 0.65L_d$. An ultrashort shock wave is seen to build up on the trailing edge of the pulse [Fig. 5.1(a)] as a result of this spatiotemporal field evolution. The minimum pulse width of this shock transient, achieved at $z = 1.1L_d$, is 1.36 fs. The beam focusing geometry in these simulations is adjusted in such a way as to enhance pulse compression and to avoid any noticeable ionization effects. Comparison of the simulations performed using the full model of Eqs. (2.8)–(2.11) [filled circles in Fig. 5.1(b)] with simulations where ionization, high-order nonlinearity and ionization, or dispersion effects were switched off [open circles, triangles, and rectangles in Fig. 5.1(b)] shows that the minimum pulse width of the shock transient, arising on the

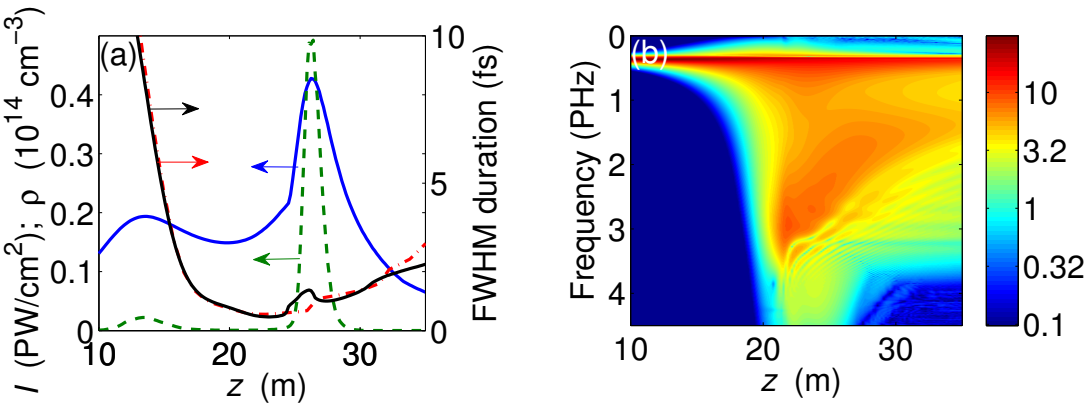

Figure 5.2 (a) the maximum field intensity (solid line, left axis), the maximum electron density (dashed line, left axis), the on-axis FWHM pulse width after spectral filtering (solid line, right axis) and FWHM pulse width of the spectrally filtered field integrated over the beam (dash-dotted line, right axis) as functions of the propagation distance z and (b) the field spectrum on the beam axis for $\lambda_0 = 800$ nm, $\tau_p = 30$ fs, $f = 0.65L_d$, and $P_0 = 0.8P_{cr}$ in helium at $p = 0.02$ bar. From P. A. Zhokhov and A. M. Zheltikov, 2013 [2].

trailing edge of the pulse, is controlled by the tradeoff of the effects related to dispersion, high-order nonlinearities, and, to some extent, ionization. For tightly focused beams [small R in Fig. 5.1(b)], high-order nonlinearities and ionization effects limit the pulse width. In the regime of loose focusing large R in Fig. 5.1(b)], dispersion effects start to play a significant role, limiting the minimum pulse width of the shock transient.

When the effects of impact ionization are negligible (which is the case within a broad range of parameters, including the regime considered here), the spatiotemporal field dynamics leading to the generation of ultrashort optical shocks can be scaled in the peak power through a coordinated adjustment of the gas pressure $p \propto P^{-1}$, the input beam diameter $d_0 \propto P^{1/2}$, and the focal length $f \propto P$. As a specific example of high-power attosecond shock generation, we consider the evolution of laser pulses

with a central wavelength $\lambda_0 = 800$ nm and an input pulse width of 30 fs ($\tau_0 = 70$), corresponding to a typical output of mode-locked Ti: sapphire lasers. The input pulse energies are set equal to 43 mJ and 50 mJ, corresponding to input peak powers P_0 of 1.36 TW and 1.7 TW at a helium pressure $p = 0.02$ bar. With the input beam diameter and the linear focal length taken equal to $d_0 = 2.9$ mm and $f = 15.5$ m, the maximum electron density generated by the laser pulse is 5x10^{13} cm^{-3}, and the longitudinal profiles of the field intensity and electron density along the beam path [Fig. 5.2(a)] drastically differ from typical field intensity and electron density profiles with extended plateaus observed in the filamentation regime [18, 19].

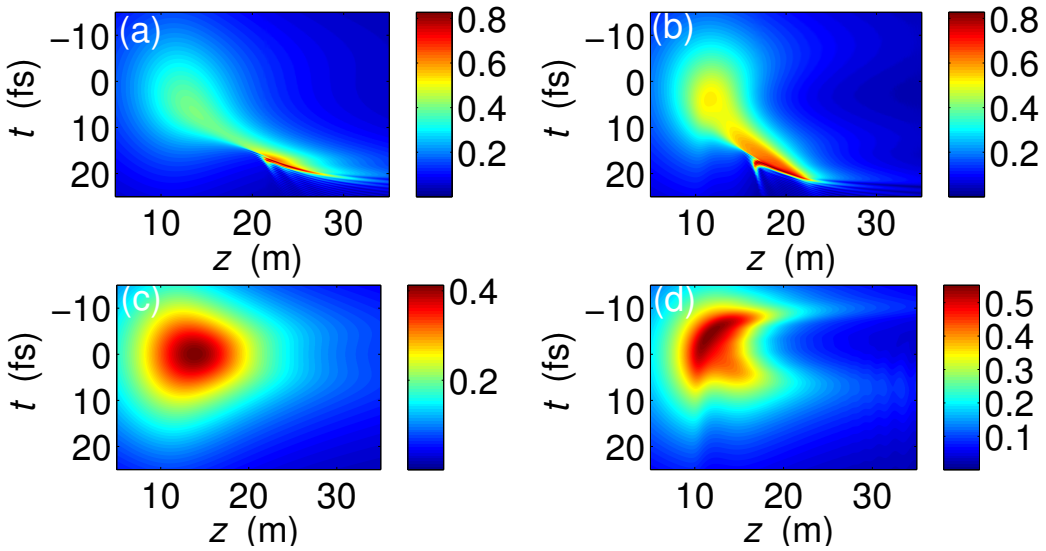

Figure 5.3 Spatiotemporal maps of the on-axis field (in GV/cm), calculated with (a), (b) and without (c), (d) the shock term in Eq. (2.16) for the initial central wavelength $\lambda_0 = 800$ nm, input pulse width $\tau_p = 30$ fs, $f = 0.65L_d$, and input peak power $P_0 = 0.8P_{cr}$ (a), (c) and $P_0 = P_{cr}$ (b), (d) in helium with $p = 0.02$ bar. From P. A. Zhokhov and A. M. Zheltikov, 2013 [2].

To isolate the shock-wave effects in the generation of an ultrashort peak on the

trailing edge of the pulse, seen in Figs. 5.3(a) and 5.3(b), we performed simulations with the shock operator T in Eqs. (2.16) replaced by the identity operator. With the shock-wave effects switched off, a drastically different type of field evolution is observed [Figs. 5.3(c), 5.3(d)]. For peak powers below P_{cr} [$P = 0.8P_{cr}$ in Fig. 5.3(c)], the pulse retains its symmetric shape, as the peak of the pulse propagates with the same group velocity as its edges. As the peak power approaches P_{cr}, ionization effects become noticeable, defocusing the trailing edge of the pulse [Fig. 5.3(d)]. Generation of an ultrashort pulse is not observed in any of these regimes when the shock term is disabled.

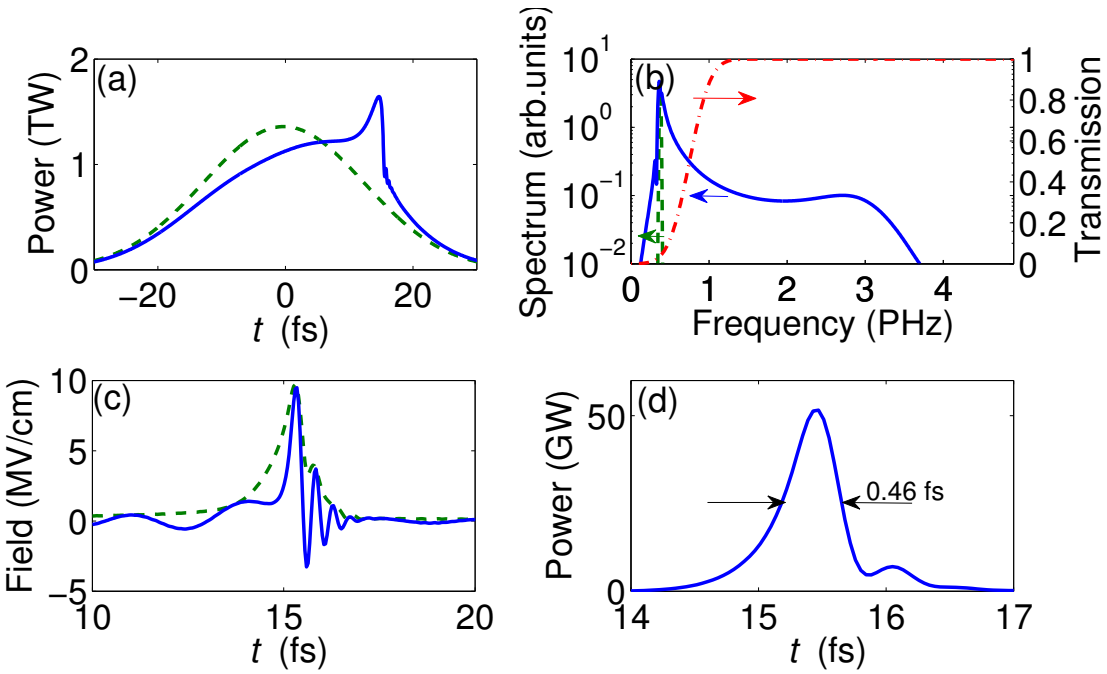

Figure 5.4 (a), (b) The pulse power integrated over the entire beam and the spectrum of the pulse on the beam axis at $z = 0$ (dashed line, left axis) and 20 m (solid line, left axis). Also shown are the transmission of the filter (dotted line, right axis). (c) The electric field on the beam axis (solid line) and the pulse envelope (dashed line) at $z = 20$ m; (d) the pulse envelope integrated over the entire beam behind the filter for $\lambda_0 = 800$ nm, $\tau_p = 30$ fs, $f = 0.65L_d$, and $P_0 = 0.8P_{cr}$ in helium at $p = 0.02$ bar. From P. A. Zhokhov and A. M. Zheltikov, 2013 [2].

The shock term, as can be seen from Figs. 5.3(a) – 5.3(d), tends to push the most intense part of the pulse toward its trailing edge, giving rise to subfemtosecond shock transients on the back of the pulse [seen at $15 < t < 20$ fs in Figs. 5.3(a), 5.3(b)]. The physics behind shock-wave formation in this regime is intuitively clear, as the highest-intensity fraction of the pulse propagates slower than its edges due to the positive Kerr-effect-induced change in the group index of the gas. Unlike 1D shock waves, 3D shock transients can evolve toward much shorter, attosecond pulse widths due to a strongly coupled dynamics of the optical field in space and time. Specifically, in the regime illustrated by Fig. 5.3(a), a shock wave tends to increase the field intensity on the trailing edge of the pulse, enhancing the self-focusing of this portion of the waveform (Fig. 5.5). Since the field intensity on the leading edge of the pulse is much lower, this part of the pulse undergoes strong diffraction, facilitating the generation of an ultrashort shock transient. Enhancement of pulse compression due to self-steepening on the trailing edge of the pulse is confirmed by numerical simulations performed with and without the shock-wave term in Eq. (2.16) (Fig. 5.5). At the point of maximum pulse compression [$z = 26$ m in Fig. 5.3(a)], an ultrashort shock is tightly confined to the pulse section where the beam size is minimal due to the most efficient self-focusing.

The field waveform produced as a result of this spatiotemporal field dynamics features an extremely short peak on a long pedestal [Fig. 5.4(a)]. The spectrum of this pedestal is centered around the input spectrum [shown by the dashed line in Fig. 5.4(b)], while its temporal power profile follows the input pulse [the dashed line in Fig. 5.4(a)] slightly distorted by the shock wave. The spectrum of the ultrashort peak at $15 < t < 20$ fs in Fig. 5.3(a) displays a strong blue shift [Figs. 5.2(b), 5.4(b)], translating into a strong chirp of the electric field on the beam axis [Fig. 5.4(c)]. Due to this spectral shift, the ultrashort shock wave can be separated from the pedestal

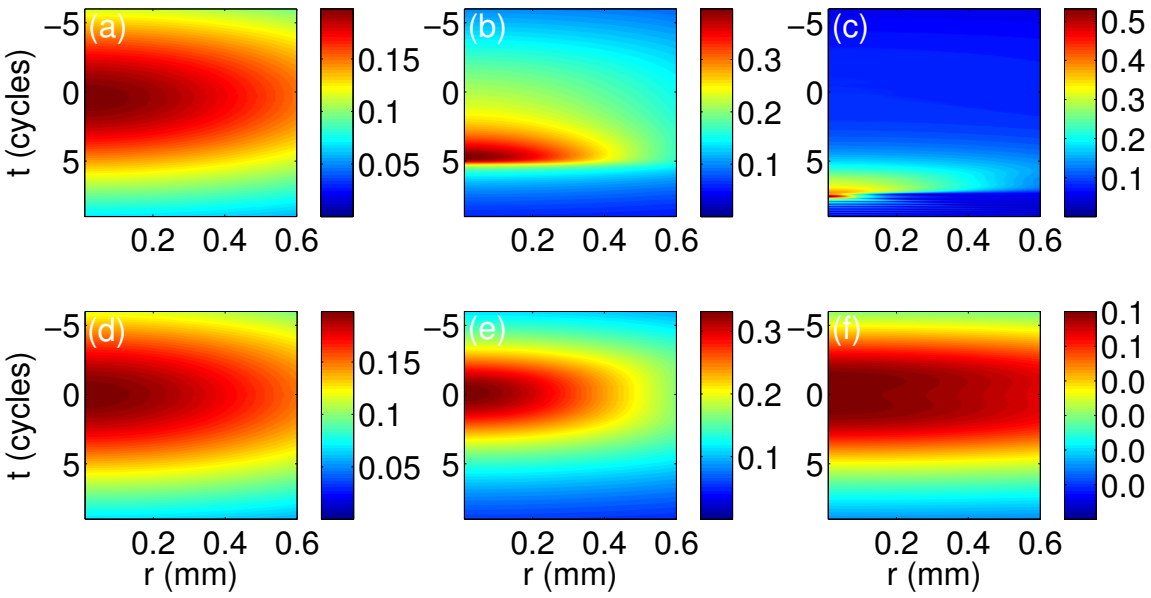

Figure 5.5 Maps of the intensity (PW/cm^2) in the (r, t) coordinates simulated with (a), (b), (c) and without (d), (e), (f) the shock-wave term for (a), (d) $z = 10$ m, (b), (e) $z = 16$ m, (c), (f) $z = 22$ for $\tau_p = 30$ fs, $P_0 = 0.8P_{cr}$, $f = 0.65L_D$, $p = 0.02$ bar. From P. A. Zhokhov and A. M. Zheltikov, 2013 [2].

through spectral filtering. In contrast to filamentation compression schemes, where the laser fluences are prohibitively high for a direct intrafilament filtering of the compressed pulse, the laser fluence around the point of maximum pulse compression in our scheme is below 2 J/cm^2, which allows a spectral filter to be inserted in the laser beam at $z = 21$ m to block the spectrum of the pedestal [as shown by the dash-dotted line in Fig. 5.4(b)] and to produce an extremely short shock transient across the entire beam with the FWHM pulse width estimated, following the integration over the beam, as 460 attoseconds. The maximum field intensity in this 0.46-fs pulse is about 2×10^3 times higher than the intensity of a prepulse 15 fs before the peak and 1.6×10^4 times higher than the postpulse intensity 15 fs after the peak. The total energy carried by this 0.46-fs shock wave is 0.03 mJ, translating into a peak power

of 52 GW. The FWHM pulse width in the spectrally filtered shock wave calculated as a function of the propagation path is shown in Fig. 5.2(a). The integral pulse width of the compressed shock transient across the entire beam [dash–dotted curve in Fig. 5.2(a)] closely follows the on-axis beam intensity, shown by the solid line in this figure. Equations (2.8) and (2.16) is still valid for such field transients since all the necessary conditions for the applicability of these equations, $\frac{1}{|A|}|\frac{\partial A}{\partial z}| \ll k_0$ and $|k_0 - \frac{\omega_0}{V}| \ll k_0$, are satisfied, with $k_0 = \frac{\omega_0}{c} n(\omega_0)$ [42]. Indeed, for the regime where attosecond shock transients are generated, we have $\max\left\{\frac{1}{|A|}|\frac{\partial A}{\partial z}|\right\} \approx 10$ cm^{-1} and $|k_0 - \frac{\omega_0}{V}| \approx 0.05$ cm^{-1}, while $k_0 \approx 8 \times 10^4$ cm^{-1}.

A broad transparency range free of any electronic resonances is critical for attosecond shock wave generation as it helps reduce absorption, dispersion-induced pulse stretching and precursor formation [80]. For helium, the first electronic resonance corresponds to the $1s-2p$ transition and occurs at $\nu_{1s-2p} \approx 5.13$ PHz. For the attosecond shock transient in Fig. 5.4(d), the high-frequency part of the spectrum falling beyond ν_{1s-2p} carries less than 10^{-11} of the total radiation energy and less than 10^{-5} of the energy of the attosecond waveform behind the spectral filter. Under these conditions, effects related to precursor formation are negligible.

Unlike laser-induced filaments, where few-cycle field transients are generated as a part of an ultrafast strongly coupled spatiotemporal dynamics, which stretches these transients within extremely short propagation paths, attosecond optical shock waves demonstrated in this work are generated with loosely focused beams, at low gas pressures, and in the regime where ionization effects are negligible. Due to all these factors, such waveforms maintain their pulse widths over much longer propagation paths. Specifically, at $p = 0.02$ bar, the 0.46-fs field waveform shown in Fig. 4(d) remains shorter than 0.65 fs within a propagation path of 70 cm, allowing this field waveform to be extracted from a gas medium with an appropriate pressure gradient,

thus making it suitable as a subfemtosecond probe for time-resolved experiments.

To summarize, unlike 1D shock waves in optical fibers, 3D shock transients can evolve toward remarkably short, subfemtosecond optical waveforms, suggesting a pulse self-compression scenario whereby multigigawatt attosecond optical waveforms can be synthesized.

6. SCALING LAWS FOR FILAMENTS IN GASES*

Methods of scaling analysis, known since the early days of natural sciences [81], offer powerful tools for in-depth studies of a broad diversity of systems in physics, chemistry, geosciences, biology, and social sciences. Identifying scaling laws for systems with multiparameter, multiple-scale nonlinear dynamics is especially challenging. In nonlinear optical physics, this type of dynamics is found in laser-induced filamentation [16, 18, 19], a specific scenario of spatiotemporal dynamics of optical fields where the beam self-focusing of a high-intensity ultrashort optical pulse is balanced by defocusing due to the radial profile of the electron density induced by ultrafast ionization, giving rise to a self-channeling-type propagation of laser radiation. Besides offering an intriguing example of unique ultrafast nonlinear dynamics, laser-induced filamentation enables long-distance transmission of high-intensity ultrashort pulses [82], suggests a powerful strategy for pulse compression to extremely short [83, 84], in certain cases subcycle [71], pulse widths, allows remotely pumped lasing [85], and opens new horizons in standoff detection [21].

Important scaling laws for some of the key physical processes contributing to laser-induced filamentation are known from the classical earlier work on laser–matter interaction and nonlinear-optical physics. In his seminal 1964 work [13], Keldysh has derived a closed-form expression allowing the photoionization rate to be calculated as a function of the laser intensity. On the beam dynamics side, Bespalov and Talanov [28] have offered important insights into small-scale filamentation of high-power laser beams, while Marburger [17] has derived a semi-analytical formula for the position of the nonlinear focus as a function of the peak power. However, in laser-induced

*Section reprinted with permission from "Scaling laws for laser-induced filamentation" by P. A. Zhokhov and A. M. Zheltikov, [3]

filamentation, all these tendencies, identified earlier for isolated physical processes, are manifested as a part of complex spatiotemporal field evolution, involving strongly coupled waveform transformations in space and time, where the beam dynamics is not uniform within the laser pulse and the beam often undergoes multiple refocusing cycles. As a consequence, a simple combination of analytical results and physical intuition available for some of the processes involved in laser-induced filamentation fail to adequately describe the properties of the laser field in a filament and even to explain the most prominent effects observed in a laser filament.

In this section, we show that, despite all the complexity of the underlying nonlinear physics, the filamentation of ultrashort optical field waveforms obeys a set of physically instructive scaling laws, applicable within a remarkably broad range of laser powers, pulse widths, gas pressures, and propagation paths [3]. The scalability of the key physical effects contributing to laser-induced filamentation will be identified with the use of the relevant field-evolution and ionization-dynamics equations and verified by supercomputer simulations, suggesting practical recipes for the power scaling of filamentation-based pulse compression.

To isolate the pressure dependence of physical parameters in Eqs. (2.2)–(2.8), we write

$$\rho_{at} = p/p_0 \; \overline{\rho}_{at}, \tag{6.1}$$

$$\rho = p/p_0 \; \overline{\rho}_e, \tag{6.2}$$

$$R_i[A] = p/p_0 \; \overline{R}_i[A]. \tag{6.3}$$

where p is the gas pressure, p_0 is the atmospheric pressure, and the bar indicates that a physical parameter is taken at $p = p_0$. The dielectric susceptibilities (both linear $\chi^{(1)}$, and nonlinear $\chi^{(3)}$) are proportional to the number of atoms per unit

volume, and thus, to the gas pressure. The linear refractive index $n(\omega)$ is given by $n(\omega) = \sqrt{1+\chi^{(1)}(\omega)}$. Since for gases the refractive index is very close to unity, we can write $n(\omega) \approx 1 + \chi^{(1)}(\omega)/2$. The group index that determines the group velocity at the central frequency of the pulse is then $n_g(\omega_0) = n(\omega_0) + \omega_0 \left(\frac{\partial n}{\partial \omega}\right)_{\omega_0} \approx 1 + \frac{\chi^{(1)}(\omega_0)}{2} + \frac{\omega_0}{2}\left(\frac{\partial \chi^{(1)}}{\partial \omega}\right)_{\omega_0}$. Therefore, $D(\omega) = k(\omega) - \frac{\omega}{V} = \frac{\omega}{c}\left(n(\omega) - n_g(\omega_0)\right) \approx \frac{\omega}{c}\left(\frac{\chi^{(1)}(\omega)}{2} - \frac{\chi^{(1)}(\omega_0)}{2} - \frac{\omega_0}{2}\left(\frac{\partial \chi^{(1)}}{\partial \omega}\right)_{\omega_0}\right)$. We see that $\hat{D}$ is proportional to $\chi^{(1)}$ and, thus, proportional to the gas pressure

$$\hat{D} = p/p_0 \; \overline{D}. \tag{6.4}$$

On the other hand, according to (2.3), n_2 is proportional to $\chi^{(3)}$ and inversely proportional to $k(\omega)$. $k(\omega)$ is almost independent of the gas pressure because gas refractive index is very close to unity, thus, the nonlinear refractive index n_2 is proportional to the gas pressure. Similarly, n_4 and χ_{TH} are proportional to the gas pressure:

$$n_2 = p/p_0 \; \overline{n}_2, \tag{6.5}$$

$$n_4 = p/p_0 \; \overline{n}_4, \tag{6.6}$$

$$\chi_{TH} = p/p_0 \; \overline{\chi}_{TH}. \tag{6.7}$$

Therefore,

$$R_{nl} = p/p_0 \; \overline{R}_{nl} \tag{6.8}$$

Let us now introduce dimensionless coordinates $\xi = x/a, \zeta = y/a, \eta = z/L_D$, and $\tilde{\nabla}_\perp^2 = \frac{\partial^2}{\partial \xi^2} + \frac{\partial^2}{\partial \zeta^2}$, where a is the input beam radius, and $L_D = \frac{k(\omega_0)a^2}{2}$ is the diffraction

length, in order to rewrite Eq. (2.8) as

$$\frac{\partial A}{\partial \eta} = iT^{-1}\frac{\tilde{\nabla}_{\perp}^{2}A}{4} + \frac{p}{p_0}L_D\left(i\overline{D}A + \overline{R}_i[A] + \overline{R}_{nl}\right). \tag{6.9}$$

Eq. (6.9) is pivotal in revealing important scaling laws for pulse propagation dynamics. Mathematically, this equation remains invariant as long as the product pL_D is kept constant. In terms of physical parameters, this implies that variations in the input beam radius a are coordinated with the gas pressure in such a way that pa^2 is constant. All the nonlinear-optical effects included in Eq. (6.9) scale uniformly with such a transformation. Since the diffraction term in Eq. (6.9) involves second-order derivatives in ξ and ζ, the invariance of the diffraction term in the field evolution equation written in terms of real-physical-space variables x and y dictates that the beam focusing length f should be varied jointly with a as $f \propto a^2$. Thus, if $A_s(t,\xi,\zeta,\eta)$ is a solution to the field evolution equation (6.9) subject to the initial condition $A_s(t,\xi,\zeta,\eta=0) = A_0(t,\xi,\zeta)$ for $a = a_1$, $p = p_1$, and $f = f_1$, then it will be also a solution to Eq. (6.9) with the same initial condition for all a, f, and p such that $pa^2 = p_1a_1^2$ and $a^2/f = a_1^2/f_1$.

Finally, with the peak power of the input laser pulse represented as

$$P = a^2 \max_t \left\{ \int_{-\infty}^{\infty}\int_{-\infty}^{\infty} |A_0(t,\xi,\zeta)|^2 d\xi d\zeta \right\}, \tag{6.10}$$

the initial condition $A_s(t,\xi,\zeta,\eta=0) = A_0(t,\xi,\zeta)$ remains constant when the gas pressure and the beam focusing length are changed jointly with P as $p \propto P^{-1}$ and $f \propto P$.

We thus conclude that joint variations in a, p, and f keep the solution to Eq.

(6.9) invariant as long as

$$pP = const, \tag{6.11}$$

$$pa^2 = const, \tag{6.12}$$

$$pf = const. \tag{6.13}$$

Equations (6.11) – (6.13) express the key scaling laws for pulse propagation dynamics. Since the critical power of self-focusing, $P_{cr} = \lambda_0^2 \left[2\pi n_2\right]^{-1} = \lambda_0^2 p_0 \left[2\pi p \overline{n}_2\right]^{-1}$, where $\lambda_0 = 2\pi c/\omega_0$, scales as p^{-1} with the gas pressure, Eq. (6.11) is consistent with the common wisdom that the P/P_{cr} ratio has to be kept constant for the invariance of the spatiotemporal field dynamics in the filamentation regime. However, we can now see from Eqs. (6.11) – (6.13) that the $P/P_{cr} = const$ condition is necessary, but not sufficient to keep the beam dynamics constant.

When applied jointly with Eq. (6.11), the condition of Eq. (6.12) is equivalent to keeping the peak pulse intensity constant while allowing the pressure to be variable. Although simple in its form, this result is not trivial at all if not counterintuitive as it shows that, while the gas pressure is changing, one needs to keep the intensity constant instead of trying to compensate for a change in nonlinearity caused by a variation in p. However, it is Eq. (6.13) that is, perhaps, the most intriguing of all the scaling rules. Indeed, the focusing length f is a freely variable parameter. It is remarkable, therefore, that Eq. (6.13), requires the product of f and p be constant. As explained above, Eq. (6.12) combined with Eq. (6.13) provides the invariance of the diffraction term in the field evolution equation. Eqs. (6.11) and (6.13), in their turn, require the invariance of the initial beam and envelope profiles, highlighting the importance of the initial conditions for the scalability of spatiotemporal field dynamics.

Avalanche ionization, which cannot be included as a scalable term into the equations of pulse propagation dynamics, sets a limitation on the applicability range of the scaling rules (6.11) – (6.13). This process becomes important when the electron collision time, $\tau_c = \overline{\tau}_c \frac{p_0}{p}$, becomes less than the pulse width τ_0, leading to the following limitation on the gas pressure:

$$p < p_a = \frac{\overline{\tau}_c}{\tau_0} p_0 \tag{6.14}$$

For a laser pulse with $\tau_0 = 30$ fs propagating in argon, where $\overline{\tau}_c = 190$ fs, the avalanche ionization starts to play a significant role for gas pressures above $p_a = 6.3$ bar.

We now verify the scaling laws (6.11) – (6.13) by numerical simulations using Eqs. (2.1) – (2.6) with the impact ionization term included for the representative regimes of laser-induced filamentation. We examine two representative regimes of filamentation-assisted pulse self-compression [27, 25], which yield drastically different types of spatiotemporal waveform dynamics (Fig. 6.1) and electron density profiles (Figs. 6.2,6.3). In the first regime, an initially collimated laser beam with an input FWHM pulse width $\tau_0 = 30$ fs and a central wavelength $\lambda_0 = 800$ nm propagates in argon with $U_i = 15.75$ eV, $\overline{n}_2 = 1.74 \times 10^{-19}$ cm^2/W, $\overline{\tau}_c = 190$ fs, $f_R = 0$ and linear dispersion modeled with the standard reference data [53]. As shown by Bergé [27], pulse compression to single-cycle pulse widths can be achieved in this regime of filamentation. This prediction is fully supported by the results of our numerical simulations [Figs. 6.1(a), 6.1(c), 6.2(e), 6.2(f)].

In the second regime studied here, an ultrashort optical waveform displays a well-resolved refocusing cycle [Fig. 6.1(b),(d)], accompanied by efficient pulse self-compression due to pulse self-steepening and space–time focusing [25]. This fila-

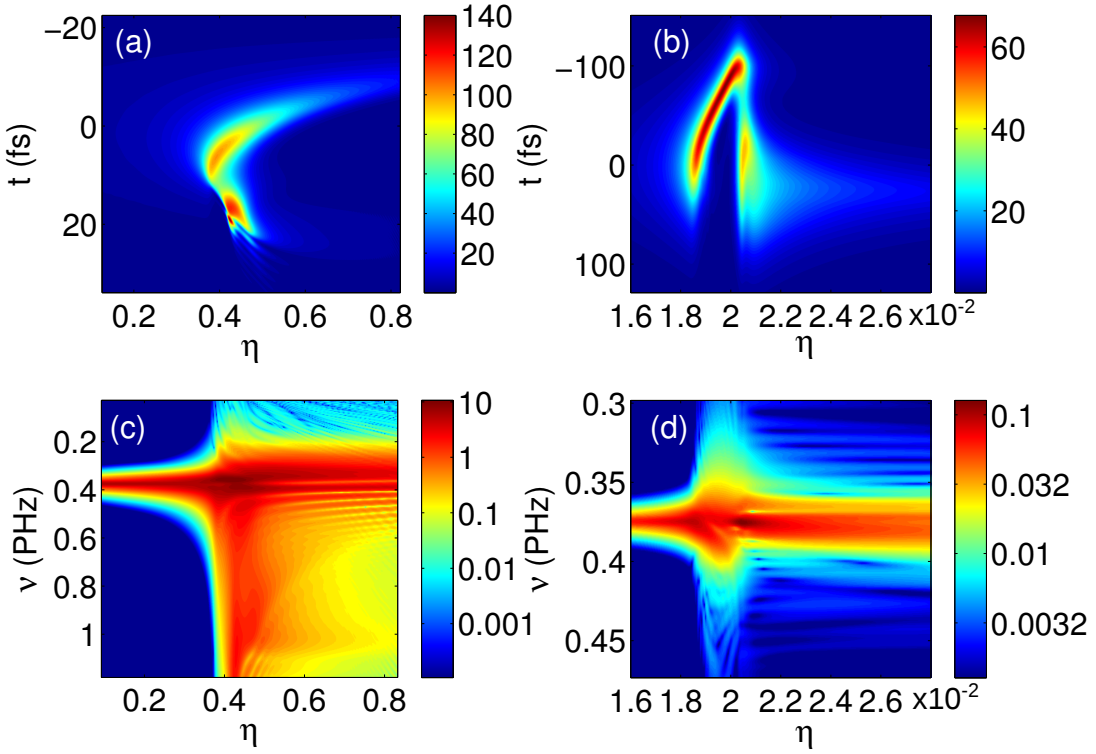

Figure 6.1 The maps of (a), (b) on-axis field intensity and (c), (d) on-axis spectral intensity for laser pulses with (a), (c) $\tau_0 = 30$ fs, $a = 0.5$ mm in an initially collimated beam, and $P = 3P_{cr}$ and (b), (d) $\tau_0 = 115$ fs, $a = 2.5$ mm, $f = 0.02L_D = 0.5$ m, and $P = 4.6P_{cr}$ in (a), (c) argon and (b), (d) krypton at a gas pressure of 1 bar. From P. A. Zhokhov and A. M. Zheltikov, 2014 [3]

mentation regime is achieved in our simulations by focusing a laser beam with an input FWHM pulse width of 115 fs, a central wavelength $\lambda_0 = 800$ nm and focusing distance $f = 0.02L_D$ in krypton with $U_i = 14$ eV, $\overline{n}_2 = 3 \times 10^{-19}$ cm^2/W, $\overline{\tau}_c = 200$ fs, and $f_R = 0$.

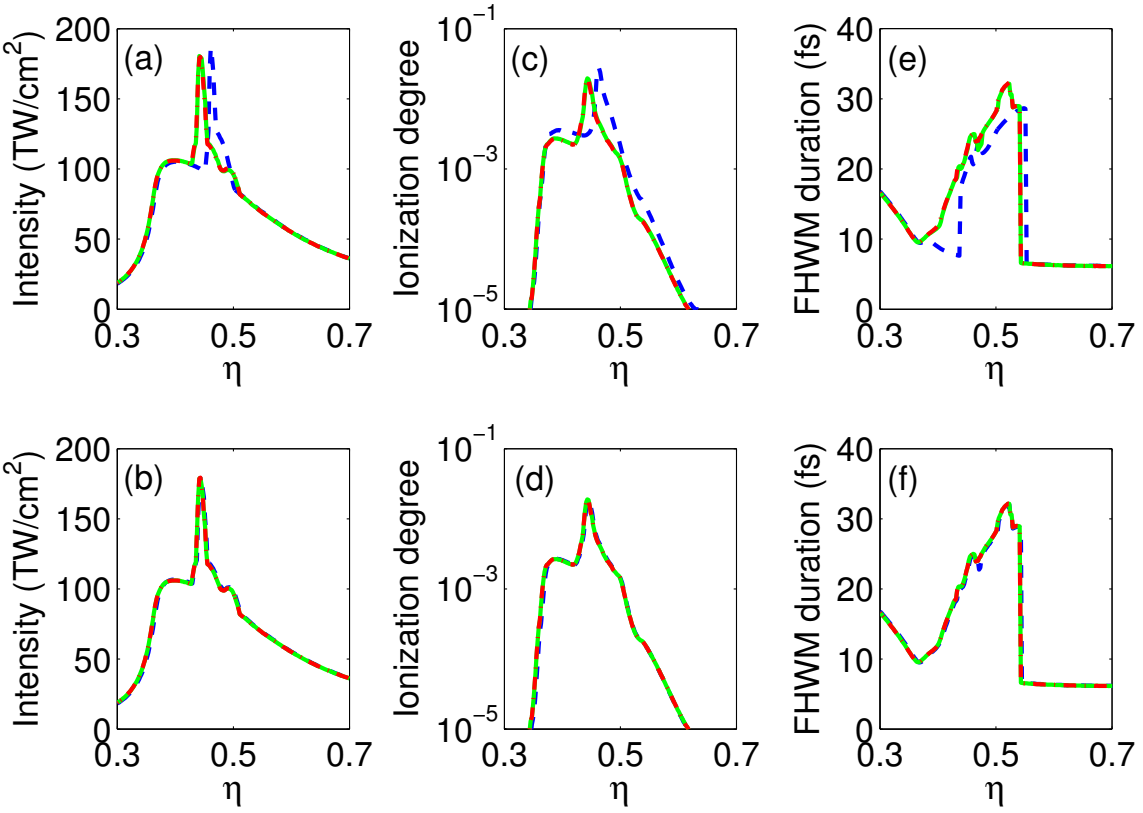

Figure 6.2 The on-axis field intensity (a),(b), ionization degree $Z = \frac{N_e}{N_{at}}$ (c), (d) and the on-axis pulse FWHM duration (e),(f) for a laser pulse propagating in argon $\tau_0 = 30$ fs in an initially collimated beam with $a = 0.1$ mm, $L_D = 4$ cm, $P = 0.7$ GW, $p = 25$ bar (blue dashed line); $a = 0.5$ mm, $L_D = 1$ m, $P = 18$ GW, $p = 1$ bar (green solid line); and $a = 1.9$ mm, $L_D = 14$ m, $P = 250$ GW, $p = 0.07$ bar (red dash–dotted line) with (a),(c),(e) and without (b),(d),(f) avalanche ionization. From P. A. Zhokhov and A. M. Zheltikov, 2014 [3]

Dynamics of an ultrashort laser pulse in the first regime is illustrated in Figs.

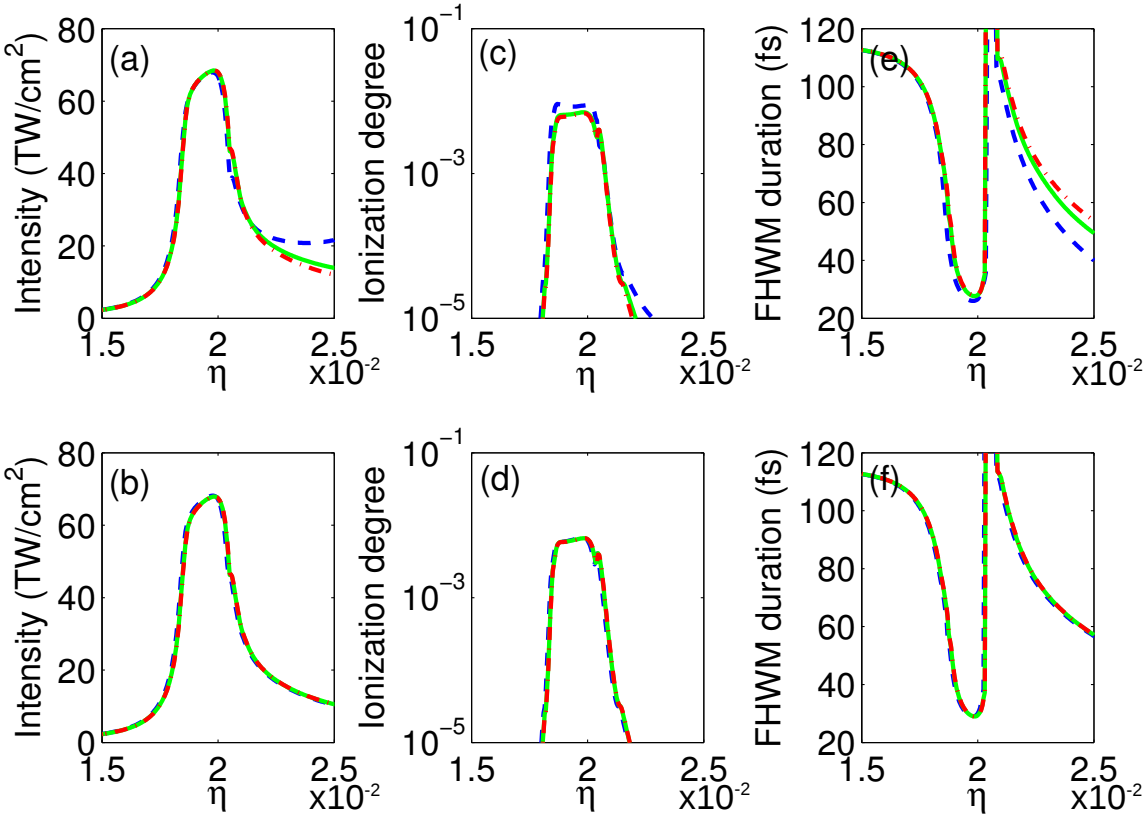

Figure 6.3 The on-axis field intensity (a),(b), ionization degree $Z = \frac{N_e}{N_{at}}$ (c), (d) and the on-axis pulse FWHM duration (e),(f) for a laser pulse propagating in krypton with $\tau_0 = 115$ fs; $a = 0.83$ mm, $L_D = 2.7$ m, $f = 5.5$ cm, $P = 1.6$ GW, $p = 10$ bar (blue dashed line); $a = 2.5$ mm, $L_D = 24$ m, $f = 0.5$ m, $P = 15$ GW, $p = 1$ bar (green solid line); and $a = 8.3$ mm, $L_D = 270$ m, $f = 5.5$ m, $P = 160$ GW, $p = 0.1$ bar (red dash–dotted line) with (a),(c),(e) and without (b),(d),(f) avalanche ionization. From P. A. Zhokhov and A. M. Zheltikov, 2014 [3]

6.1(a) and 6.1(c). The laser field with an input intensity of 3.2 TW/cm^2 and an input peak power $P = 3P_{cr}$ is seen to exhibit a typical filamentation dynamics, featuring supercontinuum generation [for $\eta > 0.4$ in Fig. 6.1(c)] and evolving toward a few-cycle field waveform [for $\eta > 0.5$ in Figs. 6.1(a), 6.2(e)], in agreement with the earlier predictions for this regime of filamentation [27]. In Fig. 6.2, we show the longitudinal profiles of field intensity I, ionization degree $\langle Z \rangle = \rho/\rho_{at}$, and FWHM

pulse width τ_p on the beam axis calculated for different values of the input beam radius a, the input peak power P, and the gas pressure p, varied in a coordinated fashion so that Eqs. (6.11) and (6.12) are satisfied [for a collimated beam, Eq. (6.13) is fulfilled with any finite gas pressure p]. For gas pressures below p_a, simulations yield identical longitudinal profiles of I [Figs. 6.2(a), 6.2(b)], Z [Figs. 6.2(c), 6.2(d)], and τ_p [Figs. 6.2(e), 6.2(f)] for any set of parameters meeting Eqs. (6.11) – (6.13), thus indicating the validity of the scaling rules expressed by these conditions within a broad range of the relevant parameters. As an important consequence, filamentation regimes enabling pulse self-compression to single-cycle pulse widths can be achieved within a broad range of peak powers through an appropriate adjustment of the input beam parameters and the gas pressure [Figs. 6.2(e), 6.2(f)]. For gas pressures $p > p_a$, avalanche ionization starts to play a noticeable role, distorting the longitudinal profiles of I, Z, and τ_p. These distortions are clearly seen (Fig. 6.2) from the comparison of simulations performed with and without the avalanche ionization term in the pulse propagation equations. Figs. 6.2(a),(c) show the on-axis intensity and ionization degree $\langle Z \rangle = \frac{\rho}{\rho_{at}}$ as functions of unitless propagation distance η for different input beam radii a – 0.1 mm, 0.5 mm and 1.9 mm, which correspond to pulse powers P equal to 0.7 GW, 18 GW and 250 GW and pressures p equal to 25 bar, 1 bar and 0.07 bar respectively. The ratio of input power P to the critical power of self-focusing P_{cr} is $P/P_{cr} = 3$, and input intensity is 3.2 TW/cm^2.

In the second regime of filamentation-based pulse compression studied here, the ratio of the input peak power to the critical power of self-focusing is higher than in the first regime considered above, enabling the refocusing of the trailing part of the pulse and leading to efficient pulse self-compression [Figs. 6.1(b), 6.3(e), 6.3(f)] as a result of self-steepening and space-time focusing [25]. The temporal envelope of the pulse in this regime exhibits a prominent defocusing of its trailing part at

$\eta \approx 2\times10^{-2}$, followed by refocusing and generation of an ultrashort ($\approx$ 30 fs FWHM) field waveform on the back of the pulse [Figs. 6.1(b), 6.3(e), 6.3(f)].

With $\tau_0 = 115$ fs and $\overline{\tau}_c = 200$ fs for krypton, the avalanche ionization remains weak in this regime for gas pressures below $p_a \approx 1.7$ bar. In this range of gas pressures, numerical simulations with Eqs. (2.1) – (2.6) give identical longitudinal profiles of field intensity [Figs. 6.3(a), 6.3(b)], ionization degree [Figs. 6.3(c), 6.3(d)], and FWHM pulse width [Figs. 6.3(e), 6.3(f)] for any set of input laser beam parameters varied in such a way that Eqs. (6.11) – (6.13) are satisfied. Well-pronounced intensity clamping is clearly seen in Figs. 6.3(a) – 6.3(d). For gas pressures above p_a, effects related to the avalanche ionization are no longer negligible. These effects, as can be seen from simulations performed with and without the avalanche ionization term (Fig. 6.3), tend to accumulate toward the rear part of the filament, generating higher electron densities [Fig. 6.3(c)] and providing higher field intensities [Fig. 6.3(a)] and shorter pulse widths [Fig. 6.3(e)] in this section of the filament.

We will now illustrate, by means of numerical simulations, that the P/P_{cr} ratio alone is in no way sufficient to fully control or scale filamentation dynamics. To this end, we vary the gas pressure and parameters of the input laser field in such a way as to keep the P/P_{cr} ratio constant, thus fulfilling Eq. (6.11), but the focusing conditions change, implying that Eq. (6.13) is not satisfied. As can be seen from Figs. 6.4(a) – 6.4(d), although the P/P_{cr} ratio is kept constant in all the simulations, variations in the focusing length can give rise to striking changes in field dynamics. Indeed, in the regime of tight focusing, $f = 0.4L_D$ [Fig. 6.4(a)], the electron density induced by the laser beam near the linear focus is high enough to defocus the laser beam to the extent of complete suppression of filamentation. When the focusing is too loose, on the other hand, $f = 2L_D$ [Fig. 6.4(d)], dispersion-induced stretching decreases the field intensity, also preventing filamentation. Because of these effects,

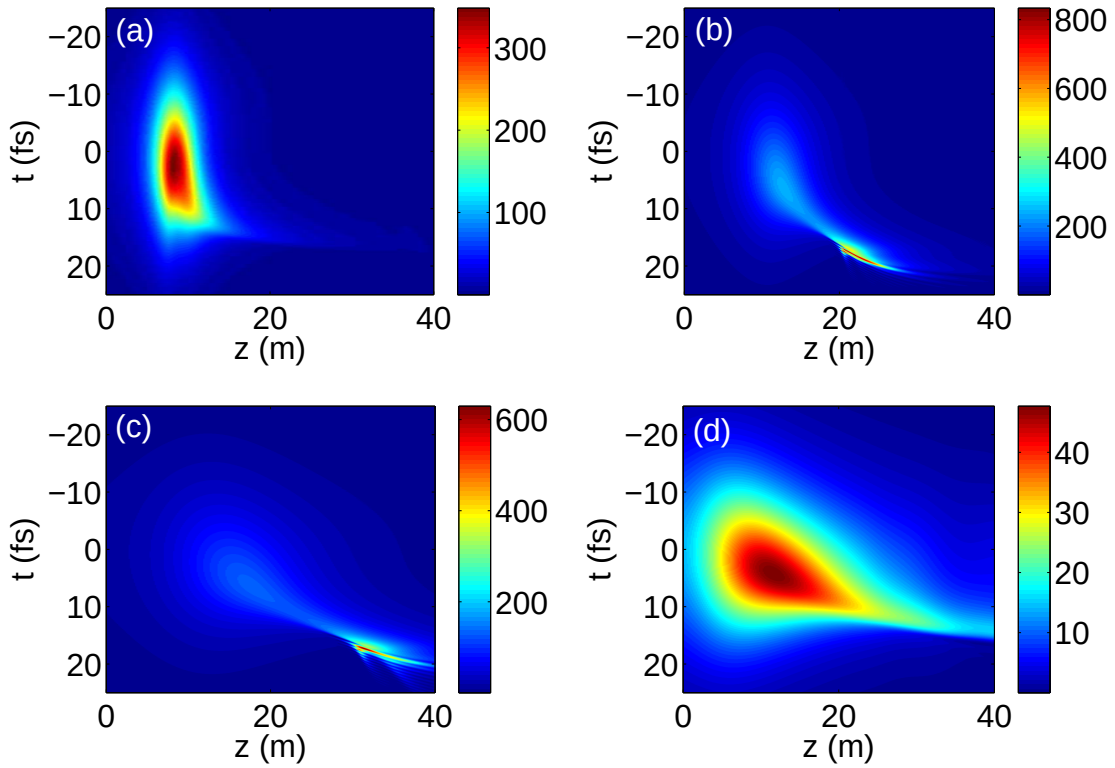

Figure 6.4 The on-axis field intensity ($\times 10^{12}$ W/cm^2) as a function of time t and propagation coordinate z in helium at $p = 0.02$ bar, $a = 2.9$ mm, $P = 1.4$ TW ($0.8\ P_{cr}$), $\tau_0 = 30$ fs, $\lambda_0 = 800$ nm, and $f = 0.4L_D = 9.5$ m (a), $0.6L_D = 14.3$ m (b), $0.9L_D = 21.4$ m (c), and $2L_D = 47.6$ m (d). From P. A. Zhokhov and A. M. Zheltikov, 2014 [3]

filamentation is only observed within a limited range of focusing lengths, as shown by Figs. 6.4(b) and 6.4(c).

Similarly, when we vary input beam diameter while keeping focusing distance and P/P_{cr} constant, i.e., fulfilling conditions (6.11) and (6.13), but violating the condition (6.12), field dynamics changes dramatically. At small input diameters [Fig. (6.5)(a), (b)] initial stage of self-focusing happens far before the linear focus (consistently with the Marburger formula, [17]), and several self-focusing-free electron defocusing cycles are observed. At larger input diameters [Fig. 6.5(c),(d)] high-intensity area starts close to the linear focus point, refocusing happens once in the trailing part of the pulse, which then propagates with little changes in temporal structure, providing the basis for the filamentation pulse compression regime, described in [25].

In summary, we have identified a set of physically transparent scaling laws for the filamentation of ultrashort laser pulses. We have shown that the intuitively clear $P/P_{cr} = const$ scaling law can be directly derived from the field evolution equation. This scaling law has been shown to be necessary, but not sufficient for an accurate scaling of spatiotemporal field dynamics in the filamentation regime. The full set of scaling laws, as demonstrated in this work, has to include two other physically significant conditions, requiring the invariance of maximum field intensity and beam diffraction. Using this set of scaling laws, we have demonstrated that one of the most significant effects of laser-induced filamentation, viz., pulse compression, is not limited to a single, unique point in the parameter phase space, but can be implemented within a remarkably broad range of laser powers, pulse widths, gas pressures, and propagation paths.

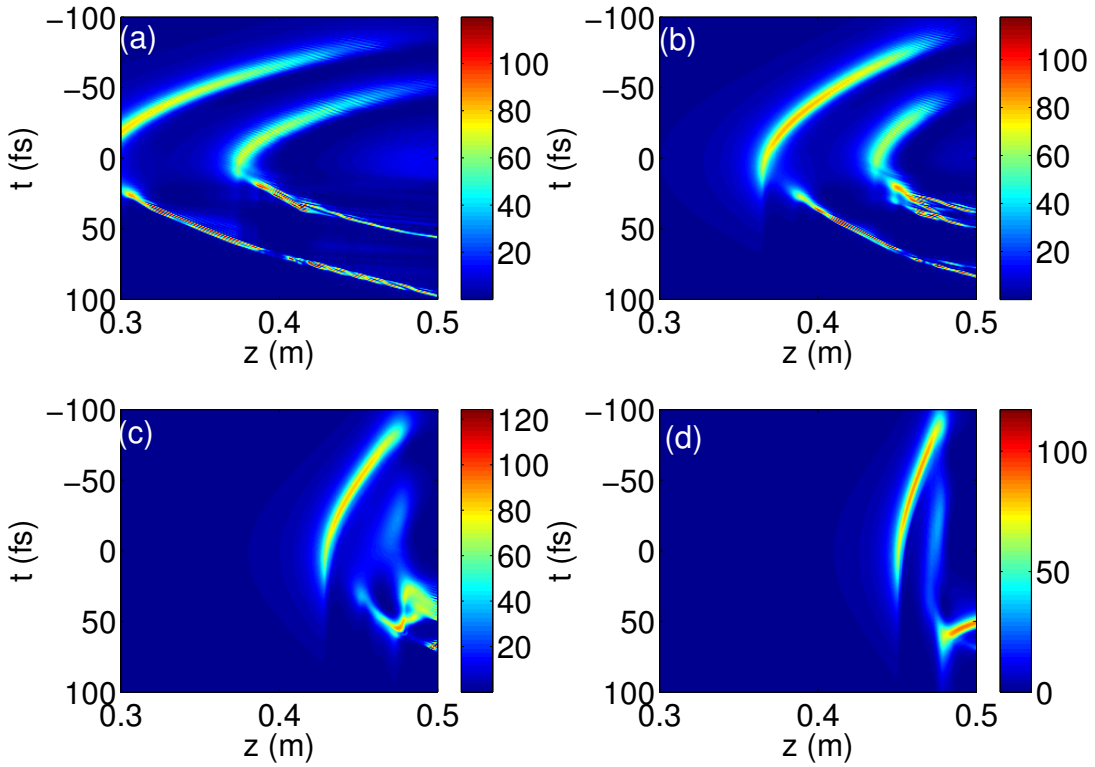

Figure 6.5 The on-axis field intensity ($\times 10^{12}$ W/cm^2) as a function of time t and propagation coordinate z in krypton at $p = 1$ bar,$P = 4.4$ GW (4.6 P_{cr}), $\tau_0 = 115$ fs, $\lambda_0 = 800$ nm, $f = 0.5$ m and (a) $a = 1.0$ mm, (b) $a = 1.5$ mm, (c) $a = 2.5$ mm, (d) $a = 3.5$ mm. From P. A. Zhokhov and A. M. Zheltikov, 2014 [3]

7. FIELD-CYCLE-RESOLVED PHOTOIONIZATION IN SOLIDS: INTRODUCTION

In his seminal 1964 paper [13], Keldysh has presented his celebrated formulas for photoionization, providing a uniform description of multiphoton and tunneling ionization. Over the next five decades, the Keldysh theory of photoionization has been pivotal to the research in laser science, providing a commonly accepted framework for a quantitative analysis of ionization in a remarkable diversity of light–matter interaction phenomena, including laser-induced breakdown [86, 4], high-order harmonic [87] and terahertz [88] generation, as well as filamentation of ultrashort light pulses [19, 18]. While the original Keldysh formulas were intended to describe photoionization in a continuous-wave field, several elegant approaches have been proposed [35, 36, 38] in the context of rapidly progressing ultrafast technologies [8] and attosecond science [10], to include the wave-packet nature of ultrashort driver pulses inducing an ultrafast ionization of gases. These approaches help identify new field-cycle-sensitive phenomena in electron tunneling [89, 90] and develop novel experimental methods for all-optical detection of electron tunneling dynamics [91, 92].

Extension of the Keldysh model to ultrafast photoionization in solids is a standalone challenge in quantum physics. Meeting this challenge not only requires an adequate treatment of broadband driver fields, but also calls for a revision of the standard, hyperbolic model of the electron band structure adopted in the Keldysh formalism. The hyperbolic band model enables an accurate description of weak-field optical properties of solids [14, 93], but fails in the strong-field regime, where effects of zone edges become significant [94]. A Schrödinger-equation treatment with a 1D cosine-type dispersion [95, 39] has been shown to partially address this problem,

offering an adequate framework for the numerical analysis of an important class of ultrafast ionization effects in solids [96]. Still, in the lack of a closed-form solution for the photoionzation rate valid for ultrashort pulses of arbitrary shape, the physical intuition based on the Keldysh theory of photoionization of solids often has to be pushed beyond the range where this theory is rigorously valid, for the sake of compact semianalytical description and overall physical clarity [92, 97, 98].

In this part, we derive a closed-form solution for the nonadiabatic ionization rate in a transparent solid [40], which can be used not only to calculate the probability of ionization in the wake of the pulse and after each field cycle, but also to analyze the behavior of the ionization rate within the field cycle. Our analysis reveals ultrafast ionization dynamics within the field cycle and recovers the results of the Keldysh theory within its range of applicability.

8. GENERAL QUANTUM-MECHANICAL FRAMEWORK*

In this section we will develop a general quatum-mechanical framework that would allow us to analyse photoionization probability and density of photocurrents in two-band dielectrics with arbitrary number of spatial dimensions. Then, in the following section, we will provide specific derivation for a dielectric with cosine-shaped energy-momentum relation (also commonly referred to as a dispersion relation) of electron hole pairs, and approximate formulas for a dielectric with arbitrary spatially separable dispersion relation. Let us consider dielectric in 2-band approximation. States $|v,\ \vec{}k\rangle$ and $|v,\ \vec{}k\rangle$ denote Bloch waves with crystal quasi-momentum $\vec{}k$ in the valence and conduction band, respectively. Let us use $\hbar = |e| = 1$ units, where e is electron charge. Field-free Hamiltonian can be written as

$$H_0 = \sum_{\vec{k}} \mathcal{E}_v(\vec{k})|v,\vec{k}\rangle\langle v,\vec{k}| + \mathcal{E}_c(\vec{k})|c,\vec{k}\rangle\langle c,\vec{k}| \tag{8.1}$$

Sum in (8.1) is performed over all momentum states in the first Brillouin zone (BZ), $\mathcal{E}_v(\vec{k})$ and $\mathcal{E}_c(\vec{k})$ denote energy of the state with momentum $\vec{k}$ in the valence and conduction band, respectively.

The operator of electron coordinate $\vec{R}$ consists of interband and intraband parts. Intraband part is related to classical motion of electron within the band, and as such, can be written as $i\frac{\partial}{\partial\vec{k}}$. Momentum conservation requires that interband part of coordinate operator to connect states with same quasi-momentum, thus, in general,

$$\vec{R} = \sum_{\vec{k}} \vec{X}(k)\left(|c,\vec{k}\rangle\langle v,\vec{k}| + |v,\vec{k}\rangle\langle c,\vec{k}|\right) + i\frac{\partial}{\partial\vec{k}} \tag{8.2}$$

*Parts of this section are reprinted with permission from "Field-cycle-resolved photoionization in solids" by P. A. Zhokhov and A. M. Zheltikov [40]

Time-dependent Hamiltonian of electron in the presence of the field and in the dipole approximation is then (recall that electron charge is -1)

$$H(t) = \sum_{\vec{k}} \mathcal{E}_v(\vec{k})|v,\vec{k}\rangle\langle v,\vec{k}| + \mathcal{E}_c(\vec{k})|c,\vec{k}\rangle\langle c,\vec{k}| + \vec{E}(t)\cdot\vec{R} \tag{8.3}$$

Single-electron wavefunction generally has the form

$$|\psi(t)\rangle = \sum_{\vec{k}} V(\vec{k},t)|v,\vec{k}\rangle + C(\vec{k},t)|c,\vec{k}\rangle \tag{8.4}$$

Time-dependent Shrödinger equation immediately yields partial differential equations (PDEs) for coefficients $C(\vec{k},t)$ and $V(\vec{k},t)$ (we omit $\vec{k},t$ arguments for brevity).

$$\begin{aligned} i\frac{\partial V}{\partial t} &= \mathcal{E}_v(\vec{k})V + \vec{E}(t)\cdot\left(\vec{X}(\vec{k})C + i\frac{\partial V}{\partial \vec{k}}\right) \\ i\frac{\partial C}{\partial t} &= \mathcal{E}_c(\vec{k})C + \vec{E}(t)\cdot\left(\vec{X}(\vec{k})V + i\frac{\partial C}{\partial \vec{k}}\right) \end{aligned} \tag{8.5}$$

Since the PDEs are linear in derivatives both over time and momentum, it is possible to turn them into ordinary differential equations (ODEs) by method of characteristics. Namely, we introduce variable transformation

$$\begin{aligned} \vec{p} &= \vec{k} + \vec{A}(t) \\ \tilde{t} &= t \end{aligned} \tag{8.6}$$

where $\vec{A}(t) = \int_{-\infty}^{t} \vec{E}(t')dt'$ is vector potential. The derivative transformation is then

$$\begin{aligned} \frac{\partial}{\partial \vec{k}} &= \frac{\partial}{\partial \vec{p}} \\ \frac{\partial}{\partial t} &= \frac{\partial}{\partial \tilde{t}} + \vec{E}(t)\cdot\frac{\partial}{\partial \vec{p}} \end{aligned} \tag{8.7}$$

Therefore, (8.5) can be rewritten as (again, we omit $(\vec{p},\tilde{t})$ arguments of V and C for brevity)

$$\begin{aligned} i\frac{dV}{d\tilde{t}} &= \mathcal{E}_v(\vec{p}-\vec{A}(\tilde{t}))V + \vec{E}(\tilde{t})\cdot\vec{X}(\vec{p}-\vec{A}(\tilde{t}))C \\ i\frac{dC}{d\tilde{t}} &= \mathcal{E}_c(\vec{p}-\vec{A}(\tilde{t}))C + \vec{E}(\tilde{t})\cdot\vec{X}(\vec{p}-\vec{A}(\tilde{t}))V \end{aligned} \tag{8.8}$$

We can also introduce state probability amplitudes

$$\begin{aligned} v(\vec{p},\tilde{t}) &= V(\vec{p},\tilde{t})e^{i\int_{-\infty}^{\tilde{t}}\mathcal{E}_v(\vec{p}-A(t'))dt'} \\ c(\vec{p},\tilde{t}) &= C(\vec{p},\tilde{t})e^{i\int_{-\infty}^{\tilde{t}}\mathcal{E}_c(\vec{p}-A(t'))dt'} \end{aligned} \tag{8.9}$$

such that $v(\vec{p},\tilde{t})$ and $c(\vec{p},\tilde{t})$ do not change with time in the absence of the field. Finally, ODEs for $v(\vec{p},\tilde{t})$ and $c(\vec{p},\tilde{t})$ are

$$\begin{aligned} i\frac{dv}{d\tilde{t}} &= \vec{E}(\tilde{t})\cdot\vec{X}(\vec{p}-\vec{A}(\tilde{t}))ce^{-i\int_{-\infty}^{\tilde{t}}\mathcal{E}(\vec{p}-A(t'))dt'} \\ i\frac{dc}{d\tilde{t}} &= \vec{E}(\tilde{t})\cdot\vec{X}(\vec{p}-\vec{A}(\tilde{t}))ve^{i\int_{-\infty}^{\tilde{t}}\mathcal{E}(\vec{p}-A(t'))dt'} \end{aligned} \tag{8.10}$$

where $\mathcal{E}(\vec{p}) = \mathcal{E}_c(\vec{p}) - \mathcal{E}_v(\vec{p})$ is electron-hole dispersion relation. Exact solution of (8.10) can be written as unwieldy time-ordered product of unitary evolution operators. Before doing further approximations, let us write down expressions for photoionization probability and photocurrent density in terms of $c(\vec{p},\tilde{t})$ and $v(\vec{p},\tilde{t})$. In what follows we omit tilde above time argument, since $\tilde{t} = t$. Given the transition amplitude $\vec{c}(\vec{p},\tilde{t})$ we can find quantum-mechanical average of all operators of interest. Quantum-mechanical average of the operator of projection onto conduction band states

$$\hat{\rho} = \sum_k |c,\vec{k}\rangle\langle c,\vec{k}| \tag{8.11}$$

yields probability of photoionization or conduction-band electron density (it should

be noted that usage of a greek letter ρ to denote the projection operator is somewhat unconventional, projection operator is more commonly by P, however, we are planning to use P to denote electric polarization of unit volume of the dielectric further on, moreover, quantum-mechanical average of the projection operator gives conduction electron density or plasma density, customary denoted as ρ)

$$\rho(t) = \langle\hat{\rho}\rangle = \sum_{\vec{k}} |\vec{c}(\vec{k} + \vec{A}(t), t)|^2. \tag{8.12}$$

Since dispersion relation is periodic in the first Brillouin zone, summation in (8.12) can be performed either over $\vec{k}$ or over $\vec{p}$

$$\rho(t) = \sum_{\vec{p}} |\vec{c}(\vec{p}, t)|^2. \tag{8.13}$$

Polarization of the unit volume is given by average of the coordinate operator, taken with negative sign (due to the electron charge -1)

$$\vec{P}(t) = -\langle\vec{R}\rangle \tag{8.14}$$

therefore

$$\begin{aligned}\vec{P}(t) &= \sum_{\vec{k}} \vec{X}(k)\left(C(\vec{k},t)^* V(\vec{k},t) + V(\vec{k},t)^* C(\vec{k},t)\right) + \\ &+ i\sum_{\vec{k}}\left(C(\vec{k},t)^*\frac{\partial}{\partial\vec{k}}C(\vec{k},t) + V(\vec{k},t)^*\frac{\partial}{\partial\vec{k}}V(\vec{k},t)\right) = \\ &= \sum_{\vec{p}} 2\mathrm{Re}\vec{X}(\vec{p}-\vec{A}(t))c(\vec{p},t)^* v(\vec{p},t) e^{i\int_{-\infty}^{t}\mathcal{E}(\vec{p}-\vec{A}(t')dt'} + \\ &+ \sum_{\vec{p}}\left(c(\vec{p},t)^*\frac{\partial c(\vec{p},t)}{\partial\vec{p}} + v(\vec{p},t)^*\frac{\partial v(\vec{p},t)}{\partial\vec{p}}\right) \\ &+ \sum_{\vec{p}}\left(|c(\vec{p},t)|^2\int_{-\infty}^{t}\frac{\partial\mathcal{E}_c(\vec{p}-\vec{A}(t'))}{\partial\vec{p}}dt' + |v(\vec{p},t)|^2\int_{-\infty}^{t}\frac{\partial\mathcal{E}_v(\vec{p}-\vec{A}(t'))}{\partial\vec{p}}dt'\right)\end{aligned} \tag{8.15}$$

We can use relation $|v(\vec{p},t)|^2 = 1-|c(\vec{p},t)|^2$ and the fact energy-momentum relations in both conduction and valence bands are periodic, thus,

$$\sum_{p}\frac{\partial\mathcal{E}_v}{\partial\vec{p}} = 0 \tag{8.16}$$

Eq. (8.15) is then transformed into

$$\begin{aligned}\vec{P}(t) &= \sum_{\vec{p}} 2\mathrm{Re}\vec{X}(\vec{p}-\vec{A}(t))c(\vec{p},t)^* v(\vec{p},t) e^{i\int_{-\infty}^{t}\mathcal{E}(\vec{p}-\vec{A}(t')dt'} + \\ &+ \sum_{\vec{p}}\left(c(\vec{p},t)^*\frac{\partial c(\vec{p},t)}{\partial\vec{p}} + v(\vec{p},t)^*\frac{\partial v(\vec{p},t)}{\partial\vec{p}} + |c(\vec{p},t)|^2\int_{-\infty}^{t}\frac{\partial\mathcal{E}(\vec{p}-\vec{A}(t'))}{\partial\vec{p}}dt'\right)\end{aligned} \tag{8.17}$$

Photocurrents density is

$$\vec{J}(t) = \frac{d\vec{P}(t)}{dt} \tag{8.18}$$

Instead of direct differentiation of (8.17), which is already cumbersome enough,

with respect to time, we can employ the fact that averages of hermitian quantum-mechanical operators can, in principle, be observed, and thus do not depend on whether equations of motion are written in Schrödinger or Heisenberg picture. Therefore,

$$\vec{J} = -\frac{d\langle R\rangle}{dt} = -\left\langle \frac{dR}{dt} \right\rangle = i\left\langle \left[H(t), \vec{R}\right] \right\rangle = i\left\langle \left[H_0, \vec{R}\right] \right\rangle \tag{8.19}$$

Last equality in (8.19) follows from the fact that $\vec{R}$ commutes with $\vec{E}(t)\cdot\vec{R}$ term in hamiltonian $H(t)$. Therefore,

$$\vec{J}(t) = i\left\langle \sum_{\vec{k}} \mathcal{E}(\vec{k})\vec{X}(\vec{k}) \left(|c,\vec{k}\rangle\langle v,\vec{k}| - |v,\vec{k}\rangle\langle c,\vec{k}| \right) \right\rangle + i\left\langle \left[H_0, i\frac{\partial}{\partial\vec{k}}\right] \right\rangle \tag{8.20}$$

Second term in (8.20) requires careful treatment. Writing it out explicitly gives

$$\begin{aligned} \left\langle \left[H_0, i\frac{\partial}{\partial\vec{k}}\right] \right\rangle = &\sum_{\vec{k}} \langle\psi(t)| \left(\mathcal{E}_v(\vec{k})|v,\vec{k}\rangle\langle v,\vec{k}| + \mathcal{E}_c(\vec{k})|c,\vec{k}\rangle\langle c,\vec{k}| \right) i\frac{\partial}{\partial\vec{k}}|\psi(t)\rangle - \\ &- \sum_{\vec{k}} \langle\psi(t)|i\frac{\partial}{\partial\vec{k}} \left(\mathcal{E}_v(\vec{k})|v,\vec{k}\rangle\langle v,\vec{k}| + \mathcal{E}_c(\vec{k})|c,\vec{k}\rangle\langle c,\vec{k}| \right) |\psi(t)\rangle \end{aligned} \tag{8.21}$$

At a first glance, it is not clear how to take derivatives with respect to momentum of momentum eigenfunctions. However, turns out that such derivatives are not

necessary. To see that, let us use (8.4) and rewrite (8.21) as

$$\begin{aligned}
&\left\langle \left[H_0, i\frac{\partial}{\partial \vec{k}} \right] \right\rangle = \\
&\sum_{\vec{k}} \left(\mathcal{E}_v(\vec{k}) V^*(\vec{k},t) \langle v,\vec{k}| + \mathcal{E}_c(\vec{k}) C^*(\vec{k},t) \langle c,\vec{k}| \right) i\frac{\partial}{\partial \vec{k}} \left(C(\vec{k},t)|c,\vec{k}\rangle + V(\vec{k},t)|v,\vec{k}\rangle \right) - \\
&\sum_{\vec{k}} \left(C^*(\vec{k},t) \langle c,\vec{k}| + V^*(\vec{k},t) \langle v,\vec{k}'| \right) i \left(\mathcal{E}_v(\vec{k}) \frac{\partial}{\partial \vec{k}} V(\vec{k},t)|v,\vec{k}\rangle + \mathcal{E}_c(\vec{k}) \frac{\partial}{\partial \vec{k}} C(\vec{k},t)|c,\vec{k}\rangle \right) + \\
&+ \sum_{\vec{k}} |C(\vec{k},t)|^2 \frac{\partial E_c(\vec{k})}{\partial \vec{k}} + |V(\vec{k},t)|^2 \frac{\partial E_v(\vec{k})}{\partial \vec{k}}
\end{aligned} \tag{8.22}$$

Assuming $\langle v,\vec{k}|\frac{\partial}{\partial \vec{k}}|c,\vec{k}\rangle = \langle c,\vec{k}|\frac{\partial}{\partial \vec{k}}|v,\vec{k}\rangle = 0$, first two terms in (8.22) cancel out completely. Similarly to (8.15), we can use $|V(\vec{k},t)|^2 = 1 - |C(\vec{k},t)|^2$ and (8.16) and find

$$\left\langle \left[H_0, i\frac{\partial}{\partial \vec{k}} \right] \right\rangle = i \sum_{\vec{k}} |C(\vec{k},t)|^2 \frac{\partial \mathcal{E}(\vec{k})}{\partial \vec{k}} = i \sum_{\vec{p}} |c(\vec{p},t)|^2 \frac{\partial \mathcal{E}(\vec{p} - \vec{A}(t))}{\partial \vec{p}} \tag{8.23}$$

The expression for photocurrent density is then

$$\begin{aligned}
\vec{J}(t) = &\sum_{\vec{p}} 2\vec{X}(\vec{p} - \vec{A}(t)) \mathcal{E}(\vec{p} - \vec{A}(t)) \mathrm{Im} c(\vec{p},t) v^*(\vec{p},t) e^{-i\int_{-\infty}^{t} \mathcal{E}(\vec{p} - \vec{A}(t'))dt'} - \\
&- \sum_{\vec{p}} |c(\vec{p},t)|^2 \frac{\partial \mathcal{E}(\vec{p} - \vec{A}(t))}{\partial \vec{p}}
\end{aligned} \tag{8.24}$$

Both polarization and current density can be conveniently written as a sum of inter- and intraband components

$$\vec{P}(t) = \vec{P}^{(i)}(t) + \vec{P}^{(c)}(t) \tag{8.25}$$

and

$$\vec{J}(t) = \vec{J}^{(i)}(t) + \vec{J}^{(c)}(t) \tag{8.26}$$

where superscript $^{(i)}$ denotes interband, and $^{(c)}$ denotes intraband, and

$$P^{(i)}(t) = \sum_{\vec{p}} 2\mathrm{Re}\vec{X}(\vec{p} - \vec{A}(t))c(\vec{p},t)^* v(\vec{p},t) e^{i\int_{-\infty}^{t} \mathcal{E}(\vec{p}-\vec{A}(t')dt'} \tag{8.27}$$

$$P^{(c)}(t) = \sum_{\vec{p}} \left(c(\vec{p},t)^* \frac{\partial c(\vec{p},t)}{\partial \vec{p}} + v(\vec{p},t)^* \frac{\partial v(\vec{p},t)}{\partial \vec{p}} + |c(\vec{p},t)|^2 \int_{-\infty}^{t} \frac{\partial \mathcal{E}(\vec{p} - \vec{A}(t'))}{\partial \vec{p}} dt' \right) \tag{8.28}$$

$$\vec{J}^{(i)}(t) = \sum_{\vec{p}} 2\vec{X}(\vec{p} - \vec{A}(t)) \mathcal{E}(\vec{p} - \vec{A}(t)) \mathrm{Im} c(\vec{p},t) v^*(\vec{p},t) e^{-i\int_{-\infty}^{t} \mathcal{E}(\vec{p}-\vec{A}(t'))dt'} \tag{8.29}$$

$$\vec{J}^{(c)}(t) = -\sum_{\vec{p}} |c(\vec{p},t)|^2 \frac{\partial \mathcal{E}(\vec{p} - A(t))}{\partial \vec{p}} \tag{8.30}$$

Moreover, it is possible to show that

$$\vec{J}^{(i)}(t) = \frac{dP^{(i)}}{dt} \tag{8.31}$$

$$\vec{J}^{(c)}(t) = \frac{dP^{(c)}}{dt} \tag{8.32}$$

Therefore, we can account for optical response of interband transitions through polarization $P^{(i)}$, and for optical response of intraband transitions through current density $J^{(c)}(t)$, or vice versa. Expression (8.30) permits very transparent interpretation - electrons with momenta $\vec{p}$ at the time t have velocity $\frac{\partial \mathcal{E}(\vec{p}-\vec{A}(t))}{\partial \vec{p}}$. Total intraband current is a sum of contributions of velocities of electrons at all points in the momentum space, weighted with respective population, and taken with a minus sign due to negative charge of electron. The photocurrents defined by (8.24) satisfy energy conservation. Namely, the energy absorbed from the field in the unit volume at the

moment of time t due to Ohmic losses is

$$w(t) = \int_{-\infty}^{t} \vec{E}(t') \cdot \vec{J}(t') dt' = -\int_{-\infty}^{t} \left\langle \vec{E}(t') \cdot \frac{d\vec{R}(t')}{dt'} \right\rangle dt' \tag{8.33}$$

We can use Heisenberg equation of motion for $\vec{R}$

$$i\frac{d\vec{R}}{dt} = \left[H, \vec{R}\right] \tag{8.34}$$

to rewrite (8.33) as

$$w(t) = i\int_{-\infty}^{t} \left\langle \left[H(t'), \vec{E}(t') \cdot \vec{R}\right] \right\rangle dt' \tag{8.35}$$

From the form of hamiltonian (8.3) and (8.1) we get to rewrite (8.33) as

$$\begin{aligned} w(t) &= i\int_{-\infty}^{t} \left\langle \left[H_0, \vec{E}(t') \cdot \vec{R}\right] \right\rangle dt' = \\ &= i\int_{-\infty}^{t} \langle [H_0, H(t)] \rangle \, dt' = \\ &= \int_{-\infty}^{t} \frac{d\langle H_0 \rangle}{dt'} dt' = \\ &= \langle H_0 \rangle \,|_t - \langle H_0 \rangle \,|_{-\infty} \end{aligned} \tag{8.36}$$

Therefore, all the energy absorbed from the field due to Ohmic losses is absorbed by electron-hole pairs in the solid.

Let us now consider approximation of small ionization probability, standard for analysis of photoionization in solids and gases [13, 35, 36, 37, 38, 39, 94]. When $|c(\vec{p}, \tilde{t})| \ll |v(\vec{p}, \tilde{t})|$ we can set $v(\vec{p}, \tilde{t}) \approx 1$, and immediately write out solution of (8.10) as

$$c(\vec{p}, \tilde{t}) \approx -i\int_{-\infty}^{\tilde{t}} \vec{E}(t') \cdot \vec{X}(\vec{p} - \vec{A}(t')) e^{i\int_{-\infty}^{t'} \mathcal{E}(\vec{p} - \vec{A}(t''))dt''} dt' \tag{8.37}$$

As pointed out by Keldysh, transitions from valence to conduction band are

dominated by those values of $t' = t^*$, for which $M(t') = \vec{E}(t') \cdot \vec{X}(\vec{p} - \vec{A}(t'))$ has a singularity, and behavior of $M(t' \approx t^*)$ is universal and does not depend on dielectric. Thus, we can introduce

$$\vec{c}(\vec{p}, \tilde{t}) \approx -i\mathcal{N} \int_{-\infty}^{\tilde{t}} \vec{E}(t') e^{iI(\vec{p},t')} dt' \tag{8.38}$$

where $\mathcal{N}$ is the normalization factor,

$$I(\vec{p}, t) = \int_{-\infty}^{t} \mathcal{E}(\vec{p} - \vec{A}(t')) dt' \tag{8.39}$$

With $\vec{c}(\vec{p}, t)$ given by (8.38) we can further rewrite ionization probability (8.12) and photocurrents (8.30), (8.29).

$$\rho(t) = |\mathcal{N}|^2 \int_{-\infty}^{t} \int_{-\infty}^{t} \vec{E}(t_1) \cdot \vec{E}(t_2) \sum_{\vec{p}} e^{iI(\vec{p},t_2,t_1)} dt_1 dt_2 \tag{8.40}$$

$$\vec{J}^{(c)}(t) = -|\mathcal{N}|^2 \int_{-\infty}^{t} \int_{-\infty}^{t} \vec{E}(t_1) \cdot \vec{E}(t_2) \sum_{\vec{p}} e^{iI(p,t_2,t_1)} \frac{\partial \mathcal{E}(\vec{p} - \vec{A}(t))}{\partial \vec{p}} dt_1 dt_2 \tag{8.41}$$

$$\vec{J}^{(i)}(t) = -2|\mathcal{N}|^2 \int_{-\infty}^{t} \vec{E}(t_1) \sum_{\vec{p}} \mathrm{Re} e^{iI(p,t,t_1)} \mathcal{E}(\vec{p} - \vec{A}(t)) dt_1 \tag{8.42}$$

where $I(\vec{p}, t_2, t_1) = I(\vec{p}, t_2) - I(\vec{p}, t_1)$.

To summarize, in this section we developed a quantum-mechanical framework for analysis of photoionization at arbitrary short time scales, including sub-field-cycle scales. We have also shown that density of photocurrents, calculated with our framework, obeys energy conservation relation; specifically, energy of the field, that is absorbed via Ohmic losses due to photocurrents, is stored in electron-hole pairs in dielectric. Further calculations are possible if we specify certain form of dispersion relation $\mathcal{E}(\vec{p})$.

9. DERIVATION OF FORMULAS FOR PHOTOIONIZATION PROBABILITY AND PHOTOCURRENTS

9.1 Nearest-neighboor (cosine) dispersion

First, let us consider the simplest case of periodic dispersion, that follows from nearest-neighboor interaction approximation, that is,

$$\mathcal{E}(\vec{p}) = \mathcal{E}_g + \Delta - \frac{\Delta}{D}\sum_{j=1}^{D}\cos(p_j d_j) \tag{9.1}$$

where D is the number of spatial dimensions, and d_j is the lattice constant in the direction j. Let us also introduce

$$\Phi_j(t) = \frac{\Delta}{D}\int_{-\infty}^{t} e^{iA_j(t')d_j}dt' \tag{9.2}$$

and $\Phi_k(t_1,t_2) = \Phi_k(t_1) - \Phi_k(t_2)$. Due to simple form of dispersion integral $I(\vec{p},t)$ (8.39) can be evaluated exactly and gives

$$\begin{aligned} I(\vec{p},t) &= (\mathcal{E}_g+\Delta)t - \sum_{j=1}^{D}\mathrm{Re}\Phi_j(t)\cos p_j d_j - \\ &- \sum_{j=1}^{D}\mathrm{Im}\Phi_j(t)\sin p_j + const = \\ &= (\mathcal{E}_g+\Delta)t - \sum_{j=1}^{D}|\Phi_j(t)|\cos(p_j d_j - \arg\Phi_j(t)) + const \end{aligned} \tag{9.3}$$

Additive constant in expression (9.3) depends on the choice of time origin, and only affects unobservable global phase of the wavefunction. Furthermore, for crystals of

macroscopic size

$$\sum_{\vec{p}} \approx \frac{1}{(2\pi)^D} \int d^D \vec{p} \tag{9.4}$$

thus

$$\sum_{\vec{p}} e^{iI(\vec{p},t_2,t_1)} = e^{i(\mathcal{E}_g+\Delta D)(t_2-t_1)} \prod_{j=1}^{D} J_0\left(|\Phi_j(t_2,t_1)|\right) \tag{9.5}$$

and $J_0(z)$ denotes Bessel function of zeroth order. Similarly,

$$\begin{aligned}
&\sum_{\vec{p}} e^{iI(\vec{p},t,t_1)} \mathcal{E}(\vec{p} - \vec{A}(t)) = \\
&= e^{i(\mathcal{E}_g+\Delta)(t-t_1)} \prod_{j=1}^{D} J_0\left(|\Phi_j(t_2,t_1)|\right) (\mathcal{E}_g + \Delta) - \\
&- \frac{\Delta}{D} \sum_{j=1}^{D} e^{(\mathcal{E}_g+\Delta)(t-t_1)} J_1\left(|\Phi_j(t,t_1)|\right) \cos\left(d_j A_j(t) - \arg \Phi_j(t,t_1)\right) \times \\
&\times \prod_{i\neq j} J_0\left(|\Phi_i(t,t_1)|\right)
\end{aligned} \tag{9.6}$$

and

$$\begin{aligned}
&\sum_{\vec{p}} e^{iI(\vec{p},t_2,t_1)} \frac{\partial \mathcal{E}(\vec{p} - \vec{A}(t))}{\partial p_j} = \\
&= -\frac{\Delta}{D} e^{i(\mathcal{E}_g+\frac{\Delta}{D})(t_2-t_1)} J_1\left(|\Phi_i(t_2,t_1)|\right) \sin\left(d_j A_j(t) - \arg \Phi_j(t_2,t_1)\right) \times \\
&\times \prod_{i\neq j} J_0\left(|\Phi_i(t_2,t_1)|\right)
\end{aligned} \tag{9.7}$$

Expectedly, $J_1(z)$ denotes Bessel function of the first order. Finally, we write down the expressions for photoionization probability

$$\rho(t) = |\mathcal{N}|^2 \int_{-\infty}^{t} \int_{-\infty}^{t} dt_1 dt_2 \vec{E}(t_1) \cdot \vec{E}(t_2) e^{i(\mathcal{E}_g+\Delta)(t_2-t_1)} \prod_{j=1}^{D} J_0\left(|\Phi_j(t_2,t_1)|\right) \tag{9.8}$$

interband photocurrent

$$J_j^{(i)}(t) = 2|\mathcal{N}|^2 \int_{-\infty}^{t} dt_1 E_j(t_1) \Bigg[\cos(\mathcal{E}_g + \Delta)(t - t_1) \prod_{j=1}^{D} J_0\left(|\Phi_j(t, t_1)|\right) (\mathcal{E}_g + \Delta) -$$
$$- \frac{\Delta}{D} \sin(\mathcal{E}_g + \Delta)(t - t_1) \times$$
$$\times \sum_{j=1}^{D} J_1\left(|\Phi_j(t, t_1)|\right) \cos\left(d_j A_j(t) - \arg \Phi_j(t, t_1)\right) \prod_{k \neq j} J_0\left(|\Phi_k(t, t_1)|\right) \Bigg] \tag{9.9}$$

and intraband photocurrent

$$J_j^{(c)}(t) = |\mathcal{N}|^2 \int_{-\infty}^{t} \int_{-\infty}^{t} dt_1 dt_2 \vec{E}(t_1) \cdot \vec{E}(t_2) e^{i(\mathcal{E}_g + \Delta)(t_2 - t_1)} \times$$
$$\frac{\Delta}{D} J_1\left(|\Phi_j(t_2, t_1)|\right) \sin\left(d_j A_j(t) - \arg \Phi_j(t_2, t_1)\right) \prod_{k \neq j} J_0\left(|\Phi_k(t_2, t_1)|\right) \tag{9.10}$$

Before we proceed to more general case, let us touch bases with existing theories. Fig. 9.1(a) shows results of calculations of CB population in the wake of 20-cycle long gaussian pulse as a function of peak pulse intensity via Keldysh theory [13] and using our field-cycle-resolved photoionization theory (FCRPI). Material parameters are assumed to mimic fused silica, namely, band gap $\mathcal{E}_g = 9$ eV, kinetic energy of electron-hole pair at the edge of Brilloin zone $\Delta = 5.5$ eV, and electron-hole mass $m* \approx m_e$, where m_e is mass of the free electron [99]. Although fused silica is an amorphous material, it is customary to apply crystal-based photoionization theories to fused silica; in fact, the majority of experimental data on photoionization and laser-induced damage is available for fused silica, [100, 101, 4, 102, 103].

In the low-intensity regions predictions of both theories coincide remarkably well. In the high-intensity regions electrons "start to feel" the difference between the hyperbolic dispersion relation, assumed in Keldysh theory, and the cosine dispersion

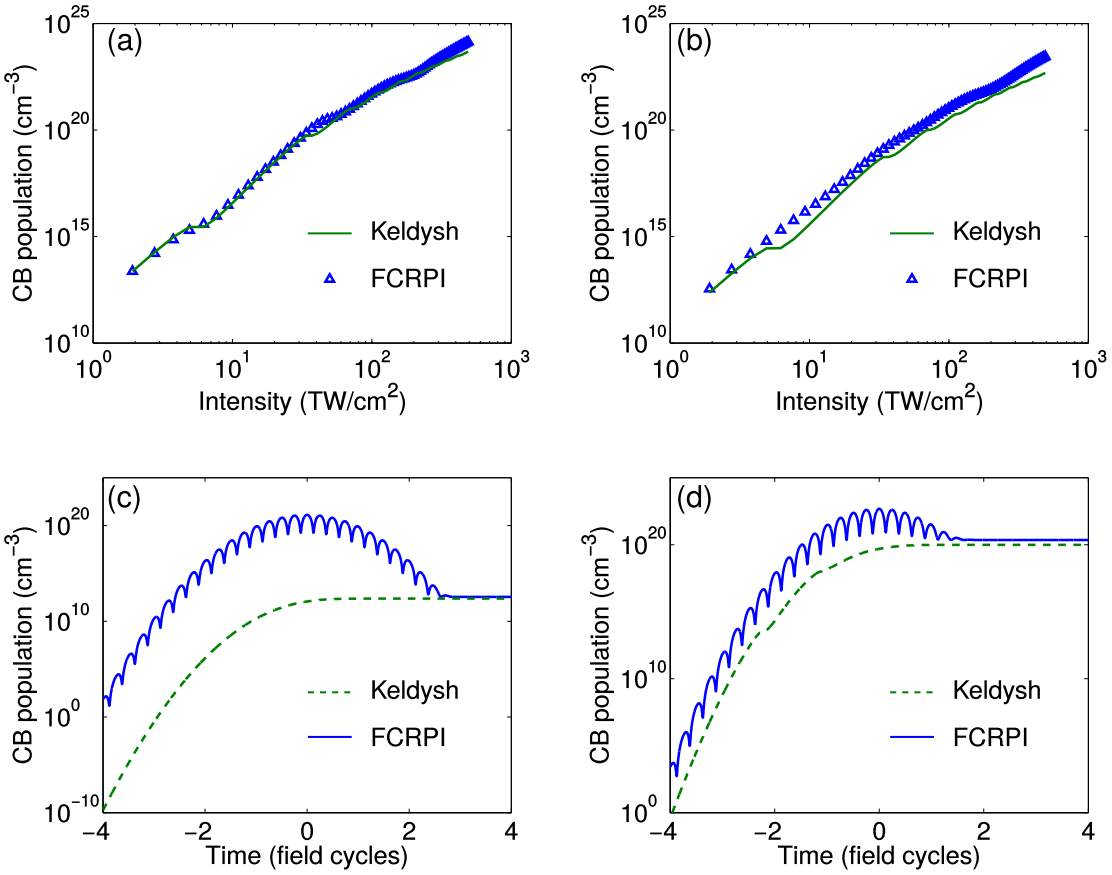

Figure 9.1 (a),(b) Ionization probability in the wake of the pulse, calculated using Keldysh theory (solid blue line), and our field-cycle-resolved photoionization theory (blue triangles). FWHM pulse duration is (a) 20 cycles , and (b) 2 cycles. (c),(d) Photoionization probability as a function of time, calculated using Keldysh theory (dashed green line), and field-cycle-resolved photoionization theory (solid blue line). FWHM pulse duration is 2 cycles. Peak pulse intensity is (c) 2 TW/cm^2 and (d) 70 TW/cm^2.

relation (9.1). When pulse durations gets smaller, Keldysh theory simply predicts linear decrease of CB population with pulse duration for a given peak intensity. FCRPI takes into account that with decreasing pulse duration it spectrum broadens. Most conspicuous difference between long- and short pulse dependencies of ionization probability on intensity is absence of Franz-Keldysh steps [104, 105]. These steps in the ionization probability as a function of intensity are due to the modification of the band gap by the applied field. More specifically, the steps occur when effective, field-modified band gap matches energy of integer number of field photons. At small pulse durations energy of a photon is not well-defined due to uncertainty principle, hence, there is no pronounced steps in the ionization probability as a function of intensity [Fig. 9.1(b)], in the contrast to predictions of keldysh formula that is based on assumtion of continuous-wave radiation.

While ionization probability in the wake of the pulse, predicted using our field-cycle-resolved photoionization (FCRPI) theory, coincides closely with one predicted by Keldysh formula, ionization probability within the pulse differs substantially [Fig. 9.1(c),(d)]. FCRPI predicts strongly oscillatory behaviour of ionization probability (defined, as we recall from Eqs. (8.11)–(8.13), as probability of electron to occupy one of the conduction band states at a moment of time t), whereas Keldysh theory predicts monotonic growth of ionization probability as a function of time. The difference stems again from the fact that Keldysh theory is intrinsically time-averaged, and disregards virtual electrons that are returning back to the valence band. At sub-field-cycle time scales there is no difference between CB electrons that are going back to valence band, and CB electrons that are in conduction band "to stay"; virtual electrons must be included for correct treatment of sub-cycle photoionization and calculation of photocurrents at sub-field-cycle time scale.

Let us now compare the photocurrents calculated via FCRPI with photocurrents

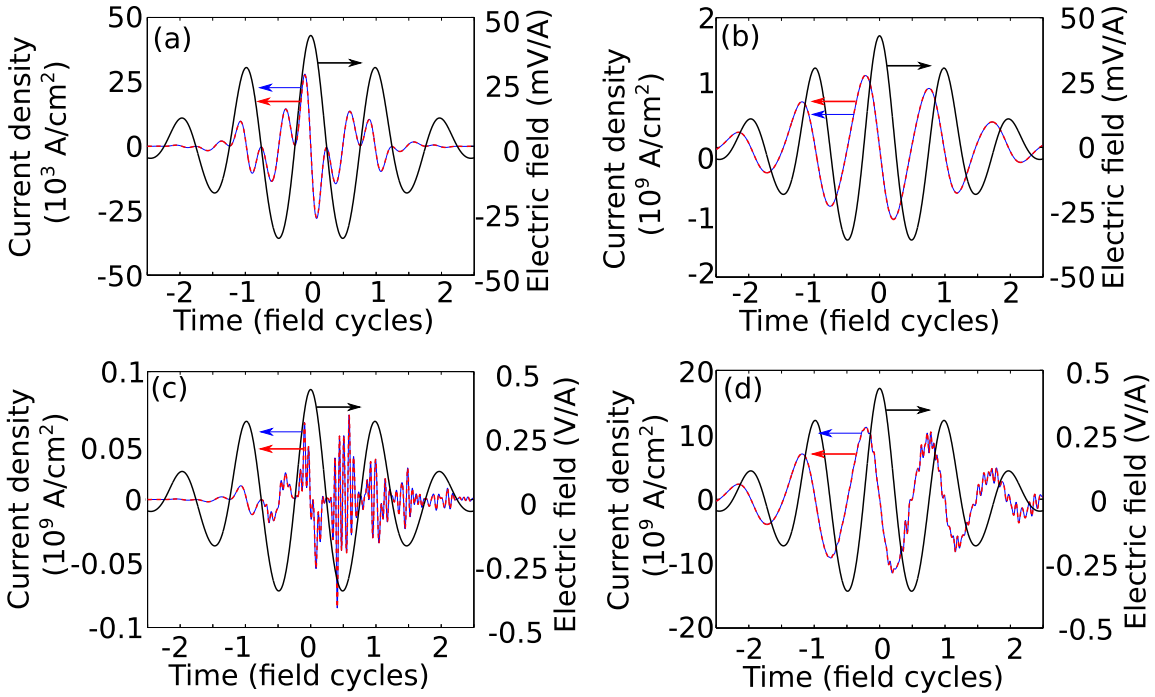

Figure 9.2 Comparison of density of (a),(c) intraband current and (b),(d) interband current calculations in 1-D semiconductor by Schrödinger equation (thin blue line, left axis) and by our photoionization theory (dashed red line, left axis). Electric field of the pulse is shown by solid thick black line, right axis. Medium parameters mimic diamond, pulse duration 2 cycles FWHM, central pulse wavelength 1.6 μm, pulse intensity is (b),(c) 0.02 TW/cm^2 and (d),(e) 2.2 TW/cm^2.

calculated via Schrödinger equation in 1-D dielectric. Fig. 9.2 shows intraband current density [Fig. 9.2(a),(c)] and interband current density [Fig. 9.2(b),(d)] in the regimes of low and high intensity. Transition matrix element $\vec{X}(\vec{k})$ is adjusted to satisfy condition $|c(\vec{p},\tilde{t})| \ll |v(\vec{p},\tilde{t})|$. We see that both in low and high-intensity regimes FCRPI accurately reproduces results of Schrödinger equation.

9.2 Arbitrary separable dispersion

Deriving expressions (9.5) – (9.7) we notice that integrations are easy to perform because integrands factorize as functions of momenta components along different Cartesian axes, which is, in turn, due to the fact that dispersion relation (9.1) is a sum of terms each of which contains only one Cartesian component of momentum. Let us now assume dispersion relation can be written as

$$\mathcal{E}(\vec{p}) = \mathcal{E}_g + \Delta - \sum_{j=1}^{D} \sum_{n} \Delta_j^{(n)} \cos(np_j d_j + \phi_j^{(n)}) \tag{9.11}$$

where $\mathcal{E}_g$ is bandgap and $\Delta = \sum_{j=1}^{D} \sum_n \Delta_j^{(n)} \cos \phi_j^{(n)}$. For example, arbitrary periodic 1-D dispersion can be written in this form (although, technically, the number of terms in the sum in (9.11) might be infinite). Then, similarly to (9.3), we evaluate expression (8.39) for $I(\vec{p}, t)$ as follows

$$\begin{aligned} I(\vec{p}, t) &= (\mathcal{E}_g + \Delta)t - \sum_{n} \sum_{j=1}^{D} \mathrm{Re}\Phi_j^{(n)}(t) \cos np_j d_j - \\ &- \sum_{j=1}^{D} \mathrm{Im}\Phi_j^{(n)}(t) \sin np_j + const = \\ &= (\mathcal{E}_g + \Delta)t - \sum_{n} \sum_{j=1}^{D} |\Phi_j^{(n)}(t)| \cos(np_j d_j - \arg \Phi_j^{(n)}(t)) + const \end{aligned} \tag{9.12}$$

where

$$\Phi_j^{(n)}(t) = \Delta_j^{(n)} \int_{-\infty}^{t} e^{ind_j A_j(t') + \phi_j^{(n)}} dt' \tag{9.13}$$

Calculation of sums like $\sum_{\vec{p}} e^{iI(\vec{p},t_2,t_1)}$ is a bit more involved than in the case of nearest-neighbour (cosine) dispersion. Specifically,

$$\begin{aligned}
&\sum_{\vec{p}} e^{iI(\vec{p},t_2,t_1)} = e^{i(\mathcal{E}_g+\Delta)(t_2-t_1)} \sum_{\vec{p}} \prod_{j=1}^{D} e^{i\sum_n |\Phi_j^{(n)}(t_2,t_1)| \cos(nd_jp_j - \arg \Phi_j^{(n)}(t_2,t_1))} = \\
&= e^{i(\mathcal{E}_g+\Delta)(t_2-t_1)} \frac{1}{(2\pi)^D} \int_{BZ} d^D\vec{p} \prod_{j=1}^{D} \prod_{n} e^{i|\Phi_j^{(n)}(t_2,t_1)| \cos(nd_jp_j - \arg \Phi_j^{(n)}(t_2,t_1))} = \\
&= e^{i(\mathcal{E}_g+\Delta)(t_2-t_1)} \prod_{j=1}^{D} \frac{1}{2\pi} \int_{-\pi/d_j}^{\pi/d_j} dp_j \prod_{n} \sum_{m_n=-\infty}^{\infty} J_{m_n}\left(|\Phi_j^{(n)}(t_2,t_1)|\right) \times \\
&\times e^{im_n(nd_jp_j - \arg \Phi_j^{(n)}(t_2,t_1)) + im_n\pi/2}
\end{aligned} \tag{9.14}$$

In the last expression in (9.14) we can exchange summation and product and operation, keeping in mind that summation is performed over all possible N-tuples of integer values $\{m_1, \dots m_N\}$, where N is maximum number of harmonic in the dispersion relation

$$\begin{aligned}
&\sum_{\vec{p}} e^{iI(\vec{p},t_2,t_1)} = e^{i(\mathcal{E}_g+\Delta)(t_2-t_1)} \prod_{j=1}^{D} \sum_{\{m_1,\dots m_N\}} \prod_{n=1}^{N} J_{m_n}\left(|\Phi_j^{(n)}(t_2,t_1)|\right) \times \\
&\times \frac{1}{2\pi} \int_{-\pi/d_j}^{\pi/d_j} dp_j e^{im_n(nd_jp_j - \arg \Phi_j^{(n)}(t_2,t_1))}
\end{aligned} \tag{9.15}$$

Integral over dp_j in (9.15) is non-zero only for those tuples $\{m_1, m_2, \dots m_N\}$, for which

$$\sum_{n=1}^{N} m_n n = 0 \tag{9.16}$$

Strictly speaking, there is infinite number of tuples satisfying (9.16), however, the largest contribution comes term where all $m_n = 0$. Therefore, N is maximum number

of harmonic in the dispersion relation

$$\sum_{\vec{p}} e^{iI(\vec{p},t_2,t_1)} \approx e^{i(\mathcal{E}_g+\Delta)(t_2-t_1)} \prod_{j=1}^{D} \prod_{n} J_0\left(|\Phi_j^{(n)}(t_2,t_1)|\right) \tag{9.17}$$

Mathematically, equality in (9.17) is exact when there is only one harmonic term in dispersion relation (regardless whether it is first, nearest-neighbor term or a higher-order term). Similarly,

$$\begin{aligned}
&\sum_{\vec{p}} e^{iI(\vec{p},t,t_1)} \mathcal{E}(\vec{p} - \vec{A}(t)) = \\
&= e^{i(\mathcal{E}_g+\Delta)(t-t_1)} \sum_{\vec{p}} \prod_{j=1}^{D} e^{i\sum_n |\Phi_j^{(n)}(t_2,t_1)| \cos(nd_j p_j - \arg \Phi_j^{(n)}(t_2,t_1))} \times \\
&\times \left[(\mathcal{E}_g + \Delta) - \sum_{i=1}^{D} \sum_{k} \Delta_i^{(k)} \cos\left(kd_i(p_i - A_i(t)) + \phi_k\right) \right]
\end{aligned} \tag{9.18}$$

First term in square brackets in (9.18) is just $(\mathcal{E}_g + \Delta) \sum_{\vec{p}} e^{iI(\vec{p},t,t_1)}$ and can be evaluated using (9.15). To calculate the second term, let us consider the following expression

$$\begin{aligned}
&\sum_{\vec{p}} \sum_{k} e^{i\sum_n |\Phi_j^{(n)}(t_2,t_1)| \cos(nd_j p_j - \arg \Phi_j^{(n)}(t_2,t_1))} \cos(kd_i(p_i - A_i(t) + \phi_k) = \\
&= \frac{1}{2} \sum_{\vec{p}} \sum_{k} e^{i\sum_n |\Phi_j^{(n)}(t_2,t_1)| \cos(nd_j p_j - \arg \Phi_j^{(n)}(t_2,t_1))} \left(e^{i(kd_i(p_i - A_i(t) + \phi_k)} + c.c. \right) = \\
&= \frac{1}{2} \sum_{\vec{p}} \sum_{k} \prod_{n} \sum_{m_n} J_{m_n}\left(|\Phi_j^{(n)}(t_2,t_1)|\right) e^{im_n \pi/2} \times \\
&\quad \times e^{im_n(nd_j p_j - \arg \Phi_j^{(n)}(t_2,t_1))} \left(e^{i(kd_i(p_i - A_i(t) + \phi_k)} + c.c. \right)
\end{aligned} \tag{9.19}$$

Expression (9.19) can be further expanded as

$$\begin{aligned}
&\sum_{\vec{p}}\sum_{k} e^{i\sum_n |\Phi_j^{(n)}(t_2,t_1)|\cos(nd_jp_j - \arg\Phi_j^{(n)}(t_2,t_1))}\cos(kd_i(p_i - A_i(t) + \phi_k) = \\
&= \frac{1}{2}\sum_{\vec{p}}\sum_{k}\sum_{\{m_1,\ldots m_N\}}\prod_n J_{m_n}\left(|\Phi_j^{(n)}(t_2,t_1)|\right)\times \\
&\times\Bigg[e^{i(\sum_n m_n n + k)d_jp_j - i\sum_n m_n \arg\Phi_j^{(n)}(t_2,t_1) - ikd_iA_i(t) + i\phi_k + i\sum_n m_n\pi/2} + \\
&\quad + e^{i(\sum_n m_n n - k)d_jp_j - i\sum_n m_n \arg\Phi_j^{(n)}(t_2,t_1) + ikd_iA_i(t) - i\phi_k + i\sum_n m_n\pi/2}\Bigg]
\end{aligned} \tag{9.20}$$

The sum over momenta $\vec{p}$ in (9.20) vanishes unless

$$\sum_n m_n n = -k \tag{9.21}$$

for first exponent in parenthesis in (9.20) and

$$\sum_n m_n n = k \tag{9.22}$$

for second exponent. Like in (9.15), we keep only the largest term, given by $m_n = 0 \quad n \neq k$ and $m_k = \pm 1$.

Then

$$\begin{aligned}
&\sum_{\vec{p}}\sum_{k} e^{i\sum_n |\Phi_j^{(n)}(t_2,t_1)|\cos(nd_jp_j - \arg\Phi_j^{(n)}(t_2,t_1))}\cos(kd_i(p_i - A_i(t) + \phi_k) \approx \\
&\quad \approx \frac{1}{2}\sum_{k}\prod_{n\neq k} J_0\left(|\Phi_j^{(n)}(t_2,t_1)|\right)\times \\
&\times\Bigg[-iJ_{-1}\left(|\Phi_j^{(k)}(t_2,t_1)|\right)e^{i\arg\Phi_j^{(k)}(t_2,t_1) - ikd_iA_i(t) + i\phi_k} + \\
&\quad + iJ_1\left(|\Phi_j^{(k)}(t_2,t_1)|\right)e^{-i\arg\Phi_j^{(k)}(t_2,t_1) + ikd_iA_i(t) - i\phi_k}\Bigg]
\end{aligned} \tag{9.23}$$

Finally,

$$\sum_{\vec{p}}\sum_{k} e^{i\sum_n |\Phi_j^{(n)}(t_2,t_1)|\cos(nd_jp_j-\arg\Phi_j^{(n)}(t_2,t_1))}\cos(kd_i(p_i-A_i(t)+\phi_k)\approx$$
$$\approx i\sum_k J_1\left(|\Phi_j^{(k)}(t_2,t_1)|\right)\cos\left(\arg\Phi_j^{(k)}(t_2,t_1)-kd_iA_i(t)+i\phi_k\right)\prod_{n\neq k}J_0\left(|\Phi_j^{(n)}(t_2,t_1)|\right) \tag{9.24}$$

Therefore,

$$\begin{aligned}
&\sum_{\vec{p}} e^{iI(\vec{p},t,t_1)}\mathcal{E}(\vec{p}-\vec{A}(t))\approx\\
&\approx ie^{i(\mathcal{E}_g+\Delta)(t-t_1)}\Bigg[\prod_n\prod_{j=1}^{D}J_0\left(|\Phi_j^{(n)}(t_2,t_1)|\right)(\mathcal{E}_g+\Delta)-\\
&-\sum_k\sum_{j=1}\Delta_j^{(k)}J_1\left(|\Phi_j^{(k)}(t,t_1)|\right)\cos\left(kd_jA_j(t)-\arg\Phi_j^{(k)}(t,t_1)-\phi_k\right)\times\\
&\times\prod_{l\neq j\cup n\neq k}J_0\left(|\Phi_l^{(n)}(t,t_1)|\right)\Bigg]
\end{aligned} \tag{9.25}$$

and

$$\begin{aligned}
&\sum_{\vec{p}} e^{iI(\vec{p},t_2,t_1)}\frac{\partial\mathcal{E}(\vec{p}-\vec{A}(t))}{\partial p_j}\approx\\
&=e^{i(\mathcal{E}_g+\Delta)(t_2-t_1)}\sum_k\Delta_j^{(k)}J_1\left(|\Phi_j^{(k)}(t_2,t_1)|\right)\times\\
&\times\sin\left(kd_jA_j(t)-\arg\Phi_j(t,t_1)-\phi_k\right)\prod_{l\neq j\cup n\neq k}J_0\left(|\Phi_l^{(n)}(t_2,t_1)|\right)
\end{aligned} \tag{9.26}$$

Thus, the final expressions for photoionization probability is similar to (9.8)

$$\rho(t) = |\mathcal{N}|^2 \int_{-\infty}^{t} \int_{-\infty}^{t} dt_1 dt_2 \vec{E}(t_1) \cdot \vec{E}(t_2) e^{i(\mathcal{E}_g+\Delta)(t_2-t_1)} \prod_n \prod_{j=1}^{D} J_0 \left(|\Phi_j^{(n)}(t_2, t_1)| \right), \tag{9.27}$$

and expressions for photocurrent densities as functions of time are also similar to (9.9) –(9.10)

$$\begin{aligned} &\vec{J}^{(i)}(t) = |\mathcal{N}|^2 \int_{-\infty}^{t} dt_1 \vec{E}(t_1) \times \\ &\Bigg[\cos(\mathcal{E}_g + \Delta)(t - t_1) \prod_n \prod_{j=1}^{D} J_0 \left(|\Phi_j^{(n)}(t_2, t_1)| \right) (\mathcal{E}_g + \Delta) - \\ &- \sum_k \Delta_j^{(k)} \sum_{j=1}^{D} J_1 \left(|\Phi_j^{(n)}(t, t_1)| \right) \cos \left(k d_j A_j(t) - \arg \Phi_j^{(k)}(t, t_1) - \phi_k \right) \times \\ &\times \prod_{l \neq j \cup n \neq k} J_0 \left(|\Phi_l^{(k)}(t, t_1)| \right) \sin(\mathcal{E}_g + \Delta)(t - t_1) \Bigg] \end{aligned} \tag{9.28}$$

Intraband current density is given by

$$\begin{aligned} &J_j^{(c)}(t) = |\mathcal{N}|^2 \int_{-\infty}^{t} \int_{-\infty}^{t} dt_1 dt_2 \vec{E}(t_1) \cdot \vec{E}(t_2) e^{i(\mathcal{E}_g+\Delta)(t_2-t_1)} \times \\ &\sum_k \Delta_j^{(k)} J_1 \left(|\Phi_j^{(k)}(t_2, t_1)| \right) \sin \left(k d_j A_j(t) - \arg \Phi_j^{(k)}(t_2, t_1) - \phi_k \right) \times \\ &\times \prod_{l \neq j \cup n \neq k} J_0 \left(|\Phi_l^{(n)}(t_2, t_1)| \right) \end{aligned} \tag{9.29}$$

Let us now compare the results of our theory, applied to dispersion with higher-order harmonics, with direct numerical solution of Schrödinger equation (more accurately, against solution of the equations (8.5)) in one dimension. We take parameters to mimc experimental conditions described in [106], namely, ZnO crystal with band gap 3.2 eV, irradiated with ultrashort pulses with central wavelength 3.4 μm. Amplitudes of first and thrid harmonic in the dispersion relation are $\Delta^{(1)} = 0.38\mathcal{E}_g$ and

$\Delta^{(3)} = 0.02\mathcal{E}_g$, and phases of these harmonics are $\phi^{(1)} = \phi^{(3)} = 0$.

Firstly, we compare ionization probability $\rho(t)$. Fig. 9.3(a) shows ionization probability in the wake of the pulse as a function of peak pulse intensity. When we take into account only first term in dispersion, results of calculation via Schrödinger equation and via field-cycle-resolved photoionization theory (FCRPI) coincide [thin and think solid blue lines in Fig. 9.3(a)]. When we add third harmonic to the electron-hole dispersion relation, certain discrepancy between Schrödinger equation and FCRPI appears (due to random phase approximation, underlying Eq. (9.15)). At the same time, overall shape of the wake ionization probability as a function of intensity, and ionization probability as a function of time [Fig. 9.3(b)–(c)] qualitatively is well reproduced by FCRPI. Interestingly, the discrepancy is largest at intermediate level of intensities [Fig. 9.3(c)], at low [Fig. 9.3(b)] and high [Fig. 9.3(d)] levels of intensities results of Schrödinger equation are accurately reproduced by FCRPI.

Interband and intraband current densities exhibit similar trend. On the qualitative level, temporal profiles of currents, calculated via Schrödinger equation, are well reproduced by FCRPI. Discrepancy is largest at the intermediate level of intensities becomes smaller at low and high intensities [Figs. 9.4–9.6].

To summarize, in this section we have applied framework developed in the previous section to calculate photoionization probability and density of photocurrents (both interband and intraband) for electric field of arbitrary temporal shape in the dielectric with cosine–type (nearest-neighbor) electron-hole dispersion, and derived approximate expressions for dielectric with arbitrary separable dispersion.

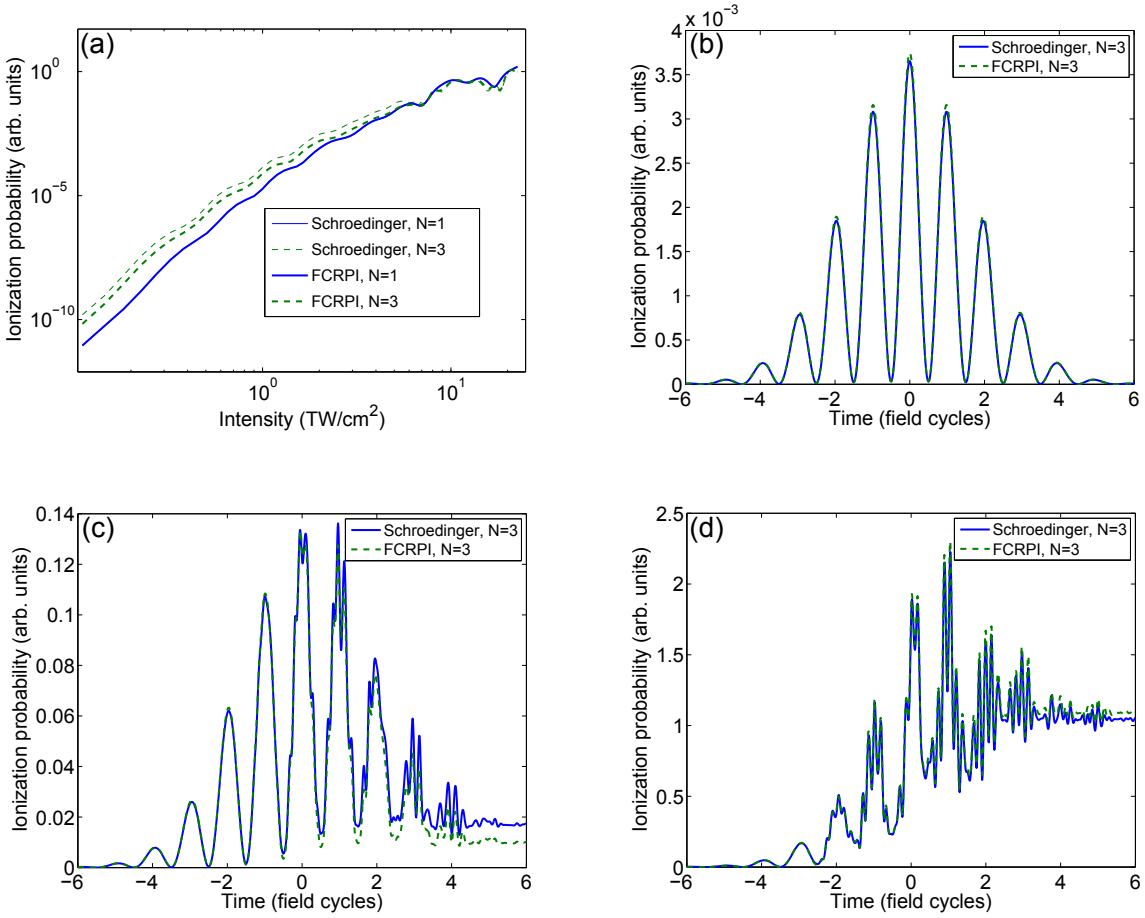

Figure 9.3 (a) Ionization probability in the wake of the pulse as a function of peak pulse intensity, calculated via Schrödinger equation with only first harmonic in the dispersion relation (thin solid blue line), via Schrödinger equation with 3 harmonics in the dispersion relation (thin dashed green line), via field-cycle-resolved photoionization theory with only first harmonic in the dispersion relation (thick solid blue line), and via field-cycle-resolved photoionization theory (thick dashed green line). (b)–(d) Ionization probability as a function of time, calculated via Schrödinger equation (solid blue line) and via FCRPI (dashed green line) with three harmonics in the dispersion relation. Peak pulse intensity is 0.1 TW/cm^2 (b), 3.6 TW/cm^2 (c), 22 TW/cm^2 (d). Pulse duration 2 cycles FWHM, central pulse wavelength 3.4 μm, dielectric band gap 3.2 eV.

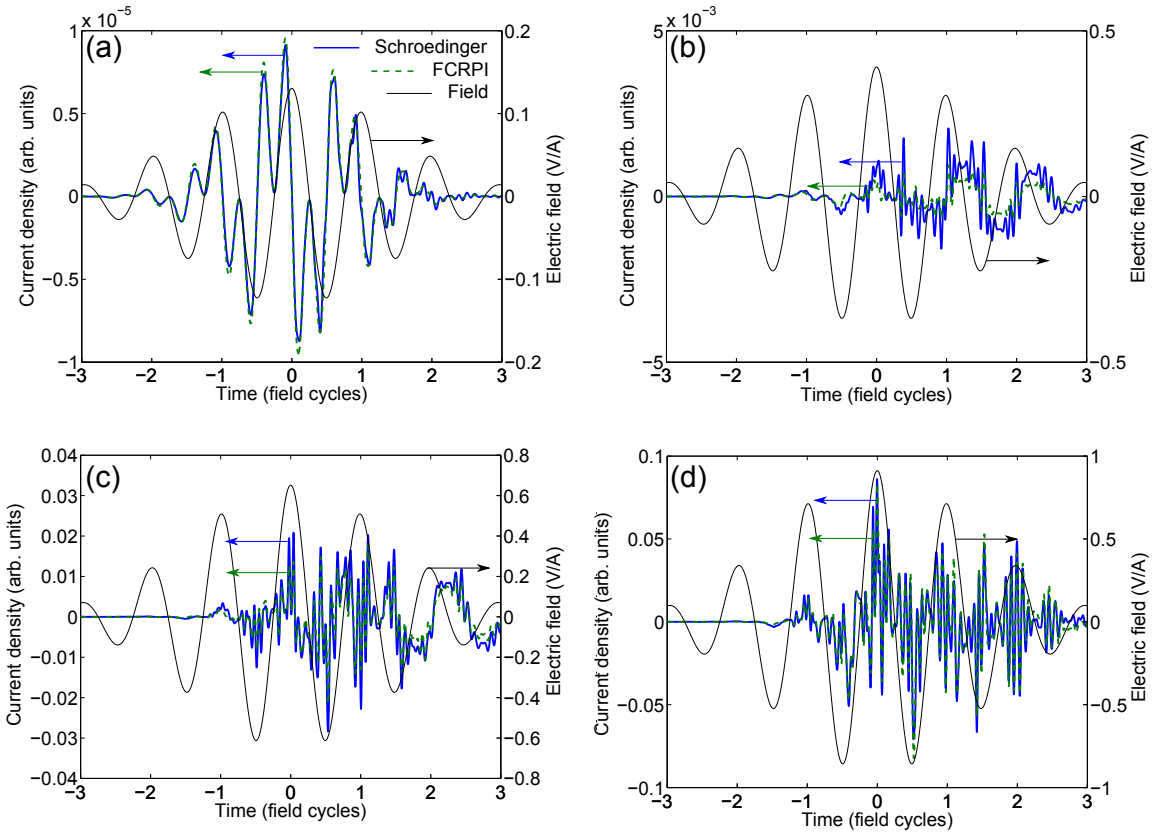

Figure 9.4 Intraband current density as a function of time, calculated via Schrödinger equation (solid blue line, left axis), and via field-cycle-resolved photoionization theory (dashed green line, left axis). Thin solid black line (right axis) shows temporal profile of electric field. Peak pulse intensity is 0.2 TW/cm^2 (a), 2 TW/cm^2 (b), 5.6 TW/cm^2 (c), and 11 TW/cm^2 (d). Pulse duration 2 cycles FWHM, central pulse wavelength 3.4 μm, dielectric band gap 3.2 eV.

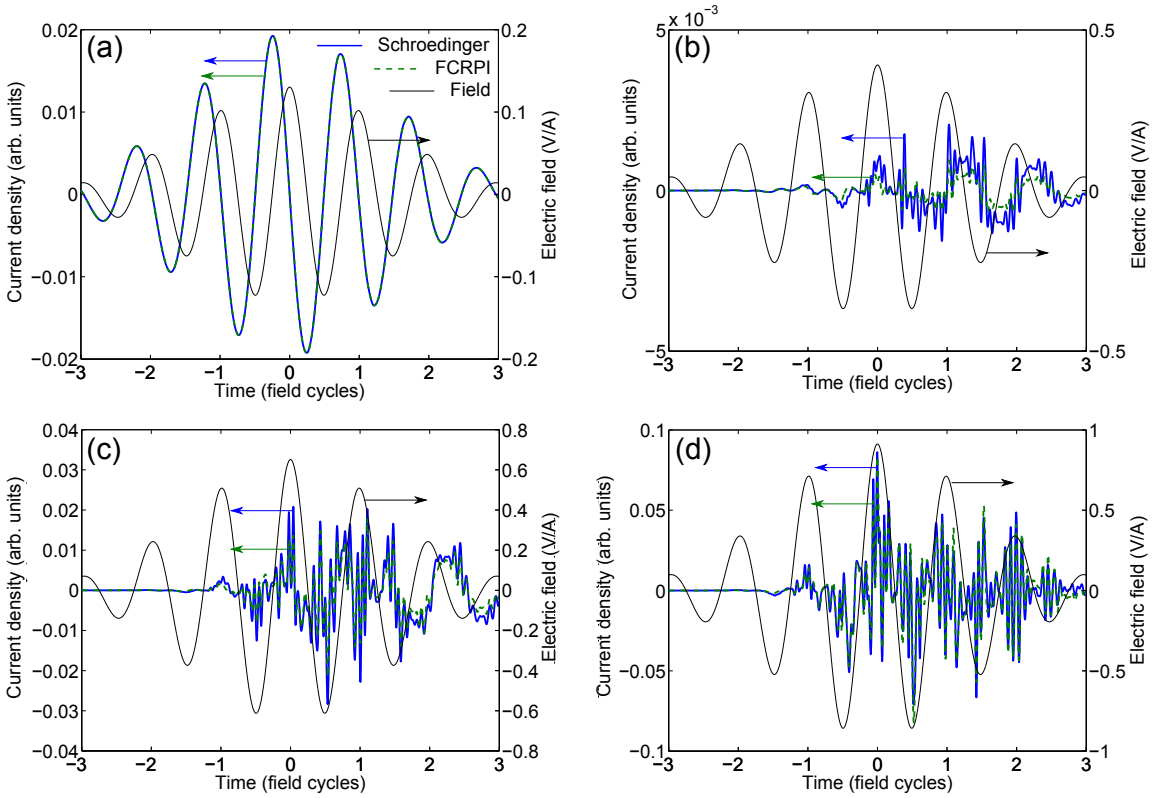

Figure 9.5 Interband current density as a function of time, calculated via Schrödinger equation (solid blue line, left axis), and via field-cycle-resolved photoionization theory (dashed green line, left axis). Thin solid black line (right axis) shows temporal profile of electric field. Peak pulse intensity is 0.2 TW/cm^2 (a), 2 TW/cm^2 (b), 5.6 TW/cm^2 (c), and 11 TW/cm^2 (d). Pulse duration 2 cycles FWHM, central pulse wavelength 3.4 μm, dielectric band gap 3.2 eV.

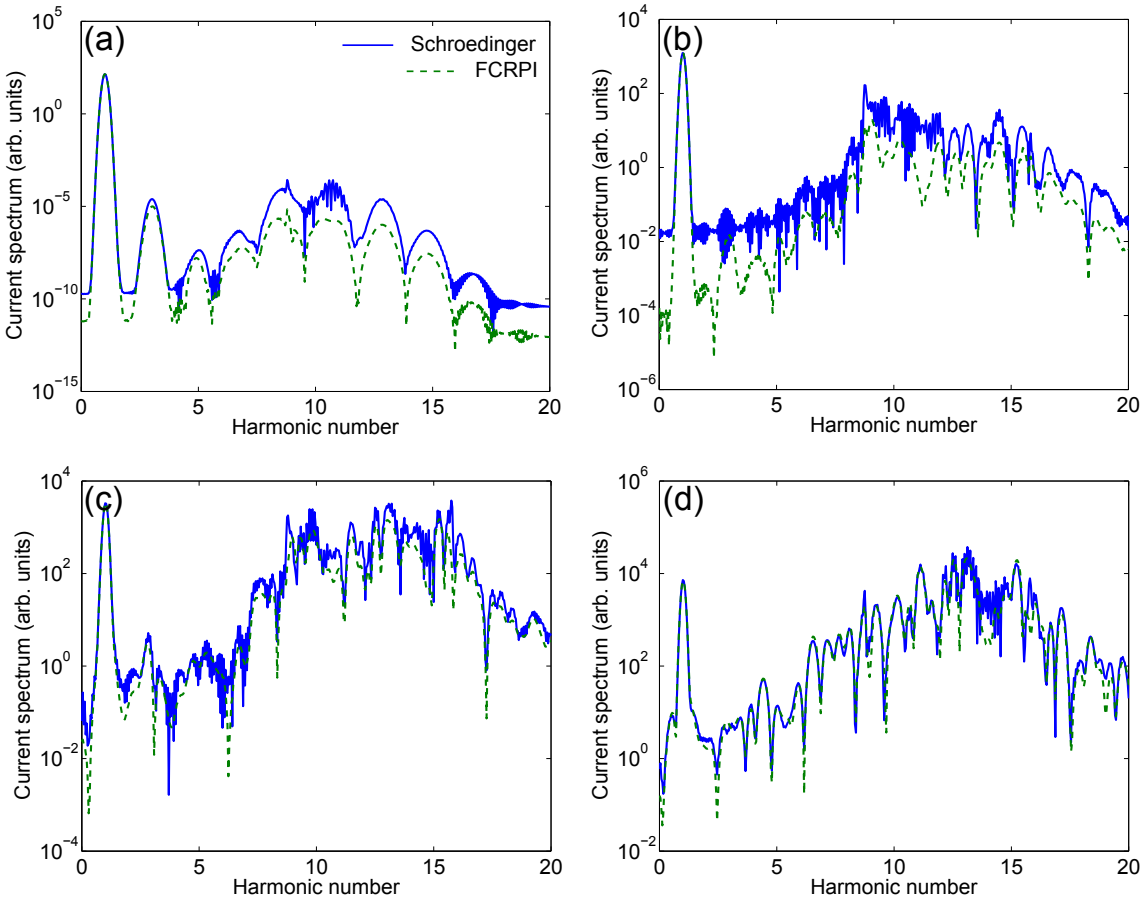

Figure 9.6 Spectrum of total current density as a function of time, calculated via Schrödinger equation (solid blue line, left axis), and via field-cycle-resolved photoionization theory (dashed green line, left axis). Peak pulse intensity is 0.2 TW/cm^2 (a), 2 TW/cm^2 (b), 5.6 TW/cm^2 (c), and 11 TW/cm^2 (d). Pulse duration 2 cycles FWHM, central pulse wavelength 3.4 μm, dielectric band gap 3.2 eV.

10. AVALANCHE IONIZATION

Fully quantum-mechanical description of avalanche ionization requires treatment through second quantization, because avalanche ionization is intrinsically multi-body effect. In this section, we will instead use *ad hoc* approach, and include avalanche corrections to the formalism of sections 8 and 9 by analogy with solutions of simple kinteic equation for plasma density in the presense of photoionization and avalanche ionization.

First, let us briefly consider equation (2.6) without recombination term

$$\frac{\partial \rho}{\partial t} = W\left(|A|^2\right)\rho_{at} + \frac{\sigma\left(\omega_0\right)}{U_i + U_p}\rho|A|^2 \tag{10.1}$$

and, more generally, equations of the form

$$\frac{\partial \rho(t)}{\partial t} = W\left(|A(t)|^2\right)\rho_{at} + \alpha(A(t))\rho(t) \tag{10.2}$$

where $\alpha(A)$ is avalanche ionization cross-section. It is easy to see that (10.1) permits solution in the following form

$$\rho(t) = \int_{-\infty}^{t} \rho_{at} W(|A(t')|^2) e^{\int_{t'}^{t} \alpha(A(t''))dt''} dt' \tag{10.3}$$

We are going to include avalanche growth factor, similar to $e^{\int_{t'}^{t} \alpha(A(t'')dt''}$ in (10.3), into the avalanche cross-section.

Then we can introduce

$$I_\alpha(t, t_1) = \int_{t_1}^{t} \alpha(t')dt' \tag{10.4}$$

and rewrite $\vec{c}(\vec{p}, \tilde{t})$ (8.38) as

$$\vec{c}(\vec{p},\tilde{t}) \approx -i\mathcal{N}\int_{-\infty}^{\tilde{t}} \vec{E}(t')e^{iI(\vec{p},t')+I_\alpha(\tilde{t},t')}dt' \tag{10.5}$$

Note that dynamics of $\vec{c}(\vec{p},\tilde{t})$ given by (10.5) is no longer hamiltonian, hence, we cannot rely on (8.36) to prove energy conservation. In fact, as we will see below, the interband current will have extra term. Let us write energy stored in electron-hole pairs at moment t as

$$w(t) = \sum_{\vec{p}} |\vec{c}(\vec{p},t)|^2 \mathcal{E}(\vec{p} - A(t)) \tag{10.6}$$

On the other hand,

$$w(t) = \int_{-\infty}^{t} \vec{E}(t') \cdot \vec{J}(t')dt' \tag{10.7}$$

Therefore,

$$\begin{aligned} \vec{J}(t) \cdot \vec{E}(t) &= \frac{d}{dt}\sum_{\vec{p}} |\vec{c}(\vec{p},t)|^2 \mathcal{E}(\vec{p} - A(t)) \\ &= \sum_{\vec{p}} \frac{\partial |\vec{c}(\vec{p},t)|^2}{\partial t}\mathcal{E}(\vec{p} - A(t)) - \sum_{\vec{p}} |\vec{c}(\vec{p},t)|^2 \frac{\partial \mathcal{E}(\vec{p} - A(t))}{\partial \vec{p}} \cdot \vec{E}(t) \end{aligned} \tag{10.8}$$

We recognize that second term in (10.8) is $\vec{J}^{(c)}(t) \cdot \vec{E}(t)$, that is, energy absorbed by intraband current $\vec{J}^{(c)}(t)$ (8.30). Naturally, we then assign first term as energy absorbed by interband current,

$$\vec{J}^{(t)}(t) \cdot \vec{E}(t) = \sum_{\vec{p}} \frac{\partial |\vec{c}(\vec{p},t)|^2}{\partial t}\mathcal{E}(\vec{p} - A(t)) \tag{10.9}$$

With $\vec{c}(\vec{p},t)$ given by (10.5), we write

$$|\vec{c}(\vec{p},t)|^2 = |\mathcal{N}|^2 \int_{-\infty}^{t}\int_{-\infty}^{t} \vec{E}(t_1) \cdot \vec{E}(t_2) e^{iI(\vec{p},t_1,t_2)+I_\alpha(t,t_1)+I_\alpha(t,t_2)}dt_1 dt_2 \tag{10.10}$$

Therefore,

$$\frac{\partial|\vec{c}(\vec{p},t)|^2}{\partial t} = |\mathcal{N}|^2 \int_{-\infty}^{t} \vec{E}(t)\cdot\vec{E}(t_1)e^{iI(\vec{p},t,t_1)+I_\alpha(t_1,t)}dt_1 + 2|\vec{c}(\vec{p},t)|^2\alpha(t) + c.c. \quad (10.11)$$

As long as avalanche cross-section $\alpha(t)$ contains field $\vec{E}(t)$ as a factor, ratio $\frac{\alpha(t)}{E(t)}$ is well-defined. We can now derive the expression for interband current in the presence of avalanche ionization

$$\vec{J}^{(t)}(t) = 2\sigma\vec{E}(t)w(t) - 2|\mathcal{N}|^2 \sum_{\vec{p}} \int_{-\infty}^{t} \vec{E}(t_1)\mathrm{Re}e^{iI(\vec{p},t,t_1)+I_\alpha(t,t_1)}\mathcal{E}(\vec{p}-\vec{A}(t)) \quad (10.12)$$

It is easy to see that in the absence of avalanche ionization, when $\sigma = I_\alpha(t) = 0$ Eq. (10.12) gives the same expression for $\vec{J}^{(t)}(t)$ as (8.42).

Since we introduced avalanche ionization coefficient as independent of momentum, modification to the ionization probability and photocurrents is straightforward

$$\begin{aligned} J_j^{(c)}(t) &= |\mathcal{N}|^2 \int_{-\infty}^{t}\int_{-\infty}^{t} dt_1 dt_2 \vec{E}(t_1)\cdot\vec{E}(t_2)e^{i(\mathcal{E}_g+D\Delta)(t_2-t_1)+I_\alpha(t,t_1)+I_\alpha(t,t_2)}\times \\ &\Delta J_1\left(|\Phi_j(t_2,t_1)|\right)\sin\left(d_jA_j(t)-\arg\Phi_j(t_2,t_1)\right)\prod_{i\neq j} J_0\left(|\Phi_i(t_2,t_1)|\right) \end{aligned} \quad (10.13)$$

$$\begin{aligned} J_j^{(c)}(t) &= |\mathcal{N}|^2 \int_{-\infty}^{t}\int_{-\infty}^{t} dt_1 dt_2 \vec{E}(t_1)\cdot\vec{E}(t_2)e^{i(\mathcal{E}_g+D\Delta)(t_2-t_1)+I_\alpha(t,t_1)+I_\alpha(t_2,t)}\times \\ &\Delta J_1\left(|\Phi_j(t_2,t_1)|\right)\sin\left(d_jA_j(t)-\arg\Phi_j(t_2,t_1)\right)\prod_{i\neq j} J_0\left(|\Phi_i(t_2,t_1)|\right) \end{aligned} \quad (10.14)$$

Interband current is given by

$$
\begin{aligned}
J_j^{(t)}(t) = 2\sigma E(t)w(t) + 2|\mathcal{N}|^2 \int_{-\infty}^{t} dt_1 E_j(t_1) e^{I_\alpha(t,t_1)} \cos(\mathcal{E}_g + \Delta)(t - t_1) \times \\
\times \Bigg[\prod_{j=1}^{D} J_0\left(|\Phi_j(t_2, t_1)|\right) (\mathcal{E}_g + \Delta) - \\
- \frac{\Delta}{D} \sum_{j=1}^{D} J_1\left(|\Phi_j(t, t_1)|\right) \cos\left(d_j A_j(t) - \arg \Phi_j(t, t_1)\right) \prod_{k \neq j} J_0\left(|\Phi_k^{(n)}(t, t_1)|\right) \Bigg]
\end{aligned}
\tag{10.15}
$$

where absorbed energy $w(t)$ is given by

$$
\begin{aligned}
w(t) = (\mathcal{E}_g + \Delta) W(t) - \frac{\Delta}{D} \int_{-\infty}^{t} \int_{-\infty}^{t} dt_1 dt_2 e^{i(\mathcal{E}_g + \Delta)(t_2 - t_1) + I_\alpha(t,t_1) + I_\alpha(t,t_2)} \times \\
\times \Bigg[\prod_{j=1}^{D} J_0\left(|\Phi_j(t_2, t_1)|\right) (\mathcal{E}_g + \Delta) - \\
- \frac{\Delta}{D} \sum_{j=1}^{D} e^{i(d_j A_j(t) - \arg \Phi_j(t,t_1))} J_1\left(|\Phi_j^{(n)}(t, t_1)|\right) \prod_{i \neq j} J_0\left(|\Phi_i(t_2, t_1)|\right) \Bigg]
\end{aligned}
\tag{10.16}
$$

and photoionization probability is given by

$$
\begin{aligned}
\rho(t) = & |\mathcal{N}|^2 \int_{-\infty}^{t} \int_{-\infty}^{t} dt_1 dt_2 \vec{E}(t_1) \cdot \vec{E}(t_2) e^{i(\mathcal{E}_g + D\Delta)(t_2 - t_1) + I_\alpha(t_1,t) + I_\alpha(t_2,t)} \times \\
& \times \prod_{j=1}^{D} J_0\left(|\Phi_j(t_2, t_1)|\right),
\end{aligned}
\tag{10.17}
$$

Let us now check the validity of our *ad hoc* approach by comparing results of avalanche-augmented field-cycle-resolved photoionization theory with the results of equation (10.1). It should be noted that we cannot compare the results of avalanche FCRPI with those of Schrödinger equation (8.5) simulations, because avalanche ionization is a multi-body effect that is not included into single-particle Schrödinger equation. Fig. 10.1(a) shows comparison of FCRPI results with and without avalanche. As expected, presence af the avalanche does not affect leading

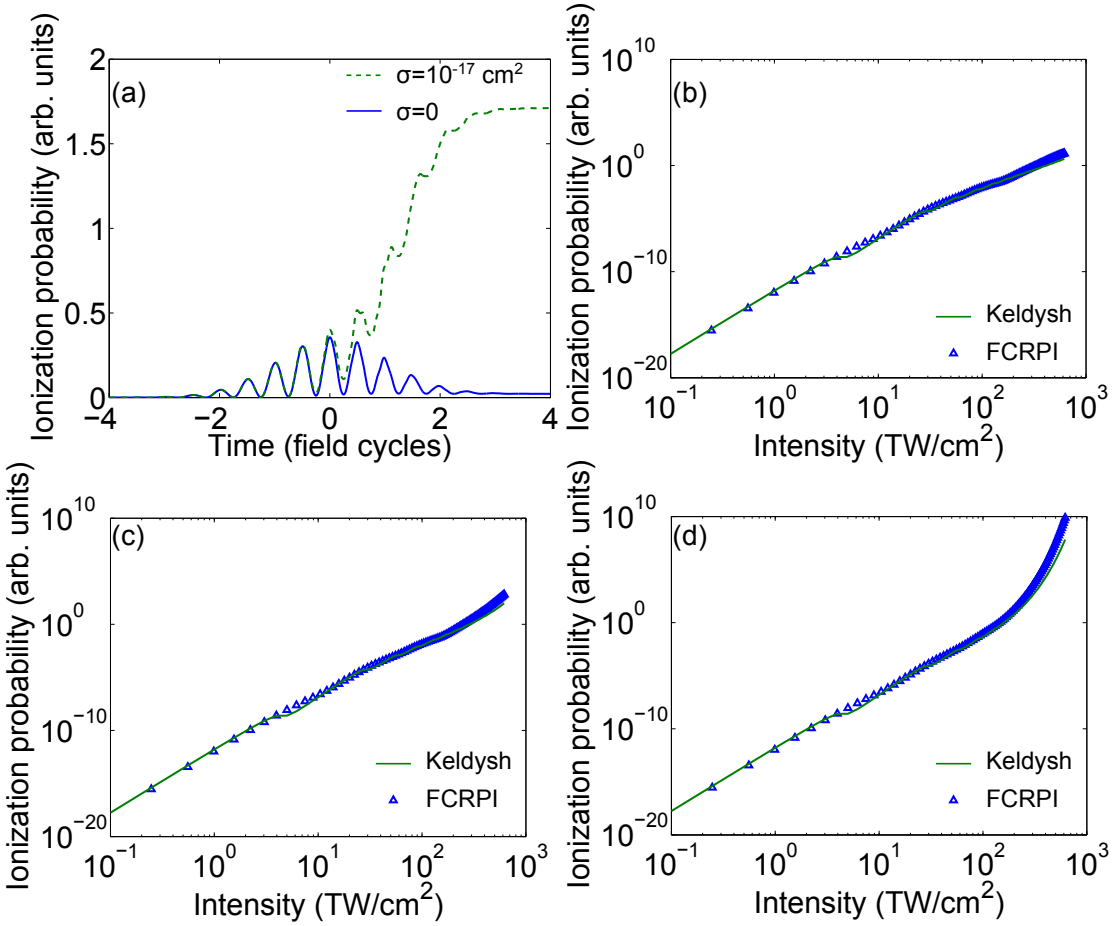

Figure 10.1 (a) CB population as a function of time without avalanche ionization (solid blue line), and with avalanche cross-section $\sigma = 10^{-17}$ cm^2 (dashed green line), calculated via FCRPI. Peak pulse intensity 150 TW/cm^2. (b)–(d) CB population in the wake of the pulse as a function of peak pulse intensity, calculated via Keldysh formula with avalanche ionization (Eq. (10.1), solid green line) and via FCRPI (triangles). Avalanche ionization cross-section is 1×10^{-18} cm^2 (b), 3×10^{-18} cm^2 (c), and 1×10^{-17} cm^2 (d). Pulse duration 2 cycles FWHM, central pulse wavelength 800 nm, material parameters mimic fused silica.

parts of the pulse, where ionization probability is relatively small. Once the avalanche ionization switches on close to the peak of the pulse, CB population grows almost monotonously, governed by avalanche ionization. Ionization probability in the wake of the pulse closely reproduces the results of equation (10.1).

The derivation of photoionization probability and photocurrent density in the presence of avalanche ionization in the dielectric with arbitrary separable dispersion (Section 9.2) is straightforward and left as an exercise for the reader.

To summarize, we have developed *ad hoc* approach that allows us to include avalanche ionization in our hamiltonian treatment of photoionization. This approach permits various functional dependencies of avalanche ionization rate on the strength of electric field (including non-instantaneous dependencies), as long as avalanche ionization cross-section contains electric field as a factor.

11. OPTICAL PROPERTIES OF SOLID-STATE PHOTOIONIZED PLASMA AT SUB-FIELD-CYCLE TIME SCALE

Optical properties of solid-state plasma is a vast multi-faceted subject studied theoretically and experimentally for many decades [107, 108, 109, 110, 111, 112], and still remaining an area of active research [92, 106, 113, 96, 114]. While steady-state properties of electrons and holes in solids plasma can be accessed through various well-established spectral-domain techniques [115, 116] and modelled using perturbation theory and self-consistent field approximation, ultrafast (femtosecond) transient changes in solid-state plasma are still of considerable interest because they uncover dynamics of various multi-body phenomena such as carrier-carrier scattering [108, 117], Coulomb screening [117, 112], and exciton formation [118]. At the same time, optical properties of solid-state plasma at femtosecond time scales are important for a number of high-power laser applications, including plasma mirrors [111], optical micromachining [119] and laser nanosurgery [120, 121].

At the shorter yet, subfemtosecond, time scales optical properties of solid-state plasma have been studied using high harmonic generation at the surface of the solid [122, 123] and in the bulk of the solid [106]. Recently, Brunel-type [124] process in solids, in which harmonics are generated due to sub-field-cycle dynamics of strong-field photoionization [13, 94, 39, 40] has been employed to study tunneling ionization in solids via low-order optical harmonics [92]. Direct time-resolved experiments with attosecond pulses [113, 114], as well as carrier-envelope-stabilized few-cycle near-infrared pulses [96] have demonstrated field-induced electron tunneling occuring at the attosecond time scales and opening venues for light-wave-controlled solid-state electronics [96].

At the same time, optical response of the photoionized plasma that determines how does intense ultrashort pulse change while propgating through the solid or reflecting off its surface is usually calculated either using fully quantum simulations with time-dependent Schrödinger equation (TDSE) or time-dependent density-functional theory (TD-DFT), or, more commonly, with assumption that plasma density varies slowly with time [18, 19, 125].

In this paper we present a two-band quantum-mechanical model of optical properties of solid-state plasma in sub-field-cycle time scales, valid for a wide range of intensities, pulse shapes and frequencies (both of incident radiation and of nonlinear response). Our approach recovers known expressions for refraction and absorption of semiconductors in the limit of low intensities.

Generally speaking, optical polarization $\vec{P}(t)$ and current density $\vec{J}(t)$ in plasma can be written in the following form

$$P_i(t) = \int_{-\infty}^{t} \chi_{ij}(t,t')E_j(t')dt' \tag{11.1}$$

$$J_i(t) = \int_{-\infty}^{t} \sigma_{ij}(t,t')E_j(t')dt' \tag{11.2}$$

where subscripts i, j denote Cartesian components of vectors, and $\vec{E}(t)$ is electric field, $\chi_{ij}(t,t')$ is dielectric susceptibility tensor, and $\sigma_{ij}(t,t')$ is conductivity tensor. Formulas (11.1) and (11.2) give a transparent physical meaning to time arguments t and t', namely, $\chi_{ij}(t,t')$ ($\sigma_{ij}(t,t')$) shows with which weight electric field at time t' contributes to polarization (current density) at time t. In the stationary linear case, $\chi_{i,j}(t,t') = \chi_{ij}(t-t')$ and $\sigma_{ij}(t,t') = \sigma_{ij}(t-t')$, and thus it is possible to write in the

spectral domain

$$\hat{P}_i(\omega) = \hat{\chi}_{ij}(\omega)\hat{E}_j(\omega) \tag{11.3}$$

$$\hat{J}_i(\omega) = \hat{\sigma}_{ij}(\omega)\hat{E}_j(\omega) \tag{11.4}$$

where

$$\hat{\chi}_{jk}(\omega) = \int_0^\infty e^{i\omega(t-t')}\chi_{jk}(t-t')d(t-t') \tag{11.5}$$

$$\hat{\sigma}_{jk}(\omega) = \int_0^\infty e^{i\omega(t-t')}\sigma_{jk}(t-t')d(t-t') \tag{11.6}$$

are complex dielectric susceptibility and complex conductivity as functions of a single frequency argument ω.

We also note that description of optical properties with current density and conductivity is equivalent to the description with polarization and dielectric susceptibility, because there is the following relation between polarization and current density

$$\vec{J}(t) = \frac{d\vec{P}(t)}{dt} \tag{11.7}$$

hence,

$$\sigma_{ij}(t,t') = \frac{\partial\chi_{ij}(t,t')}{\partial t} + \chi_{ij}(t,t)\delta(t-t') \tag{11.8}$$

where $\delta(\tau)$ is a Dirac delta function. Conversely,

$$\vec{P}(t) = \int_{-\infty}^{t} \vec{J}(t_1)dt_1 \tag{11.9}$$

hence,

$$\chi_{ij}(t,t') = \int_{t'}^{t} \sigma_{ij}(t_1,t')dt_1 \tag{11.10}$$

11.1 Slowly-varying plasma density approach (SVPD)

Popular approach to calculate optical properties of plasma is to assume plasma density is varying slowly [18, 19, 125]. Equations of motion of a single electron in collisionless plasma give the velocity of a electron as a function of time (in what follows we use units $\hbar = |e| = 1$)

$$\vec{v}(t) = -\frac{1}{m}\vec{A}(t) \tag{11.11}$$

where

$$\vec{A}(t) = \int_{-\infty}^{t} \vec{E}(t')dt' \tag{11.12}$$

is vector potential. The conductivity current in the collisionless plasma is then found as electron density and vector potential

$$\vec{J}^{(c)}(t) = -\rho(t)v(t) = \frac{\rho(t)A(t)}{m}, \tag{11.13}$$

or, equivalently,

$$\sigma_{ij}^{(c)}(t,t') = \delta_{ij}\rho(t)/m \tag{11.14}$$

where m is conduction-band electron mass. Expressions (11.11), (11.13) and (11.14) can be extended to include collisions with time constant τ_c as

$$\vec{v}(t) = -\frac{1}{m}\int_{-\infty}^{t} \vec{E}(t')e^{(t'-t)/\tau_c}dt' \tag{11.15}$$

$$\vec{J}^{(c)}(t) = \frac{\rho(t)}{m}\int_{-\infty}^{t} \vec{E}(t')e^{(t'-t)/\tau_c}dt' \tag{11.16}$$

and,

$$\sigma_{ij}^{(c)}(t,t') = \delta_{ij}\rho(t)e^{(t'-t)/\tau_c}/m \tag{11.17}$$

where δ_{ij} is Kronecker symbol.

Interband current can found via energy conservation [18, 19] and reads

$$\vec{J}^{(i)}(t) = \frac{\mathcal{E}_g \vec{E}(t)}{E^2(t)} \frac{d\rho(t)}{dt} \tag{11.18}$$

Hence

$$\sigma_{ij}^{(i)}(t,t') = \delta_{ij} \frac{\mathcal{E}_g}{E(t)^2} \frac{d\rho(t)}{dt} \delta(t-t') \tag{11.19}$$

To complete the model given by Eqs. (11.14),(11.14) and (11.19), we need to specify plasma density as a function of time $\rho(t)$. It can be found by solving the kinetic equation (2.6). For ultrashort pulses second and third terms in (2.6) can often be neglected, in which case plasma density is found by integrating photoionization rate with respect to time

$$\rho(t) = \int_{\infty}^{t} W(E(t'), \omega_0) dt' \tag{11.20}$$

where $W(E(t), \omega_0)$ is photoionization rate as a function of field strength and central pulse frequency ω_0. Besides an obvious approximation of slowly varying plasma density, SVPD tacitly assumes known photoionization rate as a function of field strength. Time-averaged nonlinear photoionization rates, such as Keldysh formula [13],[94] may also become inappropriate at sub-field-cycle time scales.

11.2 Optical properties at sub-field-cycle time scale

Using the field-cycle-resolved photoionization formalism developed in sections 8 and 9, we can write down intraband conductivity $\sigma_{ij}^{(c)}(t,t')$ as

$$\sigma_{ij}^{(c)}(t,t') = 2|\mathcal{N}|^2 \int_{-\infty}^{t'} dt_1 E_j(t_1) \sin[(\mathcal{E}_g + \Delta)(t' - t_1)] \prod_{k \neq i} J_0\left(|\Phi_k(t', t_1)|\right) \times \\ \times \frac{\Delta}{D} J_1\left(|\Phi_i(t', t_1)|\right) \sin\left(d_i A_i(t) - \arg \Phi_i(t', t_1)\right) \tag{11.21}$$

and interband conductivity $\sigma_{ij}^{(i)}(t,t')$ as

$$\sigma_{ij}^{(i)}(t,t') = 2\delta_{ij}|\mathcal{N}|^2 \Bigg[\cos[(\mathcal{E}_g + \Delta)(t - t')] \prod_{k=1}^{D} J_0\left(|\Phi_k(t,t')|\right) (\mathcal{E}_g + \Delta) - \\ - \frac{\Delta}{D} \sin[(\mathcal{E}_g + \Delta)(t - t')] \sum_{k=1}^{D} J_1\left(|\Phi_k(t,t')|\right) \cos\left(d_k A_k(t) - \arg \Phi_k(t,t')\right) \prod_{l \neq k} J_0\left(|\Phi_l(t,t')|\right) \Bigg] \tag{11.22}$$

where $\mathcal{E}_g$ is band gap, Δ is band width, D is number of spatial dimensions, $|\mathcal{N}|^2$ is normalization factor, $J_0(z)$ and $J_1(z)$ are zeroth and first order Bessel functions of the first kind, respectively, d_j is lattice constant in direction j, $\vec{A}(t) = \int_{-\infty}^{t} \vec{E}(t')dt'$ is vector potential,

$$\Phi_j(t_1, t_2) = \frac{\Delta}{D} \int_{t_1}^{t_2} e^{i d_j A_j(t')} dt', \tag{11.23}$$

Inspection of formulas (11.21) and (11.22) shows that as field amplitude goes to zero, $|\vec{E}| \to 0$,

$$\sigma_{ij}^{(c)}(t,t') \to 0 \tag{11.24}$$

$$\sigma_{ij}^{(i)}(t,t') \to \overline{\sigma}_{ij}^{(i)}(t - t') \tag{11.25}$$

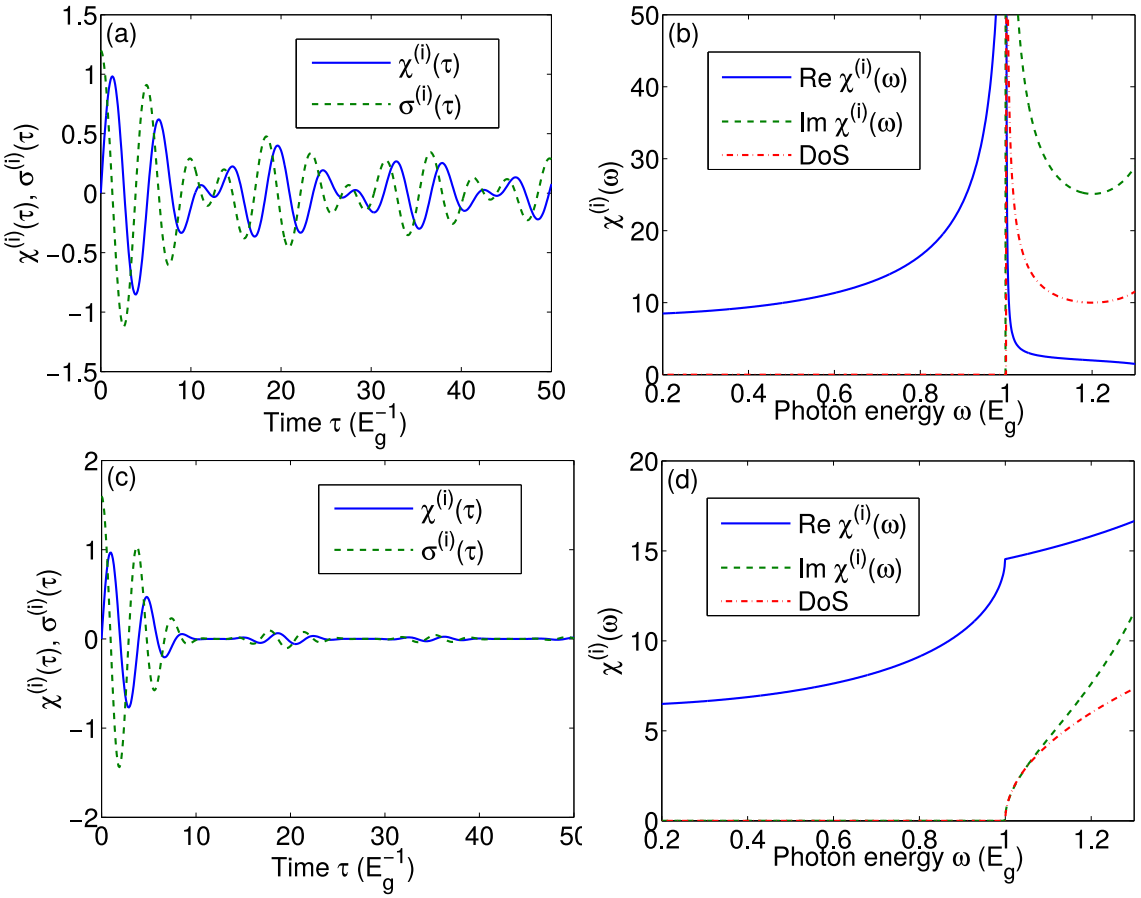

Figure 11.1 (a),(c) Linear interband single time response functions $\overline{\chi}^{(}i)(\tau)$ (solid blue line) and $\overline{\sigma}^{(i)}$ (dashed blue line). (b),(d) Frequency-dependent linear dielectric susceptibility $\hat{\chi}^{i}(\omega)$ - real part (solid blue line), imaginary part (dashed green line), and density of states in the two-band model (arb. units, red dash-dotted line) as functions of photon energy in the units of band gap energy. Number of spatial dimensions $D = 1$ (a),(b) and $D = 3$ (c),(d). In the panel (d) approximate density of states in the parabolic band approximation is plotted.

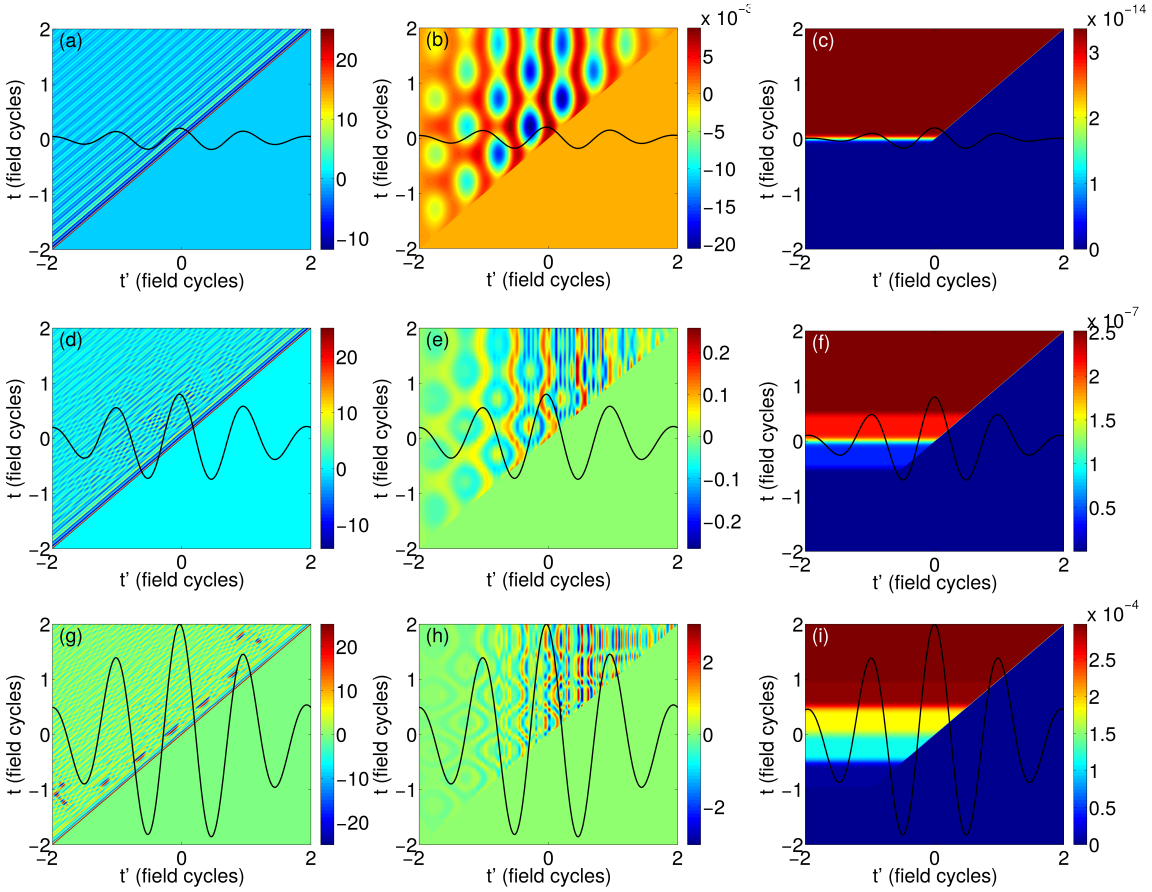

Figure 11.2 Maps of (a),(d),(g) $\sigma^{(i)}(t,t')$, (b),(e),(h) $\sigma^{(c)}(t,t')$, calculated using FCRPI, and (c),(f),(i) $\sigma^{(c)}(t,t')$, calculated using slowly-varying plasma density approach for input pulse intensity (a)–(c) 2.6 TW/cm^2, (d)–(f) 41 TW/cm^2 and (g)–(i) 260 TW/cm^2. $D = 1$, $\mathcal{E}_g = 9$ eV, $\Delta = 0.2\mathcal{E}_g$, central radiation frequency $0.2\mathcal{E}_g$, pulse duration 1 cycle FWHM. Solid black line shows electric field profile as a function of time t'.

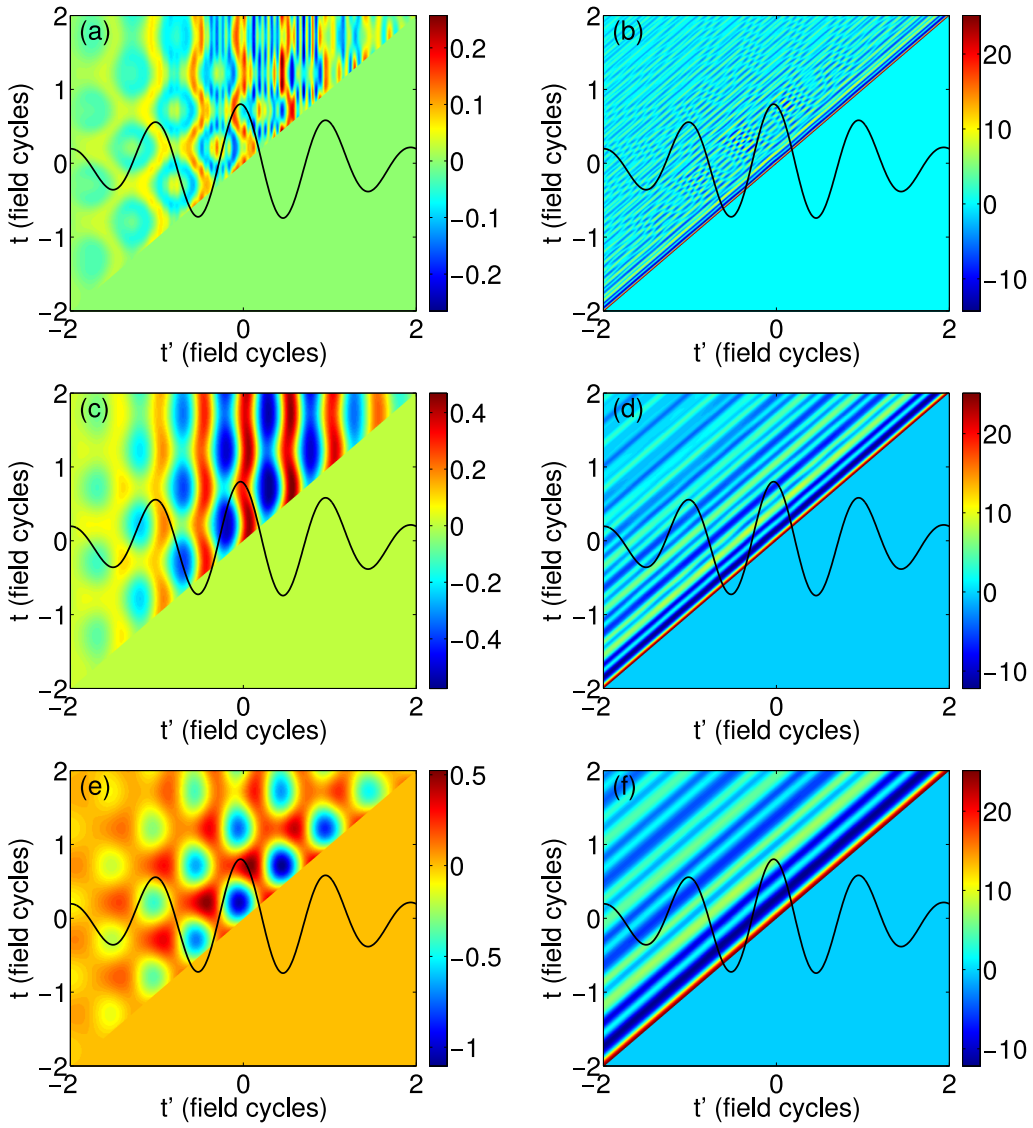

Figure 11.3 Maps of (a),(c),(d) $\sigma^{(c)}(t,t')$ and (b),(d),(f) $\sigma^{(i)}(t,t')$ for central radiation frequency (a),(b) $0.2\mathcal{E}_g$, (c),(d) $0.6\mathcal{E}_g$ and (e),(f) $1.1\mathcal{E}_g$. Input pulse intensity 41 TW/cm^2, $D = 1$, $\mathcal{E}_g = 9$ eV, $\Delta = 0.2\mathcal{E}_g$, pulse duration 1 cycle FWHM. Solid black line shows electric field profile as a function of time t'

where

$$\overline{\sigma}_{ij}^{(i)}(\tau) = 2\delta_{ij}|\mathcal{M}|^2\Bigg[\cos[(\mathcal{E}_g+\Delta)\tau](\mathcal{E}_g+\Delta)\left(J_0\left(\frac{\Delta}{D}\tau\right)\right)^D - \\ -\sin[(\mathcal{E}_g+\Delta)\tau]\Delta J_1\left(\frac{\Delta}{D}\tau\right)\left(J_0\left(\frac{\Delta}{D}\tau\right)\right)^{D-1}\Bigg] \tag{11.26}$$

We plot linear interband conductivity and linear dielectric susceptibility $\overline{\chi}^{(i)}(\tau) = \int_{-\infty}^{\tau}\overline{\sigma}^{(i)}(\tau')d\tau'$ at low intensities as a function of time τ, and in spectral domain as a function of frequency ω for 1-D and 3-D solid [Fig. 11.1]. As expected, linear absorption coefficient, proportional to imaginary part of $\hat{\chi}^{(i)}(\omega)$, follows density of states in the in the two-band solid [Fig. 11.1(b),(c)] [116]. In 1-D solid, density of states has a $(x^2-1)^{-1/2}$-type singularity in the vicinity of the band gap, and so does $\mathrm{Im}\hat{\chi}^{(i)}(\omega)$ [Fig. 11.1(b)]. In the 3-D solid singularity of density of states is softer, of $(x-1)^{1/2}$-type, which is reflected in $\mathrm{Im}\hat{\chi}^{(i)}(\omega)$ [Fig. 11.1(d)]. In the time domain linear optical response of 3-D solid decays faster than that of 1-D solid.

Figure 11.2 shows maps of $\sigma^{(c)}(t,t')$ and $\sigma^{(i)}(t,t')$ for various field pulse intensities for $D=1$. At small pulse intensities, when $A_i d_i \ll 1$, and away from the peak of the pulse intraband conductivity $\sigma_{ij}^{(c)}(t,t')$, in accord with (11.24), vanishes, whereas interband conductivity $\sigma^{(i)}(t,t')$ becomes a function of a single argument $t-t'$ [Figs. 11.2(a)]. Although in the regime of low intensities optical response is governed by interband transitions, we note drastically different behaviour of intraband coductivity $\sigma^{(c)}(t,t')$, predicted by FCRPI and by slowly-varying plasma density approximation [Fig. 11.2(b),(c)]. While in SVPD approximation $\sigma^{(c)}(t,t')$ slowly changes as a function of t and does not depend on t' [Fig. 11.2(c)] , FCRPI predicts oscillatory behaviour of intraband conductivity [Fig. 11.2(b)] that manifests itself in harmonic generation. At higher intensities nonlinear interband and intraband responses become comparable [Fig. 11.2(d),(e),(g),(h)], with $\sigma^{(i)}(t,t')$ also exhibiting complex

dependence on both t and t' [Fig. 11.2(d),(g)].

Formulas (11.21) and (11.22) are valid for arbitrary radiation frequency, as long as dipole approximation holds and population of the conduction band is small (see Supplementary Material). Figure (11.3) shows continuous transition of the conductivity functions from the regime when pulse frequency is smaller than the band gap to the regime with pulse frequency is larger than the band gap, with the peak field intensity kept constant. As the frequency increases, peak values of vector potential decrease (with field strength kept fixed), hence, maps of intraband conductivity $\sigma^{(c)}(t,t')$ show low-intensity patterns [Fig. 11.3)(a),(c),(d)]. At the same time, period of oscillations of $\sigma^{(i)}(t,t')$ approaches field cycle duration as field frequency increases [Fig. 11.3)(a),(c),(d)], indicating linear interband absorption.

11.3 FDTD simulations of transmission and reflection at the vacuum-solid interface

The current density and polarization, calculated (11.1), (11.2), and (11.21), (11.22),(11.8), can be plugged into various propagation codes to analyse transformation of the powerful pulse during propagation through dielectric, generation of high harmonics etc. It should be noted, however, that accurate numerical integration over time in the expressions (11.2) requires time step smaller than typical time of oscillations of $\sigma_{ij}(t,t')$, which, for $\sigma_{ij}^{(i)}(t,t')$ is on the order of $\mathcal{E}_g^{-1}$ (Eq. (11.22), Fig. 11.2(b),(d),(f)] . For example, for fused silica with $\mathcal{E}_g = 9$ eV reliable convergence is achieved for $\Delta t \leq 70$ as. On the other hand, our field-cycle-resolved photoionization theory [40] can predict oscillations of electron density on the order of critical plasma density, potentially causing back-reflections of the propagating wave. The propagations codes for filamentation [42, 43, 18, 19] are thus not very well-suited for modelling field-cycle-resolved photoionization, because those codes assume relatively smooth dynamics of the field (when considered in the time frame co-moving with the pulse), and absence of the back-reflected wave.

In this paper we instead employ finite-difference time-domain (FDTD) method [126, 127] to analyze pulse propagation in the presence of photoionization at subcycle time scale. FDTD is a very popular method of directly solving Maxwell equations for electric and magnetic fields, and has been applied to a large variety of problems, including propagation of radar signals [128, 129, 130], nanophotonics [131, 132, 133, 134], and plasmonics [135, 136, 137, 138]. Quantum-mechanical simulations of 4-level media have been also successfully combined with FDTD [139]. Due to its popularity, there is a number of free [140] and proprietary software packages for FDTD simulations. However, as the stability of the simulations depends crucially

on material parameters, these software packages do not allow specification of arbitrary photocurrents and polarization as source terms. Therefore, we implement our own FDTD code that treats very simple 1-D geometry in which light pulse is incident in the z direction normally onto vacuum–dielectric interface from the vacuum side. We assume electric field is polarized along one of the crystal directions, hence, photocurrents are also polarized in the same direction, and we only need to keep track of one component of the field. Specifically, we solve the following equations for x-component of electric displacement D_x

$$\frac{1}{c}\frac{\partial D_x}{\partial t} = \frac{\partial H_y}{\partial z} - 4\pi J_x \tag{11.27}$$

$$\frac{1}{c}\frac{\partial H_y}{\partial t} = \frac{\partial D_x}{\partial z} - 4\pi \frac{\partial P_x}{\partial z} \tag{11.28}$$

Here $D_x = E_x + 4\pi P_x$, E_x is x-component of the field, P_x is x-component of polarization, J_x is x-component of current, H_y is y-component of magnetic field, c is speed of light in vacuum, and vacuum-dielectric interface lies in $x-y$-plane. FDTD step is then given by the following equations

$$D_j^{n+1} = D_j^n + \frac{c\Delta t}{\Delta z}\left(H_{j+1/2}^{n+1/2} - H_{j-1/2}^{n+1/2}\right) - 4\pi c\Delta t J_j^{(c),n} \tag{11.29}$$

$$H_{j+1/2}^{n+1/2} = H_{j+1/2}^n + \frac{c\Delta t}{\Delta z}\left(D_{j+1}^n - D_j^n - 4\pi\left(P_{j+1}^n - P_j^{(t),n}\right)\right) \tag{11.30}$$

where j denotes spatial index (along z coordinate), n denotes temporal index (along t coordinate), and we have omitted Cartesian indices x and y for brevity. In vacuum, $J^{(c)}(t) = P^{(i)}(t) = 0$. In dielectric we calculate J_x using (11.2) and (11.21) (or (11.14)), and P_x using (11.1), (11.8) and (11.22) (or (11.19)). We include intraband transitions through the current density term in (11.27), and interband transitions through polarization term in (11.28), because interband transitions provide positive

contributions to the refractive index even at small fields (Eq. (11.25)) and cause numerical instability if included through current density term, and intraband transitions provide negative contribution to the refractive index and can cause instability if included through polarization term.

We also notice that, strictly speaking, equations (11.29) and (11.30) provide solution for displacement $D(t)$, whereas formulas (11.21), (11.22) require field $E(t)$ and intergral of the field in vector potential $A(t)$. In the input of formulas (11.21), (11.22) we use estimate $E(t) \approx D(t)/\epsilon(\omega_0)$, where $\epsilon(\omega_0)$ is dielectric constant at central pulse frequency ω_0.

Fig. 11.4(a),(c),(d) shows maps of electric field in the vicinity of vacuum-dielectric interface. Further insight into the process of reflection at the vacuum-dielectric boundary can be gained if we plot fraction of the energy of the input pulse that is contained in the field in vacuum, in dielectric and stored by electron-hole pairs in plasma. Specifically,

$$\mathcal{R}(t) = \frac{\int_{V_v}(E^2+H^2)|_t dv}{\int_{V_v}(E^2+H^2)\ |_{t=0} dv} \tag{11.31}$$

where $\int_{V_v} dv$ denotes integration over volume of vacuum, gives fraction of the initial pulse energy contained in vacuum at the time moment t. Similarly,

$$\mathcal{T}(t) = \frac{\int_{V_d}(E^2+H^2)|_t dv}{\int_{V_v}(E^2+H^2)\ |_{t=0} dv} \tag{11.32}$$

where $\int_{V_d} dv$ denotes integration over the volume of dielectric, gives the fraction of the energy of the input pulse, stored by the field within the dielectric. Fraction of the energy of the input pulse, stored by electron-hole pairs within the dielectric, can

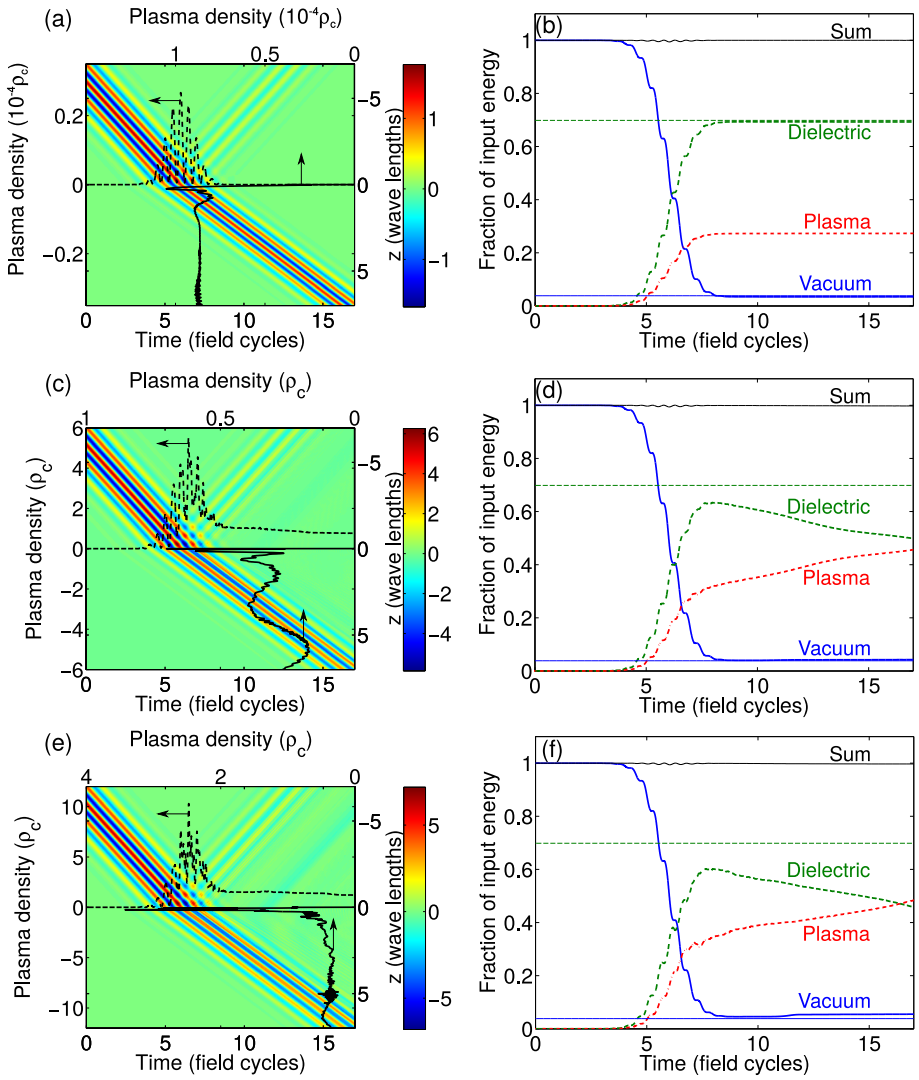

Figure 11.4 (a),(c),(e) Maps of the electric field (in V/A) in the vicinity of vacuum-dielectric interface calculated by FDTD+FCRPI. Solid black line (left-bottom axis) shows plasma density on the surface as a function of time, and dashed black line (top-right axis) shows plasma density in the wake of the pulse as a function of depth. (b),(d),(f) Fraction of the initial energy of the pulse contained in vacuum (solid blue line), in field within the dielectric (dashed green line) and in electron-hole pairs within the dielectric (dash-dotted red line) as functions of time. Sum $\mathcal{R}(t) + \mathcal{T}(t) + \mathcal{P}(t)$ is shown by thin black line, Fresnel reflection and transmission coefficients are shown by thin solid blue line and thin dashed green line respectively. Peak intensity of the incident pulse is (a),(b) 50 TW/cm^2, (c),(d) 300 TW/cm^2 , (e),(f) 400 TW/cm^2. Incident pulse duration is 2 cycles FWHM, central pulse wavelength 800 nm, ionization parameters mimic fused silica.

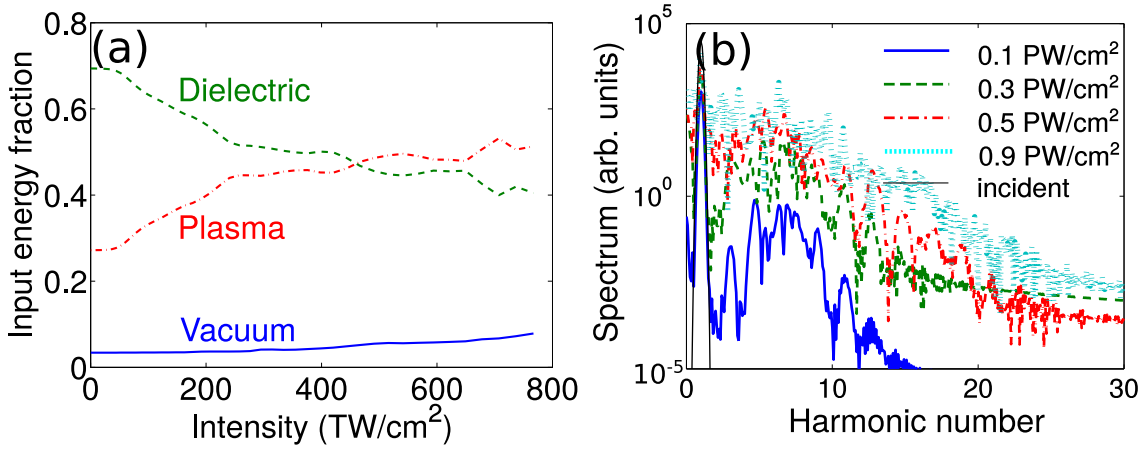

Figure 11.5 (a) Fraction of input pulse energy reflected (solid blue line), stored in the field inside the dielectric (dashed green line) and in plasma inside the dielectric (dash-dotted red line) at $t = 17$ cycles as functions of incident pulse intensity, calculated using FDTD+FCRPI. (b) Spectra of the reflected pulse for various incident pulse intensities: 10^{14} W/cm^2 (solid blue line), 3×10^{14} W/cm^2 (dashed green line) , 5×10^{14} W/cm^2 (dash-dotted red line), and 9×10^{14} W/cm^2 (dotted cyan line). Spectrum of the incident pulse is shown by thin black line.

be found by integrating Ohmic losses due to currents within plasma

$$\mathcal{P}(t) = 8\pi \frac{\int_{V_d}\int_{-\infty}^{t} E(t')\cdot J(t')dt'dv}{\int_{V_v}(E^2+H^2)|_{t=0}dv} \tag{11.33}$$

In the low-intensity linear limit $\mathcal{R}(t\to\infty)$ and $\mathcal{T}(t\to\infty)$ can be calculated using well-known Fresnel formulas [141] for electric and magnetic fields of reflected and transmitted wave to yield

$$\mathcal{R}^F = \left(\frac{1-\sqrt{\epsilon}}{1+\sqrt{\epsilon}}\right)^2 \tag{11.34}$$

$$\mathcal{T}^F = \frac{2(1+\epsilon)}{\sqrt{\epsilon}(1+\sqrt{\epsilon})^2} \tag{11.35}$$

$$\mathcal{P}^F = \frac{2(\epsilon - 1)}{\sqrt{\epsilon}(1 + \sqrt{\epsilon})^2} \tag{11.36}$$

At low pulse intensities, constant portion of the energy is stored in the electron-hole plasma, corresponding to dielectric polarization due to interband transitions [Fig. 11.4(b)]. When $t \to \infty$, $\mathcal{R}$ and $\mathcal{T}$ coincide with $\mathcal{R}^F$ and $\mathcal{T}^F$, respectively. At higher intensities, energy of the pulse is being spent as the pulse propagates into dielectric [Fig. 11.4(b)], while transmitted and reflected pulses develop new frequency components [Fig. 11.4(c),(d), Fig. 11.5(b)], which, in turn, affect both instantaneous plasma density and the plasma density in the wake of the pulse.

We can compare these results with FDTD+SVPD model [Fig. 11.6]. Distribution of energy between vacuum, dielectric and plasma is similar at small intensities [Figs. 11.6(b), 11.4(b)], but differs dramatically at medium and high intensities [Figs. 11.6(d),(f), 11.4(d),(f)]. In the SVPD approximation, shape of the reflected pulse is virtually the same as the shape of the incident pulse, whereas transmitted pulse is slowly modified by the plasma dispersion [Fig. 11.6(e)]. Density of plasma in the wake of the pulse varies slowly with depth.

To summarize, we develop a quantum-mechanical model of optical response of solid-state plasma in photoionized transparent solid at sub-field-cycle time scale. Our model is valid in a wide range of intensities, radiation frequencies and pulse shapes, and shows nonlinear dependence of optical properties, arising both from interband and intraband motion of electrons, on field intensity. Analysis of transmission and reflection of ultrashort pulse at vacuum-solid boundary with FDTD code shows complex coupled field-charge dynamics, not present in description of optical properties using slowly varying plasma density approximation.

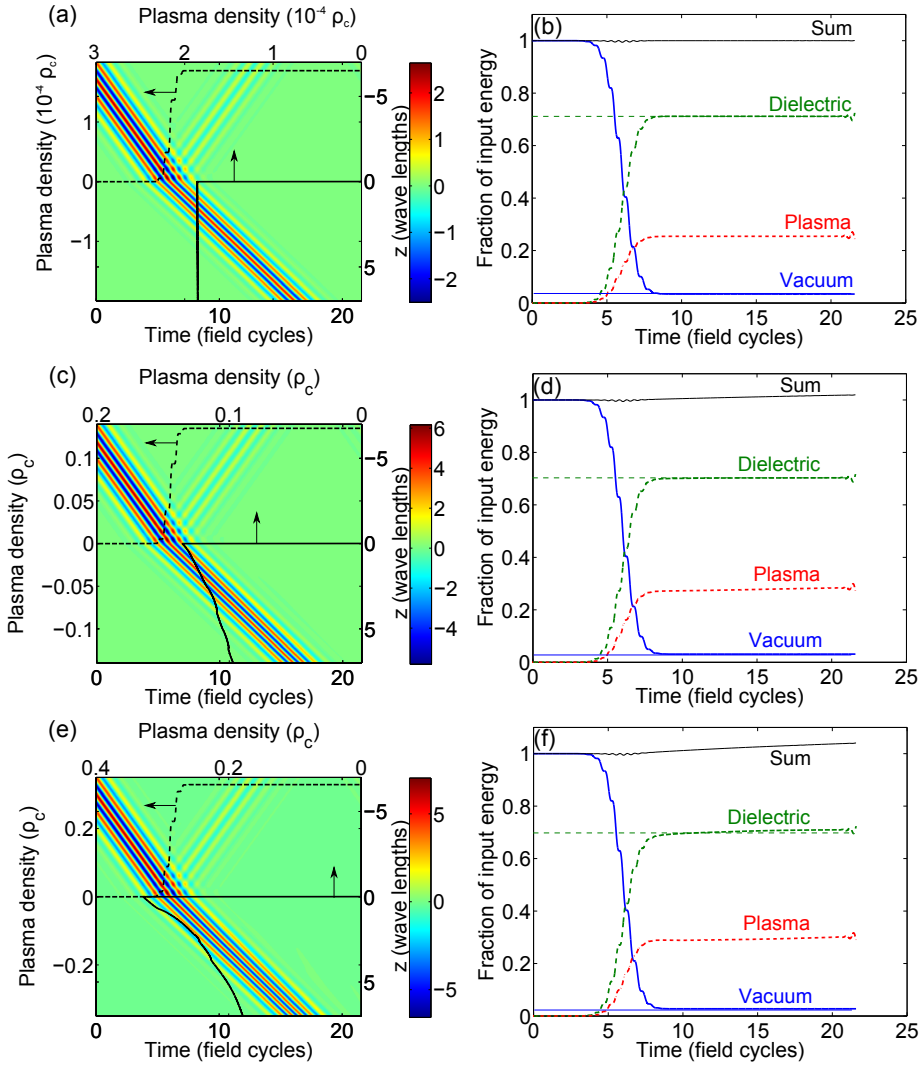

Figure 11.6 (a),(c),(e) Maps of the electric field (in V/A) in the vicinity of vacuum-dielectric interface calculated by FDTD + SVPD. Solid black line (left-bottom axis) shows plasma density on the surface as a function of time, and dashed black line (top-right axis) shows plasma density in the wake of the pulse as a function of depth. (b),(d),(f) Fraction of the initial energy of the pulse contained in vacuum (solid blue line), in field within the dielectric (dashed green line) and in electron-hole pairs within the dielectric (dash-dotted red line) as functions of time. Sum $\mathcal{R}(t) + \mathcal{T}(t) + \mathcal{P}(t)$ is shown by thin black solid line, Fresnel reflection and transmission coefficients are shown by thin solid blue line and thin dashed green line respectively. Peak intensity of the incident pulse is (a),(b) 50 TW/cm^2, (c),(d) 300 TW/cm^2 , (e),(f) 400 TW/cm^2. Incident pulse duration is 2 cycles FWHM, central pulse wavelength 800 nm, ionization parameters mimic fused silica.

12. OPTICAL BREAKDOWN BY ULTRASHORT LASER PULSES

Laser-induced breakdown of solid materials has been a subject of in-depth research since the invention of lasers [142, 143]. Systematic experimental studies performed within more than five decades have revealed distinctly different physical scenarios leading to optical breakdown in materials irradiated by long [86, 144] and short [4] laser pulses and helped identify a broad range of physical processes contributing to laser-induced breakdown [145], including field-induced and avalanche ionization, nonlinear dynamics of a laser beam, plasma effects, radiation absorption by impurity and defect states, as well as collisional dynamics, diffusion, and recombination of free carriers.

While the specific regime of laser-induced breakdown can depend on all the above-listed factors, ionization dynamics and the related buildup of free-carrier density always play a central role in laser breakdown, providing a mechanism whereby the laser field is coupled to a material. This fact is recognized by a broadly accepted criterion of laser-induced breakdown [145, 100, 146, 147, 19, 18, 121] that defines the laser breakdown threshold in terms of the laser fluence or laser intensity needed to generate a certain fraction of the critical electron density within the laser pulse. This criterion has proven to be useful in a broad range of pulse widths, offering a powerful tool for the analysis of a laser breakdown by pico- and femtosecond light pulses and helping understand a variety of related laser–matter interaction phenomena in a broad class of materials and systems, including laser-induced filamentation [147, 19, 18, 148], laser micromachining [119], laser biomedicine [121, 120], supercontinuum generation [19, 18, 149], and compression [125, 150, 151] of high-power laser pulses in solids. Here, we show, however, that this commonly accepted approach to assessing

the role of laser-induced breakdown in solids fails in the case of extremely short, few-cycle laser pulses. The physical arguments offered in this work suggest that the laser breakdown threshold of solids should be rather defined in terms of the absorbed laser energy per unit volume and energy transfer to the crystal lattice.

In the case of few-cycle laser pulses, application of criterion

$$\rho > s\rho_c(\omega_0), \tag{12.1}$$

where ρ is density of conduction band (CB) electrons, $\rho_c(\omega)$ is critical plasma density, and s is the fraction of critical plasma density that leads to the breakdown, meets the following difficulties. Firstly, the notion of central frequency is not very well defined for ultrabroad band single-cycle pulses. In the commonly used set-ups to study breakdown threshold as a function of pulse duration pulse duration is varied by adjusting chirp of the pulse [152, 100, 4, 101]. For ultrabroandband chirped pulses central frequency ω varies with time; clearly, application of breakdown criterion of the $\rho(t) > s\rho_c(\omega(t))$ should then give different results for positively and negatively chirped pulses, while experimentally this is not observed. Fundamentally, expression (12.1) contains Fourier-conjugated variables - time through $\rho(t)$ and frequency through $\rho_c(\omega)$ - in the same expression, and thus will inevitably run into inconsistensies at timescales comparable to field cycle.

Secondly, our recent revision of Keldysh photoionization theory [13] for solids shows that density of electrons in the conduction band exhibits strongly non-monotonous, oscillatory behaviour at sub-field-cycle time scales [40]. Within the field cycle plasma density can be comparable to the critical plasma density; while plasma density in the wake of the pulse can be relatively low. This corroborates necessity of revision of the criterion (12.1) – we can take maximum $\max_t \rho(t)$ or $\rho(t \to \infty)$ in the wake

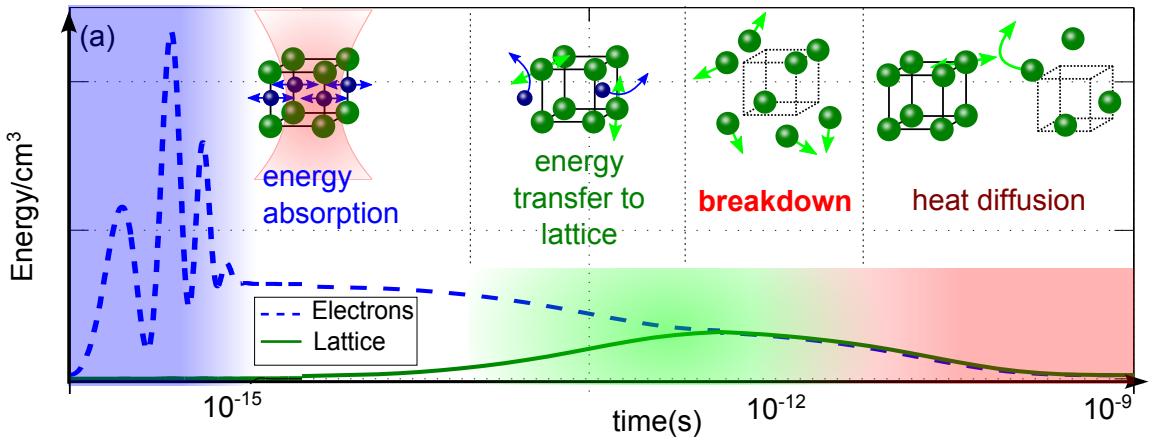

Figure 12.1 Energy transfer diagram. Dashed blue line shows energy per unit volume stored in the electronic subsystem; solid green line shows energy per unit volume stored in the lattice subsystem. Energy is absorbed into electronic sub-system during first few femtoseconds of the pulse, and transferred to the lattice on the picosecond time scale. Heat diffusion takes place on picosecond-nanosecond time scale; breakdown occurs between energy transfer to the lattice and energy dissipation through thermal conductivity.

of the pulse as plasma density ρ with clearly different predictions for optical breakdown threshold. On the other hand, accurate theoretical answer to both questions is of paramount importance for current and future applications of laser micro- and nanomachining and nanosurgery with ultrashort pulses [119, 120, 153, 121].

In sections 8–10 we have developed quantum-mechanical formalism to calculate photoionization probability and photocurrent density at sub-cycle time scales, and then in section 11 we have applied this formalism to analyse how powerful ultrashort pulse penetrates dielectric in the conditions of ultrafast ionization. We have shown that certain portion of energy can propagate into dielectric, although the maximum population of conduction band exceeds $\rho_c(\omega_0)$. Here, we focus on applying our field-cycle-resolved photoionization theory to the problem of optical breakdown and adopt the following picture [Fig. 12.1] Typical timescales of electron-lattice collisions are

1 fs – 1ps. At this time scale electrons forget history of irradiation and collective motion due to the field, but retain acquired energy. Energy transfer times are correspondingly m_e/M times larger (here M is mass of ion or atom in the lattice site, and m_e is mass of electron). Therefore, in the case of the femtosecond pulse-induced optical breakdown the electrons store the energy during the pulse; the transfer of this energy to the lattice and actual structural changes (breakdown) happen in the wake of the pulse [100]. Typical energy escape time thorough heat diffusion can be estimated from below as $\tau_h = \lambda^2/\chi$, where χ is thermal conductivity (in units of $\mathrm{m^2 s^{-1}}$), $\lambda = 2\pi c/\omega$ is the radiation wavelength, determining minimal size of the irradiated volume, and c is speed of light. Thermal conductivity of dielectric with plasma can be expected to be larger than thermal conductivity of a cold medium due to electronic contribution; consequently, is on the order 1 ps – 10ns. This hierarchy of energy transfer timescales [Fig. 12.1] enables an estimate of the breakdown time between energy transfer to the lattice and heat diffusion; and allows us to base a physically transparent criterion of optical breakdown on the amount of energy per unit volume w absorbed during the irradiation by the ultrashort light pulse that reads

$$w \geq w_{th} \tag{12.2}$$

where w_{th} amount of energy, that, if deposited instantaneously inside unit volume of a solid, causes structural changes. Quantity w can be calculated as Ohmic losses of the field due to currents (see also Eqs. (8.33) and (10.8))

$$w = \int_{-\infty}^{\infty} \vec{E}(t) \cdot \left(\vec{J}^{(c)}(t) + \vec{J}^{(t)}(t) \right) dt \tag{12.3}$$

For breakdown criterion in the form (12.2) to work, we need to provide value of

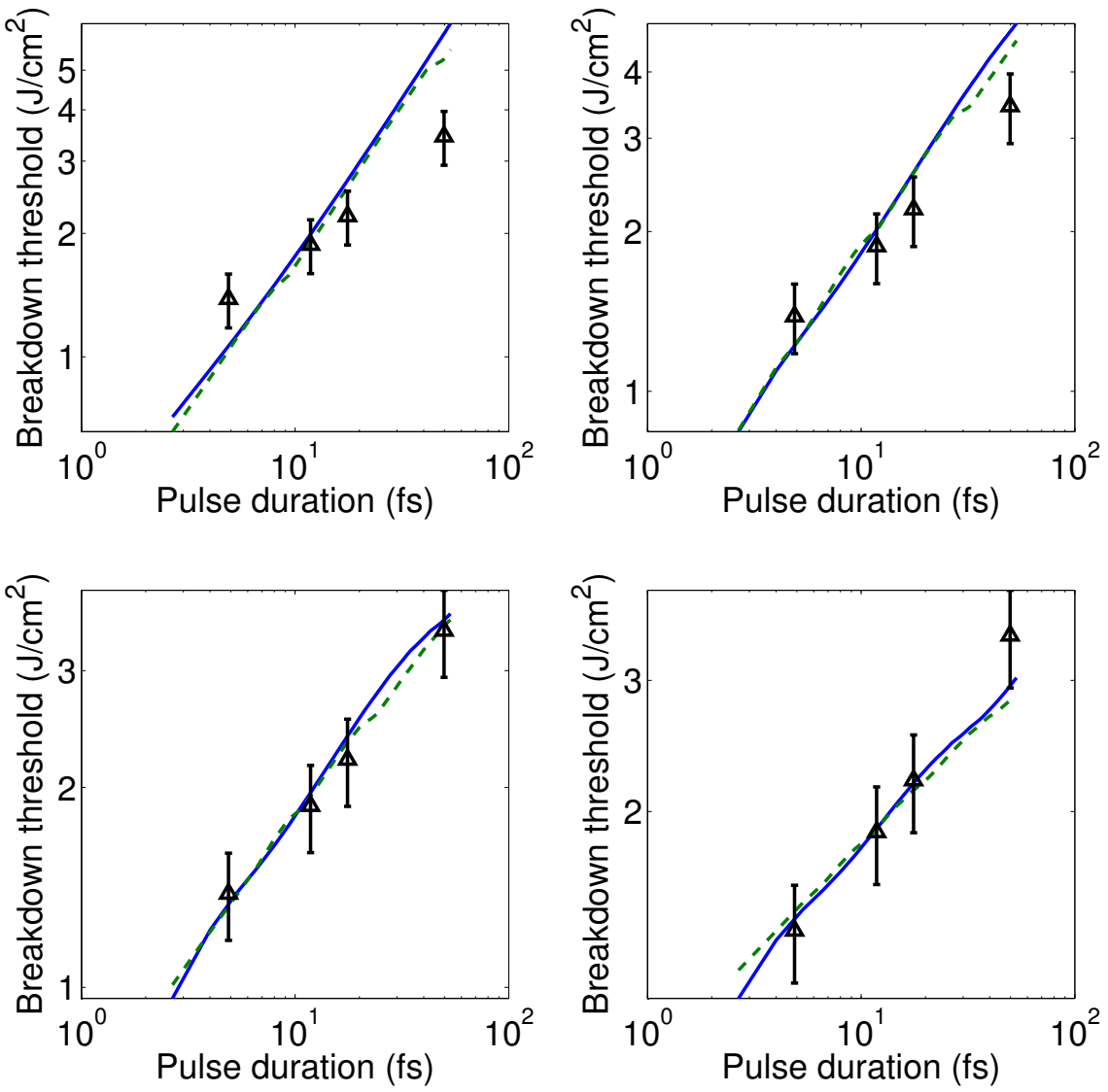

Figure 12.2 Breakdown threshold in fused silica as a function of pulse duration calculated using criterion (12.4) (solid blue line), using Keldysh formula with avalanche ionization (12.2) (dashed green line). Value of avalanche cross-section is (a) 0, (b) 2×10^{-18} cm^{-2}, (c) 5×10^{-18} cm^{-2}, and (b) 10^{-17} cm^{-2}. Best fit value of wth (th) is (a) 3 kJ/cm^3 (10^{21} cm^{-3}), (b) 6.8 kJ/cm^3 (3.4×10^{21} cm^{-3}), (c) 21 kJ/cm3 (1.2×10^{22} cm^{-3}), (d) 0.16 MJ/cm3 (1.5×10^{23} cm^{-3}), Experimental points from Lenzner et al [4] are shown as black triangles.

w_{th}. As an order-of-magnitude estimate of w_{th} we can take the energy required to heat up unit volume of the material up to the melting point and overcome latent fusion heat. For most optical materials such estimate lands in the range 0.1 – 10 kJ/cm^3. However, it is established that femtosecond breakdown itself is a non-thermal process [152, 100, 146], hence, such an estimate can be expected to overshoot actual values of w_{th}. More accurate determination of w_{th} is possible through fitting results of our calculations to the experimental data. To this end, we choose model parameters to mimic fused silica (as we speculated in the previous sections, although fused silica is not a cubic-symmetry crystal, for which our photoionization model is supposed to work best, most of the experimental data on ultrashort pulse optical breakdown is available for fused silica), namely, $\mathcal{E}_g = 9$ eV, $\Delta = 5.5$ eV, $m^* \approx m_e$. Then we calculate absorbed energy as a function of peak intensity (taking into account Fresnel reflection at the air fused silica boundary), pulse duration and avalanche ionization cross-section for Gaussian pulses and fit the results to the experimental data from [4] to obtain w_{th} . To make a fair comparison with existing theory of optical breakdown, we also calculate CB electron density using Keldysh theory augmented with avalanche ionization, namely, through equation (10.1), setting

$$\rho \geq \rho_{th} \tag{12.4}$$

as a breakdown criterion and fitting the results to the experimental points to extract ρ_{th}. Results of both fitting approaches are summarized in Fig. 12.2. With no avalanche ionization (avalanche ionization cross-section $\sigma = 0$) theoretically predicted breakdown threshold grows faster as a function of pulse duration than observed in experiment [12.2(a)]. Conversely, with larger avalanche ionization cross-section breakdown threshold exhibits weaker dependence on pulse duration then experimen-

tally observed [Fig. 12.2(d)]. Both approaches fit well into experimental data down to pulse width of 5 fs, but predict slightly different values of breakdown threshold for single-cycle (2.5 fs) laser pulses.

To summarize, in this section we propose a new ultrashort laser pulse-induced breakdown criterion in dielectrics, based on the amount of field energy absorbed by dielectric in a unit volume. This amount of energy can be calculated using our field-cycle-resolved photoionization theory (FCRPI). The results agree with experimental data from [4] for pulses with duration down to 2 cycles.

13. CONCLUSIONS

Powerful ultrashort laser pulses are transforming modern science and technology in the areas well beyond conventionally optics such as biology, chemistry, medicine, material processing, solid state physics and electronics. Tailoring ultrashort pulses themselves and ultrafast processes using light pulses of arbitrary shape will allow observation and control of processes with unprecedented temporal and spatial resolution, opening up even more applications and perspective-changing methods. In the present Ph. D. research we have investigated analytically and numerically two groups of such methods. One group is related to filamentation of ultrashort laser pulses, where we have found new regimes that form ultrashort and ultraintense wave transients, and discovered general scaling laws of filamentation that will help to translate any filamentation regime in gas to almost arbitrary level of powers.

The second group of methods develops field-cycle-resolved photoionization theory in solids (FCRPI). FCRPI, on one hand, provides photoionization probability and photocurrent density induced by fields of arbitrary shape and duration. On the other hand, FCRPI accurately reproduces results of Schrödinger equation simulations, and recovers results of Keldysh photoionization theory in the appropriate limits of the applicability of the latter. FCRPI can be used directly to analyse high-harmonic generaton or optical breakdown by shaped ultrashort pulses, and it can be incorporated into various propagation codes for accurate analysis of photoionization in the bulk of dielectric media, in photonic crystals and solid-core waveguides. FCRPI provides closed-form analysis of ultrafast charge dynamics in solids that can potentially permit optical-frequency solid state electronics that will process information 6 orders of magnitude faster than current semiconductor chips. Numerical evalua-

tion of integrals in FCRPI can easily be parallelized onto various modern computing architectures.

REFERENCES

[1] P. A. Zhokhov, V. Y. Panchenko, and A. M. Zheltikov, "Filamentation-assisted self-compression of subpetawatt laser pulses to relativistic-intensity subcycle field waveforms," *Phys. Rev. A*, vol. 86, p. 013835, 2012.

[2] P. A. Zhokhov and A. M. Zheltikov, "Attosecond Shock Waves," *Phys. Rev. Lett.*, vol. 110, no. 18, p. 183903, 2013.

[3] P. A. Zhokhov and A. M. Zheltikov, "Scaling laws for laser-induced filamentation," *Phys. Rev. A*, vol. 89, no. 4, p. 043816, 2014.

[4] M. Lenzner, J. Krüger, S. Sartania, Z. Cheng, C. Spielmann, G. Mourou, W. Kautek, and F. Krausz, "Femtosecond Optical Breakdown in Dielectrics," *Phys. Rev. Lett.*, vol. 80, no. 18, p. 4076, 1998.

[5] N. Bloembergen and A. H. Zewail, "Energy redistribution in isolated molecules and the question of mode-selective laser chemistry revisited. New experiments on the dynamics of collisionless energy redistribution in molecules possibilities for laser-selective chemistry with subpicosecond pulses," *J. Phys. Chem.*, vol. 88, no. 23, p. 5459, 1984.

[6] A. Zewail, "Femtochemistry Atomic-scale dynamics of the chemical bond using ultrafast lasers," in *Nobel Lectures, Chemistry 1996-2000* (I. Grenthe, ed.), p. 274, Singapore: World Scientific Publishing Co., 2003.

[7] A. Baltuska, T. Udem, M. Uiberacker, M. Hentschel, E. Goulielmakis, C. Gohle, R. Holzwarth, V. S. Yakovlev, A. Scrinzi, T. W. Hänsch, and F. Krausz, "Attosecond control of electronic processes by intense light fields," *Nature*, vol. 421, no. 6923, p. 611, 2003.

[8] E. Goulielmakis, V. S. Yakovlev, A. L. Cavalieri, M. Uiberacker, V. Pervak, A. Apolonski, R. Kienberger, U. Kleineberg, and F. Krausz, "Attosecond Control and Measurement: Lightwave Electronics," *Science*, vol. 317, no. 5839, p. 769, 2007.

[9] H. Akagi, T. Otobe, A. Staudte, A. Shiner, F. Turner, R. Dorner, D. M. Villeneuve, and P. B. Corkum, "Laser Tunnel Ionization from Multiple Orbitals in HCl," *Science*, vol. 325, no. 5946, p. 1364, 2009.

[10] P. B. Corkum and F. Krausz, "Attosecond science," *Nat. Phys.*, vol. 3, p. 381, 2007.

[11] J. Schwinger, "On gauge invariance and vacuum polarization," *Phys. Rev.*, vol. 82, no. 5, p. 664, 1951.

[12] S. S. Bulanov, T. Z. Esirkepov, A. G. R. Thomas, J. K. Koga, and S. V. Bulanov, "Schwinger Limit Attainability with Extreme Power Lasers," *Rev. Mod. Phys.*, vol. 105, no. 22, 2010.

[13] L. V. Keldysh, "Ionization in the field of strong electromagnetic wave," *Sov. Phys. JETP*, vol. 20, p. 1307, 1965.

[14] E. O. Kane, "Zener tunneling in semiconductors," *J. Phys. Chem. Solids*, vol. 12, p. 181, 1959.

[15] D. Strickland and G. Mourou, "Compression of amplified chirped optical pulses," *Opt. Commun.*, vol. 56, no. 3, p. 219, 1985.

[16] A. Braun, G. Korn, X. Liu, D. Du, J. Squier, and G. Mourou, "Self-channeling of high-peak-power femtosecond laser pulses in air.," *Opt. Lett.*, vol. 20, no. 1, p. 73, 1995.

[17] J. H. Marburger, "Self-focusing: Theory," *Prog. Quant. Electron.*, vol. 4, p. 35, 1975.

[18] L. Bergé, S. Skupin, R. Nuter, J. Kasparian, and J.-P. Wolf, "Ultrashort filaments of light in weakly ionized, optically transparent media," *Rep. Prog. Phys.*, vol. 70, no. 10, p. 1633, 2007.

[19] A. Couairon and A. Mysyrowicz, "Femtosecond filamentation in transparent media," *Phys. Rep.*, vol. 441, no. 2–4, p. 47, 2007.

[20] P. Rairoux, H. Schillinger, S. Niedermeier, M. Rodriguez, F. Ronneberger, R. Sauerbrey, B. Stein, D. Waite, C. Wedekind, H. Wille, L. Wöste, and C. Ziener, "Remote sensing of the atmosphere using ultrashort laser pulses," *Appl. Phys. B*, vol. 71, no. 4, p. 573, 2000.

[21] J. Kasparian, M. Rodriguez, G. Méjean, J. Yu, E. Salmon, H. Wille, R. Bourayou, S. Frey, Y.-B. André, A. Mysyrowicz, R. Sauerbrey, J.-P. Wolf, and L. Wöste, "White-Light Filaments for Atmospheric Analysis," *Science*, vol. 301, no. 5629, p. 61, 2003.

[22] Q. Luo, H. L. Xu, S. A. Hosseini, J.-F. Daigle, F. Théberge, M. Sharifi, and S. L. Chin, "Remote sensing of pollutants using femtosecond laser pulse fluorescence spectroscopy," *Appl. Phys. B*, vol. 82, no. 1, p. 105, 2005.

[23] K. Wang, B. D. Strycker, D. V. Voronine, P. K. Jha, M. O. Scully, R. E. Meyers, P. Hemmer, and A. V. Sokolov, "Remote sub-diffraction imaging with femtosecond laser filaments," *Opt. Lett.*, vol. 37, no. 8, p. 1343, 2012.

[24] G. Stibenz, N. Zhavoronkov, and G. Steinmeyer, "Self-compression of millijoule pulses to 7.8 fs duration in a white-light filament.," *Opt. Lett.*, vol. 31, no. 2, p. 274, 2006.

[25] J. Bethge, C. Brée, H. Redlin, G. Stibenz, P. Staudt, G. Steinmeyer, A. Demircan, and S. Düsterer, "Self-compression of 120 fs pulses in a white-light filament," *J. Opt.*, vol. 13, no. 5, p. 055203, 2011.

[26] S. Skupin, G. Stibenz, L. Bergé, F. Lederer, T. Sokollik, M. Schnürer, N. Zhavoronkov, and G. Steinmeyer, "Self-compression by femtosecond pulse filamentation: Experiments versus numerical simulations," *Phys. Rev. E*, vol. 74, no. 5, 2006.

[27] L. Bergé, "Self-compression of 2 μm laser filaments," *Opt. Express*, vol. 16, no. 26, p. 21529, 2008.

[28] V. I. Bespalov and V. I. Talanov, "Filamentary structure of light beams in nonlinear liquids," *JETP Lett.*, vol. 3, no. 12, p. 307, 1966.

[29] G. Méchain, A. Couairon, M. Franco, B. Prade, and A. Mysyrowicz, "Organizing Multiple Femtosecond Filaments in Air," *Phys. Rev. Lett.*, vol. 93, no. 3, p. 1, 2004.

[30] D. Faccio, A. Dubietis, G. Tamosauskas, P. Polesana, G. Valiulis, A. Piskarskas, A. Lotti, A. Couairon, and P. Di Trapani, "Phase- and group-matched nonlinear interactions mediated by multiple filamentation in Kerr media," *Phys. Rev. A*, vol. 76, no. 5, p. 3, 2007.

[31] G. Point, Y. Brelet, A. Houard, V. Jukna, C. Milián, J. Carbonnel, Y. Liu, A. Couairon, and A. Mysyrowicz, "Superfilamentation in Air," *Phys. Rev. Lett.*, vol. 112, no. 22, 2014.

[32] G. Méchain, G. Méjean, R. Ackermann, P. Rohwetter, Y.-B. André, J. Kasparian, B. Prade, K. Stelmaszczyk, J. Yu, E. Salmon, W. Winn, L. A. V. Schlie, A. Mysyrowicz, R. Sauerbrey, L. Wöste, and J.-P. Wolf, "Propagation of fs

TW laser filaments in adverse atmospheric conditions," *Appl. Phys. B*, vol. 80, no. 7, p. 785, 2005.

[33] G. Méchain, C.D'Amico, Y. B. André, S. Tzortzakis, M. Franco, B. Prade, A. Mysyrowicz, A. Couairon, E. Salmon, and R. Sauerbrey, "Range of plasma filaments created in air by a multi-terawatt femtosecond laser," *Opt. Commun.*, vol. 247, no. 1–3, p. 171, 2005.

[34] J. Garnier, "Statistical analysis of noise-induced multiple filamentation," *Phys. Rev. E*, vol. 73, no. 4, p. 046611, 2006.

[35] A. M. Perelomov, V. S. Popov, and M. V. Terent'ev, "Ionization of atoms in an alternating electric field," *Sov. Phys. JETP*, vol. 23, no. 5, p. 924, 1966.

[36] M. V. Ammosov, N. B. Delone, and V. P. Krainov, "Tunnel ionization of complex atoms and of atomic ions in an alternating electromagnetic field," *Sov. Phys. JETP*, vol. 64, no. December 1986, p. 4, 1986.

[37] V. S. Popov, "Tunnel and multiphoton ionization of atoms and ions in a strong laser field (Keldysh theory)," *Physics-Uspekhi*, vol. 47, no. 9, p. 855, 2004.

[38] G. L. Yudin and M. Y. Ivanov, "Nonadiabatic tunnel ionization: Looking inside a laser cycle," *Phys. Rev. A*, vol. 64, no. 1, 2001.

[39] P. G. Hawkins and M. Y. Ivanov, "Role of subcycle transition dynamics in high-order-harmonic generation in periodic structures," *Phys. Rev. A*, vol. 87, no. 6, 2013.

[40] P. A. Zhokhov and A. M. Zheltikov, "Field-Cycle-Resolved Photoionization in Solids," *Phys. Rev. Lett.*, vol. 113, no. 13, p. 133903, 2014.

[41] P. Zhokhov and A. Zheltikov, "Nonlinear-optical coherent combining of supercontinua from multiple filaments," *Phys. Rev. A*, vol. 86, no. 1, p. 013816, 2012.

[42] T. Brabec and F. Krausz, "Nonlinear Optical Pulse Propagation in the Single-Cycle Regime," *Phys. Rev. Lett.*, vol. 78, no. 17, p. 3282, 1997.

[43] M. Kolesik, J. V. Moloney, and M. Mlejnek, "Unidirectional Optical Pulse Propagation Equation," *Phys. Rev. Lett.*, vol. 89, no. 28, p. 283902, 2002.

[44] M. Kolesik and J. Moloney, "Nonlinear optical pulse propagation simulation: From Maxwell's to unidirectional equations," *Phys. Rev. E*, vol. 70, no. 3, p. 1, 2004.

[45] Y. R. Shen, *The Principles of Nonilinear Optics*. Hoboken: Wiley-Interscience, 2003.

[46] R. W. Boyd, *Nonlinear Optics*. San Diego: Academic Press, 3rd ed., 2008.

[47] N. Bloembergen, *Nonlinear Optics*. Singapore: World Scientific Publishing Co., 4th ed., 1996.

[48] G. P. Agrawal, *Nonlinear Fiber Optics*. San Diego: Academic Press, 2001.

[49] M. T. Hassan, T. T. Luu, A. Moulet, O. Raskazovskaya, P. A. Zhokhov, M. Garg, K. N, A. Zheltikov, V. Pervak, F. Krausz, and E. Goulielmakis, "Attosecond optical control of bound electrons," *submitted*.

[50] V. P. Kandidov, O. G. Kosareva, and S. A. Shlenov, "Spatiotemporal instability of an intense subpicosecond laser pulse in gases," *Quantum Electron.*, vol. 27, no. 5, p. 441, 1997.

[51] R. A. Fisher and W. Bischel, "The role of linear dispersion in plane-wave self-phase modulation," *Appl. Phys. Lett.*, vol. 23, no. 12, p. 661, 1973.

[52] R. A. Fisher and W. K. Bischel, "Numerical studies of the interplay between self-phase modulation and dispersion for intense plane-wave laser pulses," *J. Appl. Phys.*, vol. 46, no. 11, p. 4921, 1975.

[53] M. J. Weber, *Handbook of optical materials*. 2003.

[54] C. Brée, J. Bethge, S. Skupin, L. Bergé, A. Demircan, and G. Steinmeyer, "Cascaded self-compression of femtosecond pulses in filaments," *New J. Phys.*, vol. 12, no. 9, p. 093046, 2010.

[55] J. E. Rice, "Frequency-dependent hyperpolarizabilities for argon, krypton, and neon: Comparison with experiment," *J. Chem. Phys.*, vol. 96, no. 10, p. 7580, 1992.

[56] H. J. Lehmeier, W. Leupacher, and A. Penzkofer, "Nonresonant third-order hyperpolarizability of rare gases and N2 determined by third harmonic generation," *Opt. Commun.*, vol. 56, no. 1, p. 67, 1985.

[57] D. P. Shelton, "Nonlinear-optical susceptibilities of gases measured at 1064 and 1319 nm," *Phys. Rev. A*, vol. 42, no. 5, p. 2578, 1990.

[58] K. Zeil, S. D. Kraft, S. Bock, M. Bussmann, T. E. Cowan, T. Kluge, J. Metzkes, T. Richter, R. Sauerbrey, and U. Schramm, "The scaling of proton energies in ultrashort pulse laser plasma acceleration," *New J. Phys.*, vol. 12, no. 4, p. 045015, 2010.

[59] I. Ahmad, S. A. Trushin, Z. Major, C. Wandt, S. Klingebiel, T.-J. Wang, V. Pervak, A. Popp, M. Siebold, F. Krausz, and S. Karsch, "Frontend light source for short-pulse pumped OPCPA system," *Appl. Phys. B*, vol. 97, no. 3, p. 529, 2009.

[60] A. Toepler, "Ueber die Erzeugung einer eigentuemlichen Art von intensiven elektrischen Stromen vermittelst eines Influenz-Elektrometers," *Ann. Phys.*, vol. 201, p. 469, 1865.

[61] E. Mach and L. Sommer, "Über die Fortpflanzungsgeschwindigkeit von Explosionsschallwellen," *Sitz. Kais. Akad. Wiss. Wien*, vol. 75, p. 101, 1877.

[62] L. D. Landau and E. M. Lifshitz, *Fluid Mechanics*. Oxford: Pergamon Press, 1 ed., 1959.

[63] P. O. K. Krehl, *History of Shock Waves, Explosions and Impact: A Chronological and Biographical Reference*. Berlin: Springer, 2009.

[64] L. A. Ostrovskii, "Propagation of wave packets and space-time self-focusing in a nonlinear medium," *Sov. Phys. JETP*, vol. 24, no. 4, p. 797, 1967.

[65] D. Grischkowsky, E. Courtens, and J. Armstrong, "Observation of Self-Steepening of Optical Pulses with Possible Shock Formation," *Phys. Rev. Lett.*, vol. 31, no. 7, p. 422, 1973.

[66] R. L. Fork, C. V. Shank, C. Hirlimann, R. Yen, and W. J. Tomlinson, "Femtosecond white-light continuum pulses," *Opt. Lett.*, vol. 8, no. 1, p. 1, 1983.

[67] G. Yang and Y. R. Shen, "Spectral broadening of ultrashort pulses in a nonlinear medium," *Opt. Lett.*, vol. 9, no. 11, p. 510, 1984.

[68] J. M. Dudley and S. Coen, "Supercontinuum generation in photonic crystal fiber," *Rev. Mod. Phys.*, vol. 78, no. 4, p. 1135, 2006.

[69] A. M. Zheltikov, "Let there be white light : supercontinuum generation by ultrashort laser pulses," *Physics-Uspekhi*, vol. 49, no. 6, p. 605, 2006.

[70] E. E. Serebryannikov, E. Goulielmakis, and A. M. Zheltikov, "Generation of supercontinuum compressible to single-cycle pulse widths in an ionizing gas," *New J. Phys.*, vol. 10, no. 9, p. 093001, 2008.

[71] E. Goulielmakis, S. Koehler, B. Reiter, M. Schultze, A. J. Verhoef, E. E. Serebryannikov, A. M. Zheltikov, and F. Krausz, "Ultrabroadband, coherent light source based on self-channeling of few-cycle pulses in helium.," *Opt. Lett.*, vol. 33, no. 13, p. 1407, 2008.

[72] G. Ben-Dor, O. Igra, and T. Elperin, *Handbook of shock waves*, vol. 1. San Diego: Academic Press, 2000.

[73] F. DeMartini, C. Townes, T. Gustafson, and P. Kelley, "Self-Steepening of Light Pulses," *Phys. Rev.*, vol. 164, no. 2, p. 312, 1967.

[74] D. Anderson and M. Lisak, "Nonlinear asymmetric self-phase modulation and self-steepening of pulses in long optical waveguides," *Phys. Rev. A*, vol. 27, no. 3, p. 1393, 1983.

[75] K. J. Blow and D. Wood, "Theoretical Description of Transient Stimulated Raman Scattering in Optical Fibers," *IEEE J. Quant. Electron.*, vol. 25, no. 12, p. 2665, 1989.

[76] L. L. Boyle, "Higher Polarizability of the Helium Atom," *J. Chem. Phys.*, vol. 45, no. 4, p. 1318, 1966.

[77] D. M. Bishop and B. Lam, "Ab initio study of third-order nonlinear optical properties of helium," *Phys. Rev. A*, vol. 37, no. 2, p. 464, 1988.

[78] W.-C. Liu, "High-order nonlinear susceptibilities of helium," *Phys. Rev. A*, vol. 56, no. 6, p. 4938, 1997.

[79] M. Masili and A. Starace, "Static and dynamic dipole polarizability of the helium atom using wave functions involving logarithmic terms," *Phys. Rev. A*, vol. 68, p. 012508, 2003.

[80] L. Brillouin, *Wave propagation and group veloctiy*. New York: Academic Press, 1960.

[81] G. Gallilei, *Discorsi e Dimostrazioni Matematiche intorno à due nuoue scienze Attenenti alla Mecanica & i Movimenti Locali (Discourses and Mathematical Demonstrations Relating to Two New Sciences)*. 1638.

[82] M. Rodriguez, R. Bourayou, G. Méjean, J. Kasparian, J. Yu, E. Salmon, A. Scholz, B. Stecklum, J. Eislöffel, U. Laux, A. Hatzes, R. Sauerbrey, L. Wöste, and J.-P. Wolf, "Kilometer-range nonlinear propagation of femtosecond laser pulses," *Phys. Rev. E*, vol. 69, no. 3, p. 036607, 2004.

[83] C. Hauri, W. Kornelis, F. Helbing, A. Heinrich, A. Couairon, A. Mysyrowicz, J. Biegert, and U. Keller, "Generation of intense, carrier-envelope phase-locked few-cycle laser pulses through filamentation," *Appl. Phys. B*, vol. 79, no. 6, p. 673, 2004.

[84] A. Couairon, J. Biegert, C. P. Hauri, W. Kornelis, F. W. Helbing, U. Keller, and A. Mysyrowicz, "Self-compression of ultra-short laser pulses down to one optical cycle by filamentation," *J. Mod. Opt.*, vol. 53, no. 1-2, p. 75, 2006.

[85] D. Kartashov, S. Ališauskas, G. Andriukaitis, A. Pugzlys, M. Shneider, A. Zheltikov, S. L. Chin, and A. Baltuška, "Free-space nitrogen gas laser driven by a femtosecond filament," *Phys. Rev. A*, vol. 86, no. 3, p. 033831, 2012.

[86] N. Bloembergen, "Laser-induced electric breakdown in solids," *IEEE J. Quant. Electron.*, vol. 10, no. 3, p. 375, 1974.

[87] T. Brabec and F. Krausz, "Intense few-cycle laser fields: Frontiers of nonlinear optics," *Rev. Mod. Phys.*, vol. 72, no. 2, p. 545, 2000.

[88] M. Tonouchi, "Cutting-edge terahertz technology," *Nat. Photon.*, vol. 1, p. 97, 2002.

[89] M. Uiberacker, T. Uphues, M. Schultze, A. J. Verhoef, V. Yakovlev, M. F. Kling, J. Rauschenberger, N. M. Kabachnik, H. Schröder, M. Lezius, K. L. Kompa, H.-G. Muller, M. J. J. Vrakking, S. Hendel, U. Kleineberg, U. Heinzmann, M. Drescher, and F. Krausz, "Attosecond real-time observation of electron tunnelling in atoms.," *Nature*, vol. 446, no. 7136, p. 627, 2007.

[90] T. Balciunas, A. J. Verhoef, A. V. Mitrofanov, G. Fan, E. E. Serebryannikov, M. Y. Ivanov, A. M. Zheltikov, and A. Baltuska, "Optical and THz signatures of sub-cycle tunneling dynamics," *Chem. Phys.*, vol. 414, p. 92, 2013.

[91] A. J. Verhoef, A. V. Mitrofanov, E. E. Serebryannikov, D. V. Kartashov, A. M. Zheltikov, and A. Baltuška, "Optical Detection of Tunneling Ionization," *Phys. Rev. Lett.*, vol. 104, no. 16, p. 163904, 2010.

[92] A. V. Mitrofanov, A. J. Verhoef, E. E. Serebryannikov, J. Lumeau, L. Glebov, A. M. Zheltikov, and A. Baltuška, "Optical Detection of Attosecond Ionization Induced by a Few-Cycle Laser Field in a Transparent Dielectric Material," *Phys. Rev. Lett.*, vol. 106, no. 14, p. 147401, 2011.

[93] E. O. Kane, "Theory of Tunneling," *J. Appl. Phys.*, vol. 32, no. 1, p. 83, 1961.

[94] V. Gruzdev, "Photoionization rate in wide band-gap crystals," *Phys. Rev. B*, vol. 75, no. 20, p. 205106, 2007.

[95] V. L. Bonch-Bruevich and S. G. Kalaschnikov, *Halbleiterphysik*. Berlin: VEB, 1982.

[96] A. Schiffrin, T. Paasch-Colberg, N. Karpowicz, V. Apalkov, D. Gerster, S. Mühlbrandt, M. Korbman, J. Reichert, M. Schultze, S. Holzner, J. V. Barth, R. Kienberger, R. Ernstorfer, V. S. Yakovlev, M. I. Stockman, and F. Krausz, "Optical-field-induced current in dielectrics," *Nature*, vol. 493, p. 70, 2013.

[97] E. E. Serebryannikov, A. J. Verhoef, A. Mitrofanov, A. Baltuška, and A. M. Zheltikov, "Signatures of attosecond electron tunneling dynamics in the evolution of intense few-cycle light pulses," *Phys. Rev. A*, vol. 80, no. 5, 2009.

[98] E. E. Serebryannikov and A. M. Zheltikov, "Quantum and Semiclassical Physics behind Ultrafast Optical Nonlinearity in the Midinfrared: The Role of Ionization Dynamics within the Field Half Cycle," *Phys. Rev. Lett.*, vol. 113, no. 4, 2014.

[99] M. V. Fischetti, D. J. DiMaria, S. D. Brorson, T. N. Theis, and J. R. Kirtley, "Theory of high-field electron transport in silicon dioxide," *Phys. Rev. B*, vol. 31, p. 8124, 1985.

[100] B. C. Stuart, M. D. Feit, A. M. Rubenchik, B. W. Shore, and M. D. Perry, "Laser-induced damage in dielectrics with nanosecond to subpicosecond pulses," *Phys. Rev. Lett.*, vol. 74, no. 12, p. 2248, 1995.

[101] A.-C. Tien, S. Backus, H. Kapteyn, M. Murnane, and G. Mourou, "Short-pulse laser damage in transparent materials as a function of pulse duration," *Phys. Rev. Lett.*, vol. 82, no. 19, p. 3883, 1999.

[102] A. Couairon, L. Sudrie, M. Franco, B. Prade, and A. Mysyrowicz, "Filamentation and damage in fused silica induced by tightly focused femtosecond laser pulses," *Phys. Rev. B*, vol. 71, no. 12, p. 125435, 2005.

[103] V. Temnov, K. Sokolowski-Tinten, P. Zhou, A. El-Khamhawy, and D. von der Linde, "Multiphoton Ionization in Dielectrics: Comparison of Circular and Linear Polarization," *Phys. Rev. Lett.*, vol. 97, no. 23, p. 1, 2006.

[104] W. Franz, "Einfluß eines elektrischen Feldes auf eine optische Absorptionskante," *Z. Natur.*, vol. 13a, p. 484, 1958.

[105] L. V. Keldysh, "Behaviour of Non-Metallic Crystals in Strong Electric Fields," *Sov. Phys. JETP*, vol. 7, p. 763, 1958.

[106] S. Ghimire, A. D. DiChiara, E. Sistrunk, P. Agostini, L. F. DiMauro, and D. A. Reis, "Observation of high-order harmonic generation in a bulk crystal," *Nat. Phys.*, vol. 7, no. 2, p. 138, 2011.

[107] F. Wooten, *Optical properties of solids*. New York, NY: Academic press, 1972.

[108] A. Elci, M. O. Scully, A. L. Smirl, and J. C. Matter, "Ultrafast transient response of solid-state plasmas. I. Germanium, theory, and experiment," *Phys. Rev. B*, vol. 16, no. 1, p. 191, 1977.

[109] E. M. Lifshitz and L. P. Pitaevskii, *Physical Kinetics: Volume 10*. Butterworth-Heinemann, 1 edition ed., 1981.

[110] W. L. Kruer, *The physics of laser plasma interactions*. Frontiers in physics: v. 73, Redwood City, Calif. : Addison-Wesley, [1988], 1988.

[111] H. C. Kapteyn, M. M. Murnane, A. Szoke, and R. W. Falcone, "Prepulse energy suppression for high-energy ultrashort pulses using self-induced plasma shuttering.," *Opt. Lett.*, vol. 16, no. 7, p. 490, 1991.

[112] R. Huber, F. Tauser, A. Brodschelm, M. Bichler, G. Abstreiter, and A. Leitenstorfer, "How many-particle interactions develop after ultrafast excitation of an electron-hole plasma," *Astron. Astrophys.*, vol. 414, p. 286, 2001.

[113] M. Schultze, E. M. Bothschafter, A. Sommer, S. Holzner, W. Schweinberger, M. Fiess, M. Hofstetter, R. Kienberger, V. Apalkov, V. S. Yakovlev, M. I. Stockman, and F. Krausz, "Controlling dielectrics with the electric field of light," *Nature*, vol. 493, p. 75, 2012.

[114] M. Schultze, K. Ramasesha, C. D. Pemmaraju, S. A. Sato, D. Whitmore, A. Gandman, J. S. Prell, L. J. Borja, D. Prendergast, K. Yabana, and others, "Attosecond band-gap dynamics in silicon," *Science*, vol. 346, no. 6215, p. 1348, 2014.

[115] H. Kuzmany, *Solid-state spectrocopy*. Berlin: Springer, 2009.

[116] M. S. Dresselhaus, "Solid state physics Part II: Optical properties of solids," lecture Notes, MIT, 2001.

[117] K. El Sayed, S. Schuster, H. Haug, F. Herzel, and K. Henneberger, "Sub-picosecond plasmon response: buildup of screening," *Phys. Rev. B*, vol. 49, no. 11, p. 7337, 1994.

[118] J. Szczytko, L. Kappei, J. Berney, F. Morier-Genoud, M. T. Portella-Oberli, and B. Deveaud, "Determination of the Exciton Formation in Quantum Wells from Time-Resolved Interband Luminescence," *Phys. Rev. Lett.*, vol. 93, no. 13, p. 137401, 2004.

[119] R. R. Gattass and E. Mazur, "Femtosecond laser micromachining in transparent materials," *Nat. Photon.*, vol. 2, no. 4, p. 219, 2008.

[120] U. K. Tirlapur and K. Koenig, "Targeted transfection by femtosecond laser.," *Nature*, vol. 418, no. 6895, p. 290, 2002.

[121] A. Vogel, J. Noack, G. Hüttman, and G. Paltauf, "Mechanisms of femtosecond laser nanosurgery of cells and tissues," *Appl. Phys. B*, vol. 81, no. 8, p. 1015,

2005.

[122] S. S. Jha, "Theory of optical harmonic generation at a metal surface," *Phys. Rev.*, vol. 140, no. 6A, p. A2020, 1965.

[123] D. Von der Linde and K. Rzazewski, "High-order optical harmonic generation from solid surfaces," *Appl. Phys. B*, vol. 63, no. 5, p. 499, 1996.

[124] F. Brunel, "Harmonic generation due to plasma effects in a gas undergoing multiphoton ionization in the high-intensity limit," *J. Opt. Soc. Am. B*, vol. 7, no. 4, p. 521, 1990.

[125] F. Silva, D. Austin, A. Thai, M. Baudisch, M. Hemmer, D. Faccio, A. Couairon, and J. Biegert, "Multi-octave supercontinuum generation from mid-infrared filamentation in a bulk crystal," *Nat. Comm.*, vol. 3, p. 807, 2012.

[126] K. S. Yee, "Numerical solution of initial boundary value problems involving Maxwell's equations in isotropic media," *IEEE Trans. Antennas Propag*, vol. 14, no. 3, p. 302, 1966.

[127] D. Sullivan, *Electromagnetic simulation using the FDTD method*. Hoboken, NJ, USA: Wiley, 2 ed., 2013.

[128] J. M. Bourgeois and G. S. Smith, "A fully three-dimensional simulation of a ground-penetrating radar: FDTD theory compared with experiment," *IEEE Trans. Geosci. Remote Sens.*, vol. 34, no. 1, p. 36, 1996.

[129] L. Gürel and U. Oğuz, "Three-dimensional FDTD modeling of a ground-penetrating radar," *IEEE Trans. Geosci. Remote Sens.*, vol. 38, no. 4, p. 1513, 2000.

[130] S. Hu, H. Chen, C. Law, Z. Shen, L. Zhu, W. Zhang, and W. Dou, "Backscattering Cross Section of Ultrawideband Antennas," *IEEE Antenn. Wireless Propag. Lett.*, vol. 6, no. 11, p. 70, 2007.

[131] C. Lee, J. Thillaigovindan, C.-C. Chen, X. T. Chen, Y.-T. Chao, S. Tao, W. Xiang, A. Yu, H. Feng, and G. Q. Lo, "Si nanophotonics based cantilever sensor," *Appl. Phys. Lett.*, vol. 93, no. 11, p. 113113, 2008.

[132] G. W. Burr and A. Farjadpour, "Balancing accuracy against computation time: 3d FDTD for nanophotonics device optimization," in *Proc. SPIE*, vol. 5733, p. 336, 2005.

[133] M. L. Brongersma and P. G. Kik, eds., *Surface plasmon nanophotonics*. No. 131 in Springer series in optical sciences, Dordrecht: Springer, 2007.

[134] Q. Wang and S.-T. Ho, "Ultracompact TM-Pass Silicon Nanophotonic Waveguide Polarizer and Design," *IEEE Photon. J.*, vol. 2, no. 1, p. 49, 2010.

[135] E. Ozbay, "Plasmonics: merging photonics and electronics at nanoscale dimensions," *Science*, vol. 311, no. 5758, p. 189, 2006.

[136] A. Dhawan, S. J. Norton, M. D. Gerhold, and T. Vo-Dinh, "Comparison of FDTD numerical computations and analytical multipole expansion method for plasmonics-active nanosphere dimers," *Opt. Express*, vol. 17, no. 12, p. 9688, 2009.

[137] J. Shibayama, A. Nomura, R. Ando, J. Yamauchi, and H. Nakano, "A Frequency-Dependent LOD-FDTD Method and Its Application to the Analyses of Plasmonic Waveguide Devices," *IEEE J. Quant. Electron.*, vol. 46, no. 1, p. 40, 2010.

[138] K. H. Lee, I. Ahmed, R. S. M. Goh, E. H. Khoo, E. P. Li, and T. G. G. Hung, "Implementation of the FDTD method based on Lorentz-Drude dispersive model on GPU for plasmonics applications," *Prog. Electromagn. Res.*, vol. 116, p. 441, 2011.

[139] A. S. Nagra and R. York, "FDTD analysis of wave propagation in nonlinear absorbing and gain media," *IEEE Trans. Antennas Propag*, vol. 46, no. 3, p. 334, 1998.

[140] A. F. Oskooi, D. Roundy, M. Ibanescu, P. Bermel, J. Joannopoulos, and S. G. Johnson, "Meep: A flexible free-software package for electromagnetic simulations by the FDTD method," *Comp. Phys. Comm.*, vol. 181, no. 3, p. 687, 2010.

[141] S. A. Akhmanov and S. Y. Nikitin, *Physical optics*. Oxford: Clarendon Press, 1997.

[142] E. Yablonovitch and N. Bloembergen, "Avalanche ionization and the limiting diameter of filaments induced by light pulses in transparent media," *Phys. Rev. Lett.*, vol. 29, no. 14, p. 907, 1972.

[143] V. N. Lugovoi and A. M. Prokhorov, "Theory of the propagation of high-power laser radiation in a nonlinear medium," *Sov. Phys. Usp.*, vol. 16, no. 5, p. 658, 1974.

[144] A. A. Manenkov and A. M. Prokhorov, "Laser-induced damage in solids," *Sov. Phys. Usp.*, vol. 29, no. 1, p. 104, 1986.

[145] P. K. Kennedy, "A first-order model for computation of laser-induced breakdown thresholds in ocular and aqueous media. I. Theory," *IEEE J. Quant. Electron.*, vol. 31, no. 12, p. 2241, 1995.

[146] B. C. Stuart, M. D. Feit, S. Herman, A. M. Rubenchik, B. W. Shore, and M. D. Perry, "Optical ablation by high-power short-pulse lasers," *J. Opt. Soc. Am. B*, vol. 13, no. 2, p. 459, 1996.

[147] L. Sudrie, A. Couairon, M. Franco, B. Lamouroux, B. Prade, S. Tzortzakis, and A. Mysyrowicz, "Femtosecond Laser-Induced Damage and Filamentary Propagation in Fused Silica," *Phys. Rev. Lett.*, vol. 89, no. 18, p. 186601, 2002.

[148] M. Durand, A. Jarnac, A. Houard, Y. Liu, S. Grabielle, N. Forget, A. Durécu, A. Couairon, and A. Mysyrowicz, "Self-Guided Propagation of Ultrashort Laser Pulses in the Anomalous Dispersion Region of Transparent Solids: A New Regime of Filamentation," *Phys. Rev. Lett.*, vol. 110, no. 11, 2013.

[149] A. A. Lanin, A. A. Voronin, E. A. Stepanov, A. B. Fedotov, and A. M. Zheltikov, "Frequency-tunable sub-two-cycle 60-MW-peak-power free-space waveforms in the mid-infrared," *Opt. Lett.*, vol. 39, no. 22, p. 6430, 2014.

[150] M. Hemmer, M. Baudisch, A. Thai, A. Couairon, and J. Biegert, "Self-compression to sub-3-cycle duration of mid-infrared optical pulses in dielectrics," *Opt. Express*, vol. 21, no. 23, p. 28095, 2013.

[151] A. Pugzlys, P. Malevich, S. Alisauskas, A. A. Voronin, D. Kartashov, A. Baltuska, A. Zheltikov, and D. Faccio, "Self-compression of Millijoule mid-IR Femtosecond Pulses in Transparent Dielectrics," in *CLEO: 2014*, p. FTh1D.3, Optical Society of America, 2014.

[152] D. Du, X. Liu, G. Korn, J. Squier, and G. Mourou, "Laser-induced breakdown by impact ionization in SiO2 with pulse widths from 7 ns to 150 fs," *Appl. Phys. Lett.*, vol. 64, no. 23, p. 3071, 1994.

[153] N. Shen, D. Datta, C. B. Schaffer, P. LeDuc, D. E. Ingber, and E. Mazur, "Ablation of cytoskeletal filaments and mitochondria in live cells using a femtosecond laser nanoscissor," *Mech. Chem. Biosyst*, vol. 2, no. 1, p. 17, 2005.